

The population of Galactic Centre filaments – III. Candidate radio and stellar sources

F. Yusef-Zadeh¹★, R. G. Arendt²★, M. Wardle³, I. Heywood^{4,5} and W. Cotton⁶

¹Department of Physics and Astronomy, Northwestern University, Evanston, IL 60208, USA

²NASA/GSFC, Code 665, 8800 Greenbelt Road, Greenbelt, MD 20771, UMBC/CRESST 2, USA

³School of Mathematical and Physical Sciences, Research Centre for Astronomy, Astrophysics and Astrophotonics, Macquarie University, Sydney, NSW 2109, Australia

⁴Royal Astronomical Society, Burlington House, Piccadilly, London W1J 0BQ, UK

⁵Department of Physics and Electronics, Rhodes University, PO Box 94, Makhanda, 6140, South Africa

⁶National Radio Astronomy Observatory, Charlottesville, VA 60208, USA

Accepted 2022 August 22. Received 2022 August 22; in original form 2022 June 27

ABSTRACT

Recent MeerKAT radio continuum observations of the Galactic Centre at 20 cm show a large population of non-thermal radio filaments (NRFs) in the inner few hundred pc of the Galaxy. We have selected a sample of 57 radio sources, mainly compact objects, in the MeerKAT mosaic image that appear to be associated with NRFs. The selected sources are about four times the number of radio point sources associated with filaments than would be expected by random chance. Furthermore, an apparent correlation between bright IR stars and NRFs is inferred from their similar latitude distributions, suggesting that they both co-exist within the same region. To examine if compact radio sources are related to compact IR sources, we have used archival 2MASS, and *Spitzer* data to make spectral energy distribution of individual stellar sources coincident or close to radio sources. We provide a catalogue of radio and IR sources for future detailed observations to investigate a potential three-way physical association between NRFs, compact radio and IR stellar sources. This association is suggested by models in which NRFs are cometary tails produced by the interaction of a large-scale nuclear outflow with stellar wind bubbles in the Galactic Centre.

Key words: plasmas – radiation mechanisms: non-thermal – cosmic rays – ISM: magnetic fields.

1 INTRODUCTION

The inner thousand light years of our Galaxy are unusually active compared to the solar neighbourhood. The dormant supermassive black hole, Sgr A*, is surrounded by hot young stars with powerful winds that irradiate the nearby interstellar gas. There is circumstantial evidence of two past explosions within the last few million years. First, vast γ -ray emitting lobes filled with relativistic particles emerge from the Galactic Centre and extend above and below the disc for many thousands of light years (i.e. the Fermi bubble) (Su, Slatyer & Finkbeiner 2010). Secondly, a bipolar MeerKAT radio bubble filled by coronal X-ray emitting hot gas emerges from the inner few hundred light years of the Galaxy. The radio bubble hosts hundreds of mysterious magnetized radio filaments. The filaments occupy a region consistent with the radio bubble, suggesting a causal association between the two (Heywood et al. 2019). Theoretical models explain the *Fermi* and MeerKAT bubbles by invoking a correlated burst of supernovae or an explosion from the black hole as it swallows a cloud (Crocker & Aharonian 2011; Yang, Ruszkowski & Zweibel 2013).

The high cosmic-ray flux in the Galactic Centre suggests a global injection of relativistic particles produced as a result of a relic of a past activity by Sgr A*, due to starburst activity producing

multiple supernova explosions (Heywood et al. 2019). One scenario for the origin of the bipolar radio/X-ray features considers high cosmic-ray pressure driving large-scale winds and expanding the medium away from the Galactic plane. It has become apparent that relativistic particles permeate the central molecular zone (CMZ) at levels a thousand times that in the solar neighborhood (Geballe et al. 1999; Oka et al. 2005, 2019; Indriolo & McCall 2012; Goto et al. 2014; Le Petit et al. 2016). This provides a significant source of pressure when compared to thermal pressure in interstellar space at the Galactic Centre. High cosmic-ray pressure drives winds in the nuclei of galaxies (Everett et al. 2008; Everett, Schiller & Zweibel 2010; Ruszkowski, Yang & Zweibel 2017; Zweibel 2017) and play a role in feedback, limiting star formation and the growth of the central supermassive black holes by transferring their momentum and energy into the surrounding medium. The high-cosmic-ray flux in the Galactic Centre suggests global injection of relativistic particles produced as a result of a relic of a past activity by Sgr A*, due to starburst activity producing multiple supernovae explosions (Heywood et al. 2019). The interaction of a cosmic-ray-driven wind with stellar wind bubbles create cometary tails that could explain the energetic non-thermal radio filaments (NRFs) found throughout the Galactic Centre (Shore & LaRosa 1999; Bicknell & Li 2001; Yusef-Zadeh & Wardle 2019; Yusef-Zadeh et al. 2022a). In this scenario, a compact radio source is expected to be located along or at one end of NRFs where the wind interacts with mass-losing stars.

Another model suggests a time-dependent injecting source, such as a pulsar, crossing spatially intermittent magnetic bundles and

* E-mail: zadeh@northwestern.edu (FY-Z); richard.g.arendt@nasa.gov (RGA)

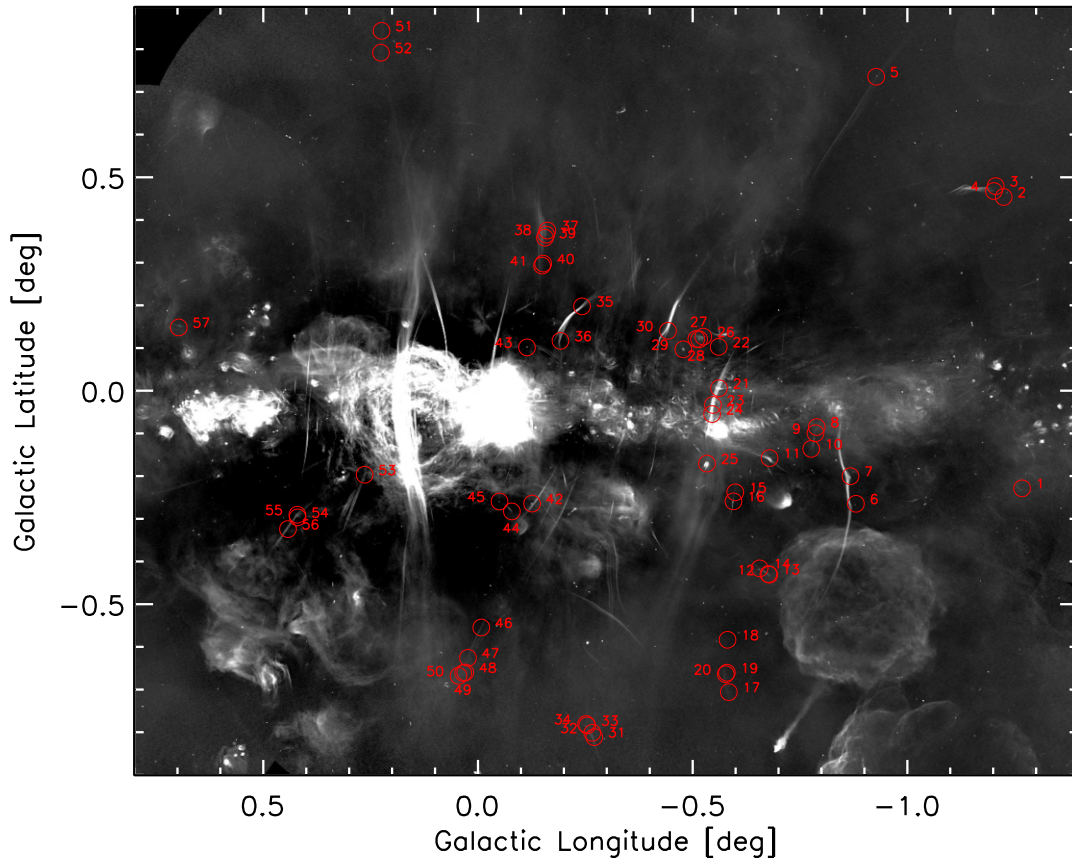


Figure 1. A 1.28-GHz mosaic image of the Galactic Centre region (Heywood et al. 2022). Red circles show the positions of compact radio sources with possible infrared counterparts. A blow-up of these sources is shown in Fig. 3(a)–(eee). There are 57 circles corresponding to the number of sources listed in Table 1.

generates filamentary structure (Thomas, Pfrommer & Enßlin 2020). This model predicts the filaments run perpendicular to the direction of the motion, unlike cometary tail model in which compact sources inject particles in the direction opposite to their motion (Shore & LaRosa 1999; Yusef-Zadeh & Wardle 2019).

Motivated by these scenarios, we provide a list of candidate radio and stellar sources that appear to be associated with NRFs. Candidate radio sources are selected only from 43 groupings of 174 magnetized filaments that run parallel to each other and are separated from each other by mean spacing of 16 arcsec (0.64 pc) (Yusef-Zadeh et al. 2022). We selected the most spectacular groupings of filaments ranging from pairs to dozens in Yusef-Zadeh et al. (2022a). We defined a group of filaments or a grouping having similar orientations, similar curvature or bending, spatially close to each other, and in some cases, converge to a point, shift sideways together, and change direction coherently. These characteristics implied that they are parts of the same system of filaments with a common origin. We avoided groups of filaments close to the Galactic plane because of confusing thermal sources in this region. The groups of filaments we selected are distinct from single filaments along the line of sight at large physical distances from each other but which appear close in projection. The analysis of single filaments, which may comprise multiple filaments in future higher resolution observations, are postponed elsewhere. We present radio and infrared images of each of the 57 candidate sources as well as the spectral energy distributions (SEDs) of their IR counterparts. The purpose of this list is to motivate further high sensitivity, spatial resolution radio and IR observations to examine a three-way spatial correlation and to test the cometary tail model of the origin of the filaments.

2 MEERKAT AND VLA OBSERVATIONS

Details of MeerKAT and the Karl G. Jansky Very Large Array (VLA) observations are found in Heywood et al. (2019), Heywood et al. (2022). Figure 1 shows a mosaic MeerKAT image of the inner few degrees of the Galactic Centre (1 arcmin corresponds to 2.4 pc at the Galactic Centre distance) with an FWHM ~ 4 arcsec resolution. VLA obtained higher resolution images of the region toward two fields centred on Sgr C and Sgr A. Thus, only few sources have been covered with these limited high-resolution measurements. VLA observation was carried out at L band (1–2 GHz) with the array in the most extended A-configuration and centred at Sgr C (J2000 $17^{\text{h}}44^{\text{m}}35^{\text{s}}.0$, $-29^{\circ}29'00''.0$). The initial flagging and reference calibration was performed using the VLA casa pipeline8 and processed with the wsclean multiscale clean algorithm with a resolution of ~ 1 arcsec. Further details on the use of the VLA data can be found in Heywood et al. (2022).

3 RESULTS AND DISCUSSION

3.1 Stellar and NRF distributions

To examine the possible association of NRFs and stellar sources on a much larger scale, Figure 2(left- and right-hand panels) display the histograms of magnetized filaments longer than 66 arcsec and of bright IR stars (Ramirez et al. 2008), as traced in four *Spitzer* bands, as a function of Galactic latitudes. Bright stars are selected mainly to avoid confusion limits and minimize extinction. A length of 66 arcsec is selected because it is a good constraint for the exclusion of thermal

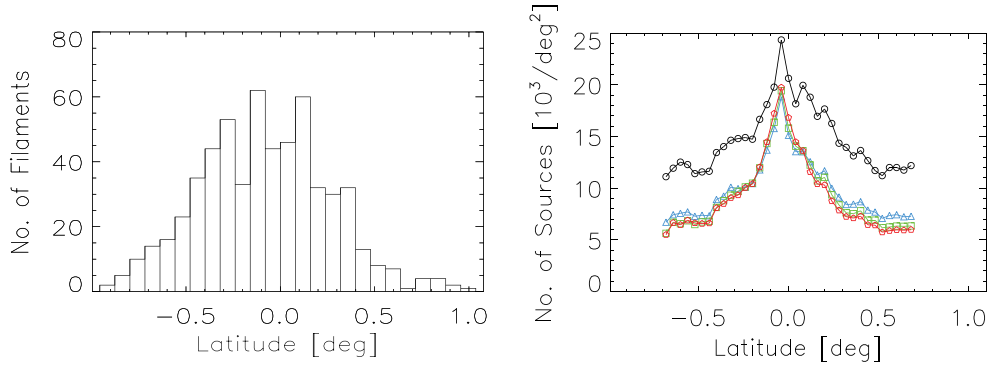


Figure 2. Left-hand panel: A histogram of the number of NRFs is shown as a function of Galactic latitude for filament lengths longer than 66 arcsec and confined to within Galactic latitude $|l| < 0.45^\circ$ (which excludes most of the thermal features), based on MeerKAT data. Right-hand panel: A histogram of the number of bright stars is shown as a function of Galactic latitude using IRAC data in all four bands 3.6, 4.5, 5.8, and 8 μm (black, blue, green, and red). This plot is constructed from data presented in (Ramirez et al. 2008).

filamentary features versus NRFs (Yusef-Zadeh et al. 2022a). The similar scale heights of the filaments and stellar sources indicate their Galactic population is suggestive of a spatial correlation between the two. In addition, both distributions tend to peak at slightly negative latitudes, suggesting that both populations are possibly associated with each other. However, robust statistical tests, e.g. the two-sample KS test, simply confirm that there are real differences between the distributions in Fig. 2(left- and right-hand panels). That’s no surprise given that some fraction of the stars will be ‘local’ while all of the NRFs are at the Galactic Centre. To investigate this weak correlation further, we will next examine the spatial relationship between compact radio and IR stellar sources as well as the SEDs of IR sources closest to the peaks of compact radio sources.

3.2 Compact radio and stellar sources

We have identified a sample of small resolved radio sources and unresolved compact radio sources in the MeerKAT image of the Galactic Centre that appear to coincide with one end of or along NRFs. Examination of modified images in which all radio sources are artificially shifted with respect to the filaments,¹ indicates that only $\sim 1/4$ of the apparent correlations between NRFs and compact sources can be attributed to random coincidence. A single filament with a length of 50 pc and width of 0.1 pc has a volume of $\sim 0.5 \text{ pc}^3$ whereas the large-scale volume of the CMZ is roughly $\sim 10^7 \text{ pc}^3$, giving a small filling factor of $\sim 10^{-3}$ for NRFs. Given the large stellar density of $\sim 10^6$ IR sources in the CMZ (Ramirez et al. 2008), the average number of stellar sources within the volume of a filament is expected to be about one. In addition, there are many striking examples of a single filament splitting into two prongs at a junction where a resolved compact radio source is located, suggestive of a flow of plasma along the filaments (Yusef-Zadeh et al. 2022). So, it is possible that a source, such as a mass-losing star, is responsible for injecting cosmic-ray particles into the filaments or acting as an obstacle redirecting plasma flow (Yusef-Zadeh & Wardle 2019; Yusef-Zadeh et al. 2022a). In this picture, mass-losing stars such as the red giants are impacted by a cosmic-ray-driven wind, creating shocks at the wind–wind interface, and pushing the shocked stellar

wind into the tail, thus providing additional acceleration of cosmic-ray particles (Yusef-Zadeh & Wardle 2019).

Not all filaments show a compact radio and infrared candidate source at their ends, so the cometary model may not be viable to explain their origin. It is possible that this subclass of filaments could be explained by an alternative model in which a compact radio source, like a pulsar crossing the filaments, injects cosmic-ray particles intermittently. In this picture, no IR counterpart is expected. A more detailed study of radio compact sources near this subclass of filaments need to be done in the future to test this model.

To examine whether compact radio sources have stellar counterparts, we have used archival 2MASS and *Spitzer* (IRAC and MIPS) data to examine the SED of individual stellar sources that lie closest to the compact radio sources. We have also checked the Gaia catalogue and found 14 of the GALCEN sources have Gaia counterparts within 2 arcsec, 12 of which are within 1 arcsec. These sources are likely foreground sources. In some cases there may be coincidences of unrelated sources. Table 1 tabulates the source number, the positions of radio and infrared sources in Galactic coordinates (l , b), the Gaia source offset, the separation between the peak radio and infrared sources and the peak intensity of the compact radio sources in Columns 1–6, respectively. The mosaic image was blanked below $10 \mu\text{Jy beam}^{-1}$ (Heywood et al. 2022). The last column shows the associated groups of filaments named in Yusef-Zadeh et al. (2022).

We present the SEDs of the nearest GALCEN catalogue (Ramirez et al. 2008) IR source to each of the radio sources, as listed in Table 1. Figure 3 shows a close up view of all 57 compact sources at radio and IR and 1.25–24 μm (2MASS+IRAC + MIPS) SEDs of stellar sources. In spite of the lack of full wavelength coverage, Figure 3 shows a sample illustrating two different classes of SEDs that may be IR counterparts to compact radio sources. In one class, ‘Red Giant SEDs’, show a distinct dip at 4.5 μm (see Fig. 3j, t, v, oo and ww). The dip is caused by the CO fundamental, which strengthens with decreasing temperature (Engelke, Price & Kraemer 2006). These sources are not detected at 24 μm . Other sources do exhibit 24 μm emission. A subset of these are visibly extended in the images and have very red SEDs (Fig. 3u, y, cc). Thus, these are likely young stellar objects and H II regions. The remainder (Figs 3b, c, bb, and vv) are point-like and typically brighter than those sources with red giant SEDs. These stars may be dusty AGB stars or supergiants (Reiter et al. 2015). It is possible that all red giants have 24 μm emission, but that it is only sufficiently bright to be detected by MIPS in these brighter classes of giants. At

¹ Tests were done by shifting point-source images by ± 64 pixels (69 arcsec) in l and b (four independent tests), and then recounting the number of apparent associations between the shifted sources and the NRFs.

Table 1. The positions of infrared sources closest to compact radio sources, both of which could be associated with groups of NRFs.

Number	Radio selection		Closest IRAC/MIPS counterpart		Gaia source offset (arcsec)	Radio-IR source offset (arcsec)	20-cm peak intensity (mJy beam ⁻¹)	Associated filament (group names)
	<i>l</i> (°)	<i>b</i> (°)	<i>l</i> (°)	<i>b</i> (°)				
1	358.732 69	−0.228 66	358.73234	−0.231 10	–	8.9	0.20	Horseshoe
2	358.775 59	0.453 83	358.77572	0.454 70	0.2	3.2	0.03	Pelican
3	358.794 24	0.479 40	358.79452	0.478 98	0.4	1.8	0.07	''
4	358.798 32	0.467 80	358.79845	0.468 30	0.3	1.9	0.14	''
5	359.072 50	0.735 48	359.07256	0.735 26	–	0.8	3.30	Arrow
6	359.119 72	−0.264 79	359.119 41	−0.265 23	–	1.9	0.57	Snake
7	359.132 42	−0.200 15	359.133 14	−0.200 11	–	2.6	1.10	Snake
8	359.211 00	−0.085 00	359.210 45	−0.085 41	–	2.5	0.73	Candle
9	359.213 88	−0.099 65	359.213 27	−0.099 90	–	2.4	0.35	''
10	359.223 89	−0.136 10	359.224 42	−0.136 03	–	1.9	0.20	''
11	359.320 86	−0.157 80	359.319 64	−0.158 09	–	4.5	1.40	Hummingbird
12	359.321 39	−0.430 90	359.322 11	−0.430 14	–	3.8	0.26	Sausage
13	359.323 53	−0.429 52	359.324 78	−0.430 18	0.9	5.1	0.24	''
14	359.343 95	−0.416 10	359.344 18	−0.416 06	–	0.8	0.60	''
15	359.400 80	−0.237 97	359.400 81	−0.238 23	–	1.0	0.01	''
16	359.404 94	−0.259 14	359.404 20	−0.259 35	0.2	2.8	1.41	''
17	359.415 75	−0.706 05	359.414 95	−0.705 14	–	4.4	0.20	Feather
18	359.418 79	−0.583 40	359.419 81	−0.582 45	–	5.0	0.04	''
19	359.420 24	−0.660 49	359.421 36	−0.661 62	–	5.7	0.07	''
20	359.422 88	−0.664 01	359.423 66	−0.662 69	–	5.5	0.41	''
21	359.438 56	0.005 95	359.438 54	0.005 41	1.1	1.9	6.2	Sgr C
22	359.435 80	0.112 72	359.438 67	0.102 42	–	2.9	0.01	French Knife
23	359.452 86	−0.033 31	359.45338	−0.033 38	–	1.9	7.20	Sgr C
24	359.454 76	−0.054 66	359.454 23	−0.05583	–	4.6	1.01	''
25	359.466 64	−0.170 61	359.467 23	−0.171 26	–	3.2	3.3	''
26	359.475 31	0.126 72	359.475 24	0.125 99	–	2.6	0.20	Bent Harp
27	359.484 96	0.120 52	359.485 14	0.119 40	–	4.1	1.80	''
28	359.491 36	0.121 41	359.490 23	0.120 55	–	5.1	0.01	''
29	359.521 74	0.096 97	359.521 46	0.096 94	–	1.0	0.90	''
30	359.557 50	0.140 30	359.557 49	0.138 49	–	6.5	0.50	Ripple
31	359.729 20	−0.811 39	359.729 07	−0.810 95	–	1.6	0.32	Knot
32	359.733 72	−0.801 22	359.734 48	−0.801 24	–	2.7	0.12	''
33	359.745 74	−0.783 98	359.744 98	−0.784 00	–	2.8	1.00	''
34	359.748 29	−0.780 59	359.747 85	−0.781 35	0.3	3.2	0.54	''
35	359.757 64	0.197 74	359.757 82	0.197 85	0.4	0.8	0.78	Flamingo
36	359.807 90	0.116 85	359.807 73	0.117 74	–	3.3	0.31	''
37	359.838 44	0.375 14	359.839 13	0.374 89	–	2.7	0.18	Harp
38	359.841 21	0.365 71	359.840 95	0.366 49	–	3.0	0.17	''
39	359.844 11	0.358 41	359.843 24	0.359 19	–	4.2	0.23	''
40	359.848 14	0.297 77	359.847 43	0.297 17	–	3.3	0.04	''
41	359.850 73	0.293 09	359.849 70	0.293 74	–	4.4	0.20	''
42	359.873 91	−0.264 30	359.874 04	−0.264 46	–	0.7	1.30	Cleaver Knife
43	359.885 80	0.101 55	359.885 86	0.101 01	–	2.0	5.60	Harp
44	359.921 07	−0.282 71	359.920 23	−0.283 00	–	3.2	0.27	Cleaver Knife
45	359.949 84	−0.259 40	359.950 39	−0.259 39	–	2.0	0.73	''
46	359.992 38	−0.554 65	359.992 60	−0.553 14	0.3	5.5	0.08	Comet
47	0.023 33	−0.625 74	0.023 43	−0.626 68	0.05	3.4	0.07	''
48	0.029 52	−0.659 87	0.029 86	−0.660 06	1.9	1.4	0.29	''
49	0.034 34	−0.661 20	0.034 86	−0.660 23	–	4.0	0.28	''
50	0.045 31	−0.667 85	0.045 83	−0.666 76	–	4.4	0.25	''
51	0.224 57	0.842 97	0.224 19	0.843 30	0.8 (1.3)	1.8	0.04	Space Shuttle
52	0.226 05	0.791 78	0.226 51	0.791 85	–	1.7	0.25	''
53	0.264 08	−0.196 83	0.263 61	−0.197 78	–	3.8	0.64	Porcupine
54	0.420 08	−0.296 63	0.419 70	−0.297 18	–	2.4	0.41	Contrail
55	0.420 75	−0.290 48	0.420 99	−0.289 75	–	2.8	0.39	''
56	0.442 69	−0.324 07	0.442 44	−0.323 76	0.4	1.4	0.17	''
57	0.696 88	0.148 27	0.697 03	0.148 05	0.8	1.0	0.75	Bent Fork

the shorter wavelengths, the IRAC data are confusion limited. So spatial coincidence of IR and radio sources at these wavelengths alone is not a strong indication of the actual association of the sources.

Some images appear to show cometary tails traced by the filaments (see Fig. 3i). An interpretation of the head–tail morphology is that the streaming of cosmic rays from the Galactic plane interacts with 24 μ m sources and create a tail oriented in

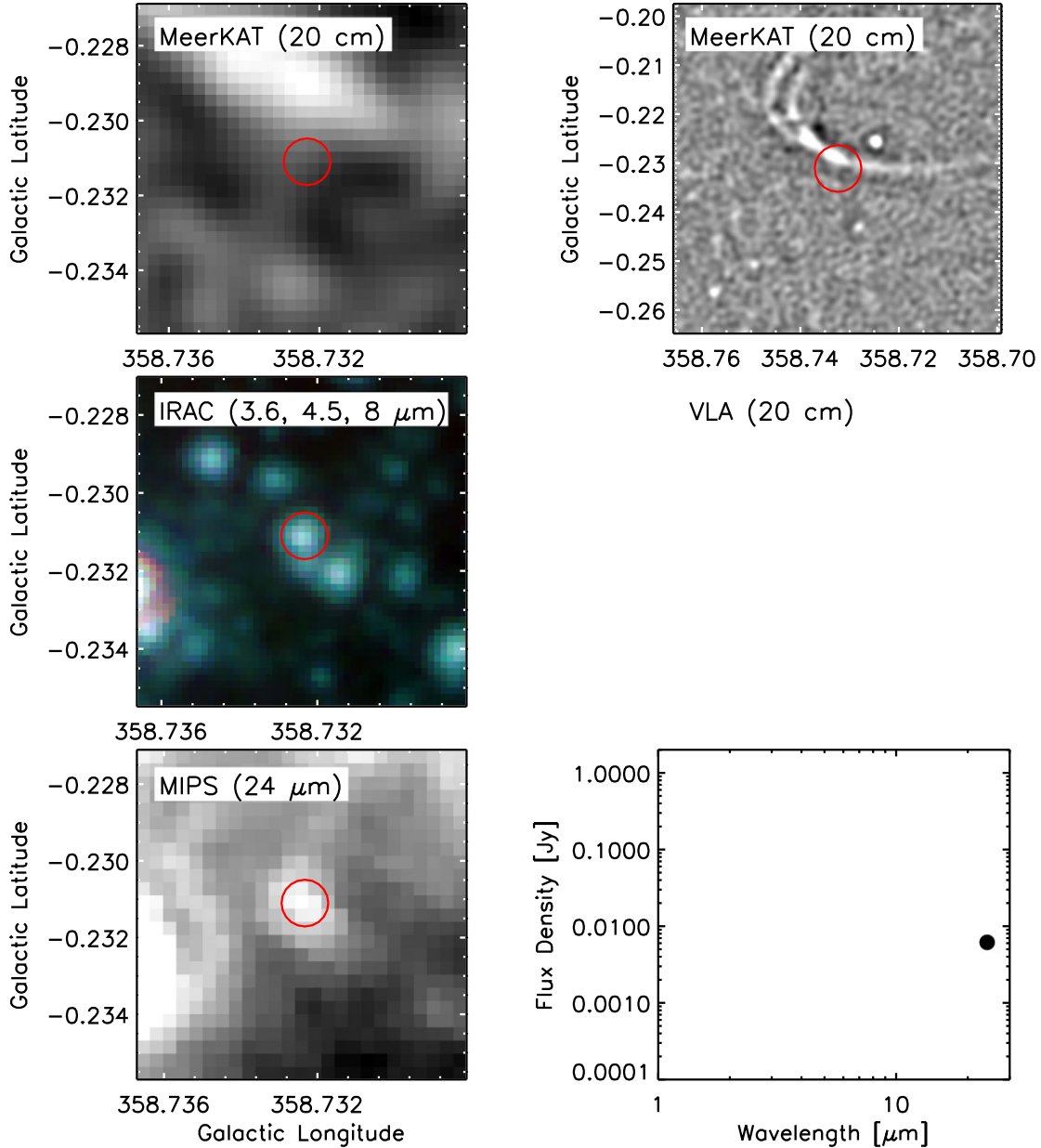


Figure 3. – (a) Each candidate radio source numbered 1–57 in Table 1 is shown in six separate panels. The left-hand column shows a narrow view of, a composite narrow view of IRAC 3.6, 4.5, 8 μm images, and a narrow view of MIPS 24 μm images from top to bottom, respectively. The right-hand column shows a wider view of MeerKAT image images (filtered to highlight filaments, (Yusef-Zadeh et al. 2022a)), unfiltered VLA image (if available), and the SED using 2MASS+IRAC + MIPS data, (black symbols: Ramirez et al. 2008; Hinz et al. 2009). Red stars indicate measurements from the GLIMPSE II Spring '08 Archive (Benjamin et al. 2003). Error bars are plotted for all measurements, but are generally smaller than the symbol size. 2MASS 95 per cent confidence upper limits are now plotted as downward triangles. Upper limits are not stated in the other catalogues on a source-by-source basis. Red circles in the image panels show the positions where the IR SED, the nearest source to the peak radio position, is measured.

the directions away from the source motion and the nuclear wind.

4 SUMMARY

This short paper provides a catalogue of the positions of radio and infrared sources that lie along groups of NFRs that have recently been identified. These sources could potentially be associated with radio filaments. We have displayed radio and IR images of 57 filaments as well as the SEDs of stellar sources coincident with radio sources. A

true physical association will support a picture in which the compact radio sources are a byproduct of a large-scale nuclear wind interacting with stellar systems, thus producing cometary tails that trace NRFs. Near- to mid- IR SEDs illustrate the various classes of sources that appear to be associated with the radio filaments. A trend we notice is the SEDs of mass-losing dusty red giants with strong 24 μm emission, or in some cases young, massive stars. Future high-resolution radio and infrared observations of the candidate sources are needed to establish their true association with NRFs, thus testing cometary tail model.

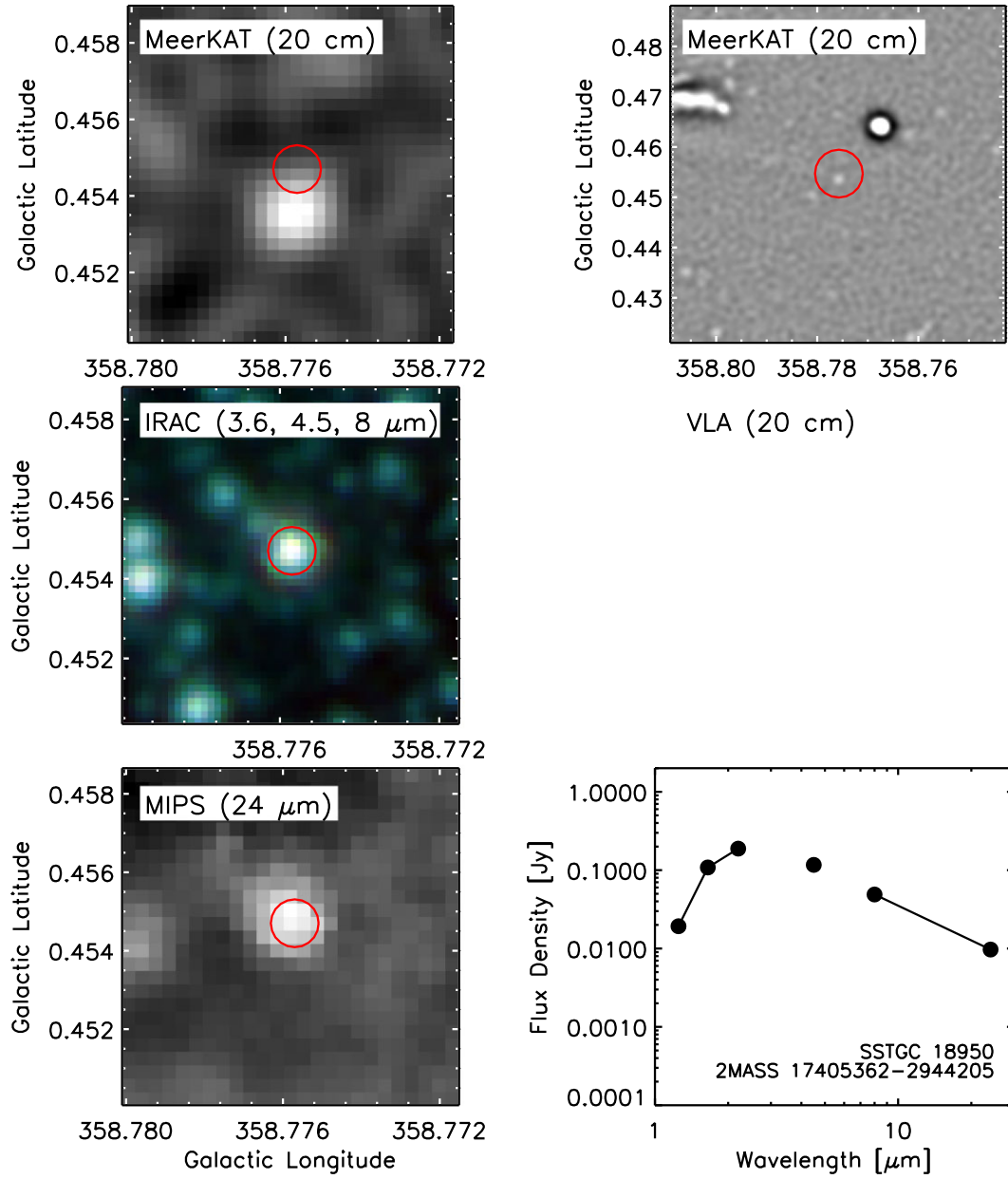


Figure 3. – (b) Same as Fig. 3(a) except for source 2 in Table 1. Open circles indicate potentially saturated IRAC measurements.

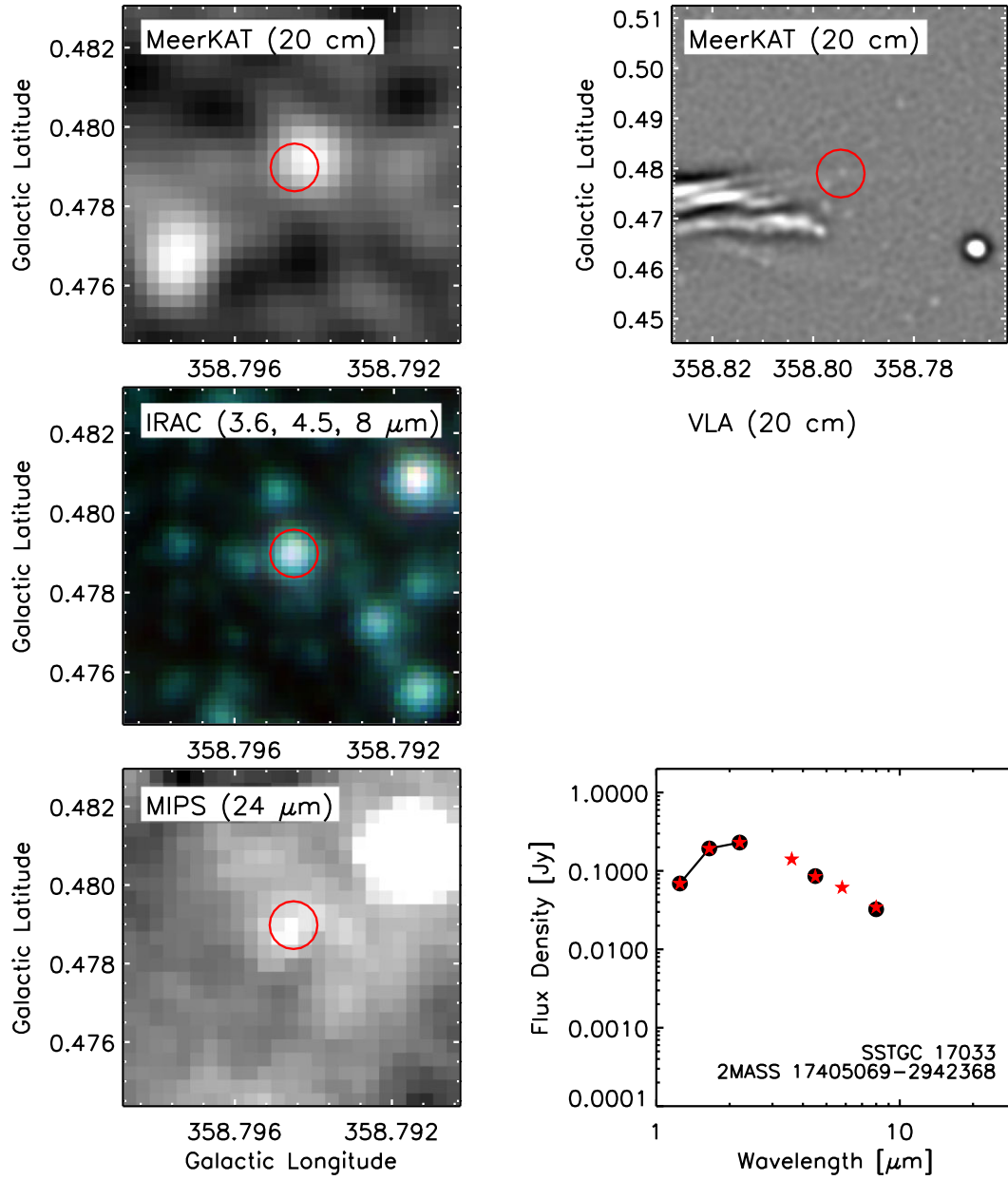


Figure 3. – (c) Same as Fig. 3(a) except for source 3 Table 1.

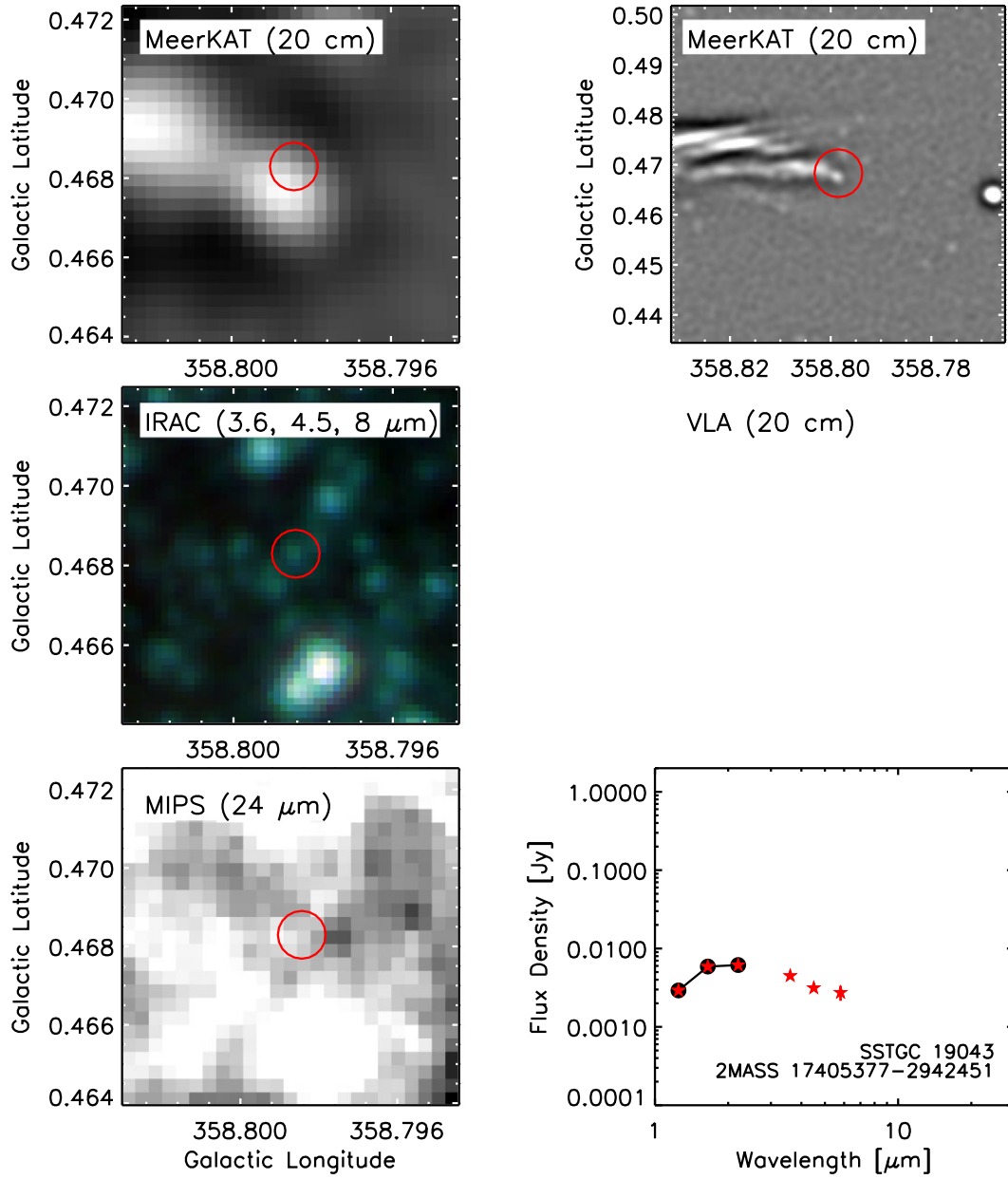


Figure 3. – (d) Same as Fig. 3(a) except for source 4 in Table 1.

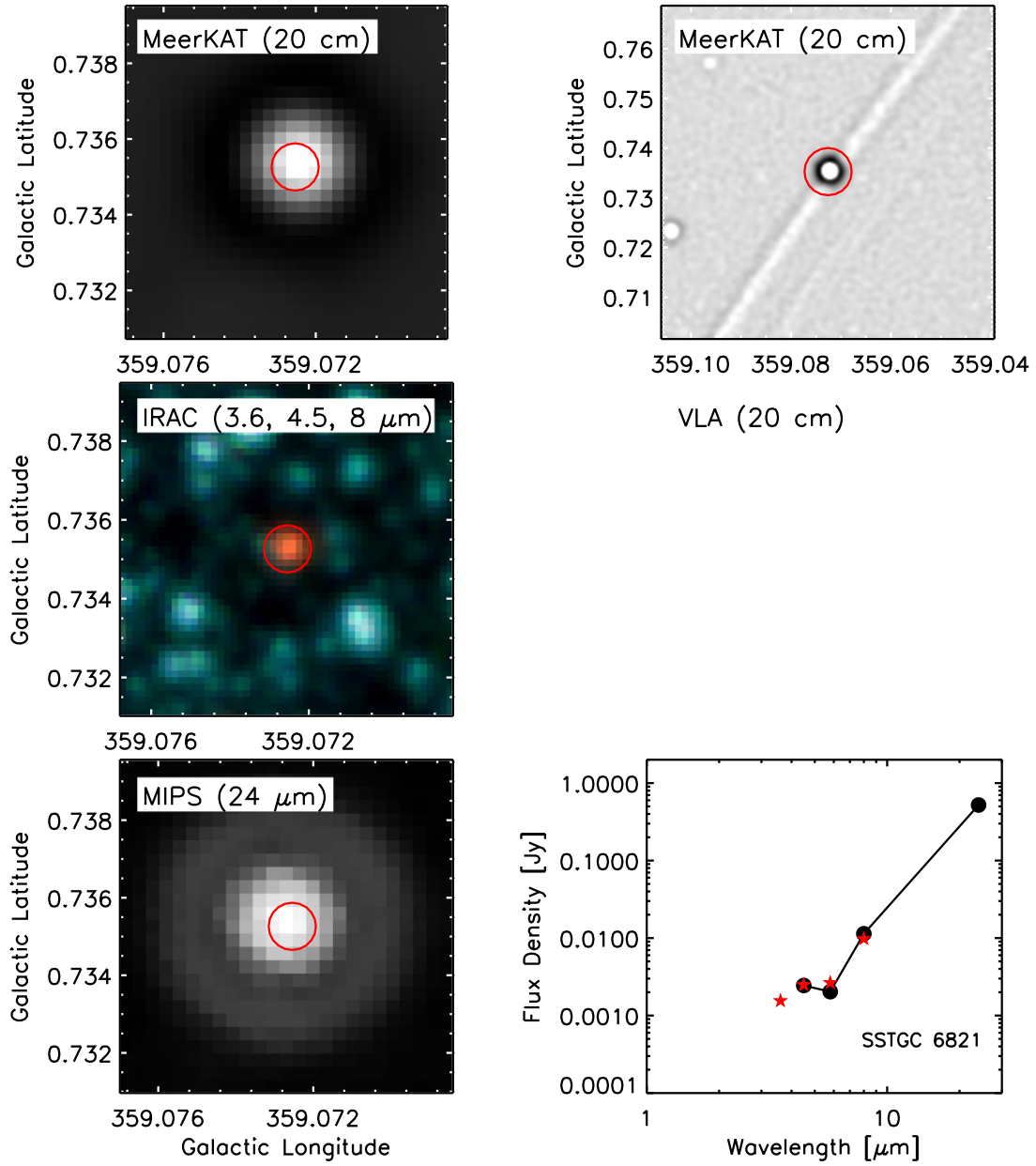


Figure 3. – (e) Same as Fig. 3(a) except for source 5 in Table 1.

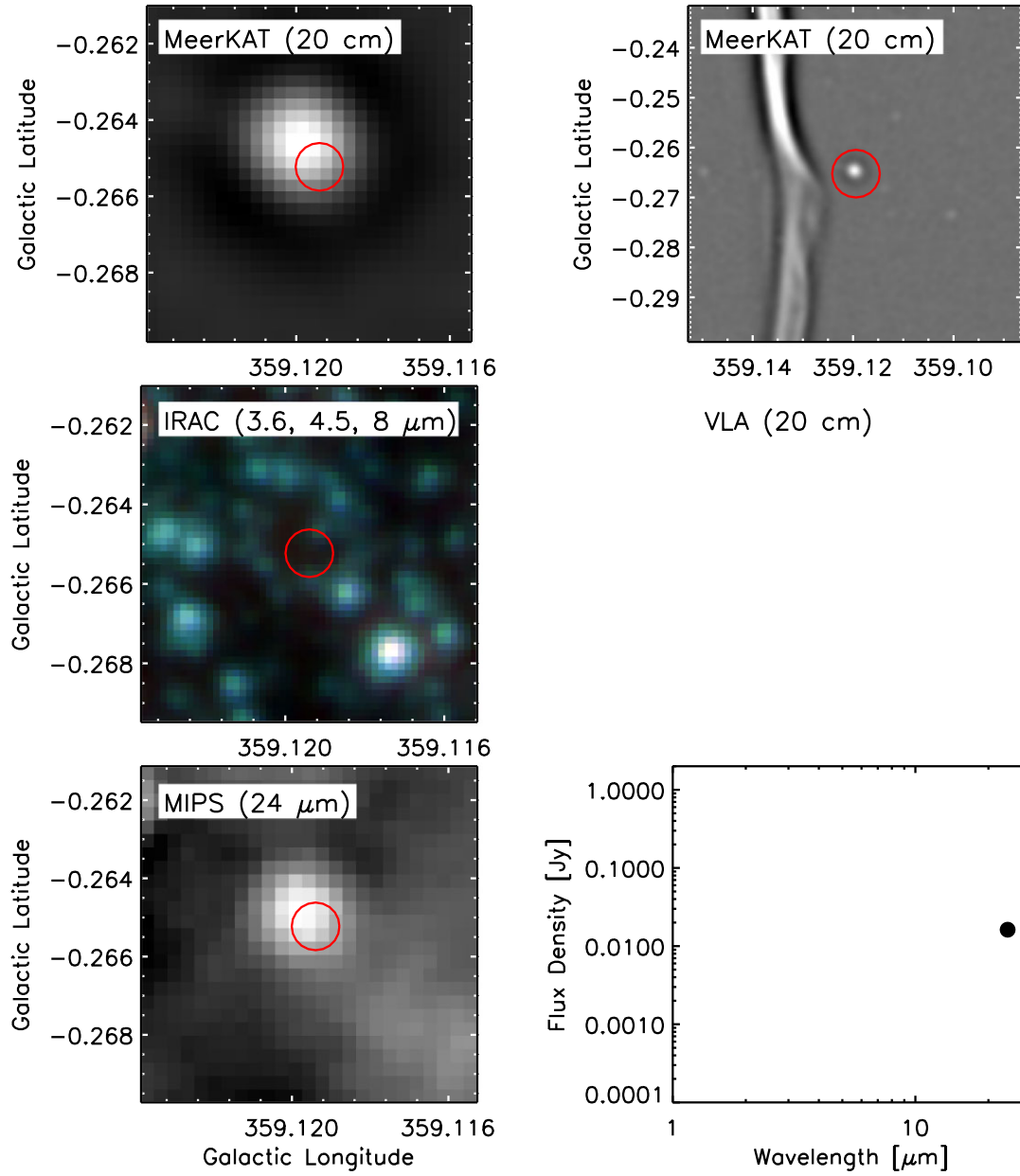


Figure 3. – (f) Same as Fig. 3(a) except for source 6 in Table 1.

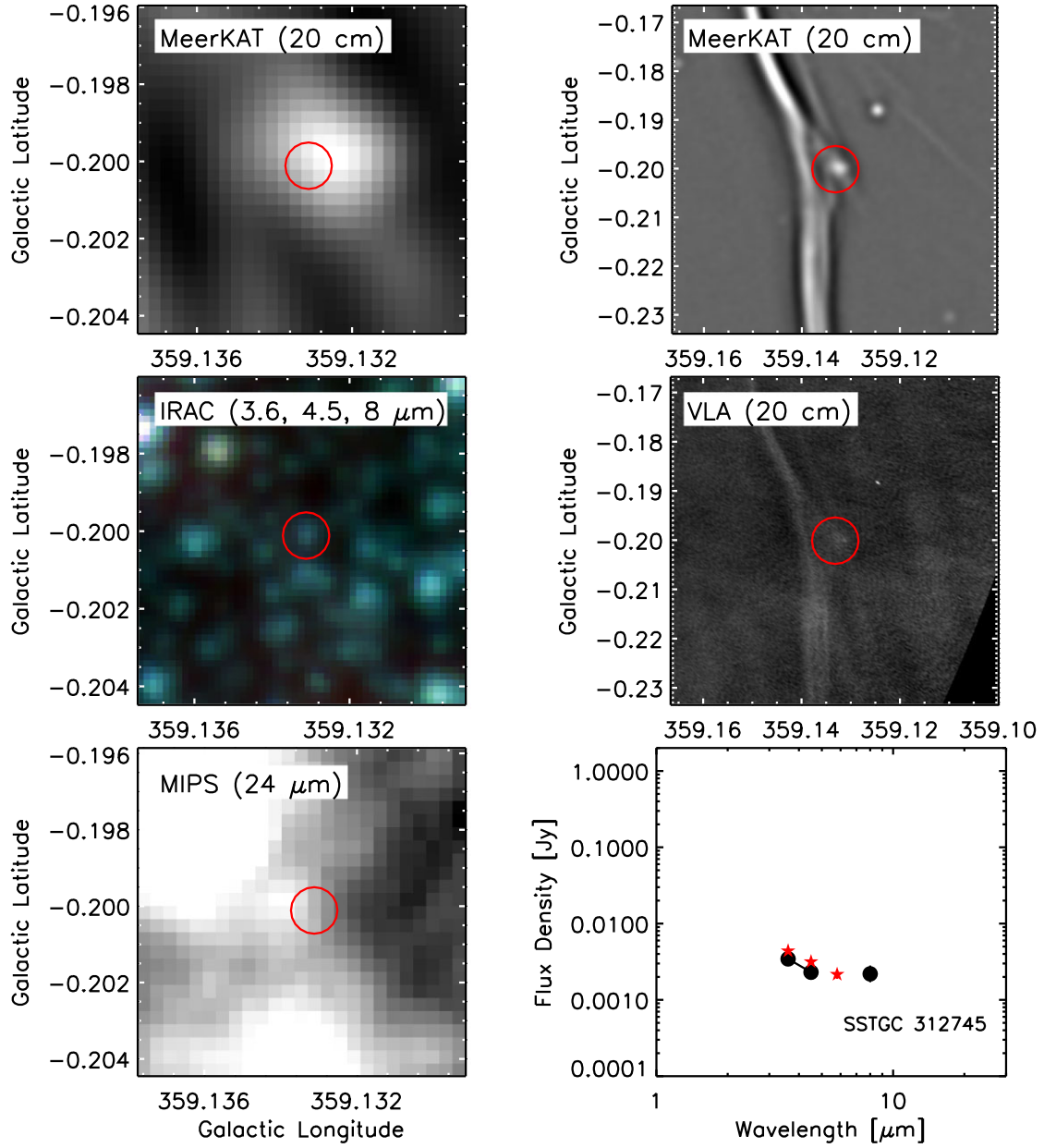


Figure 3. – (g) Same as Fig. 3(a) except for source 7 in Table 1.

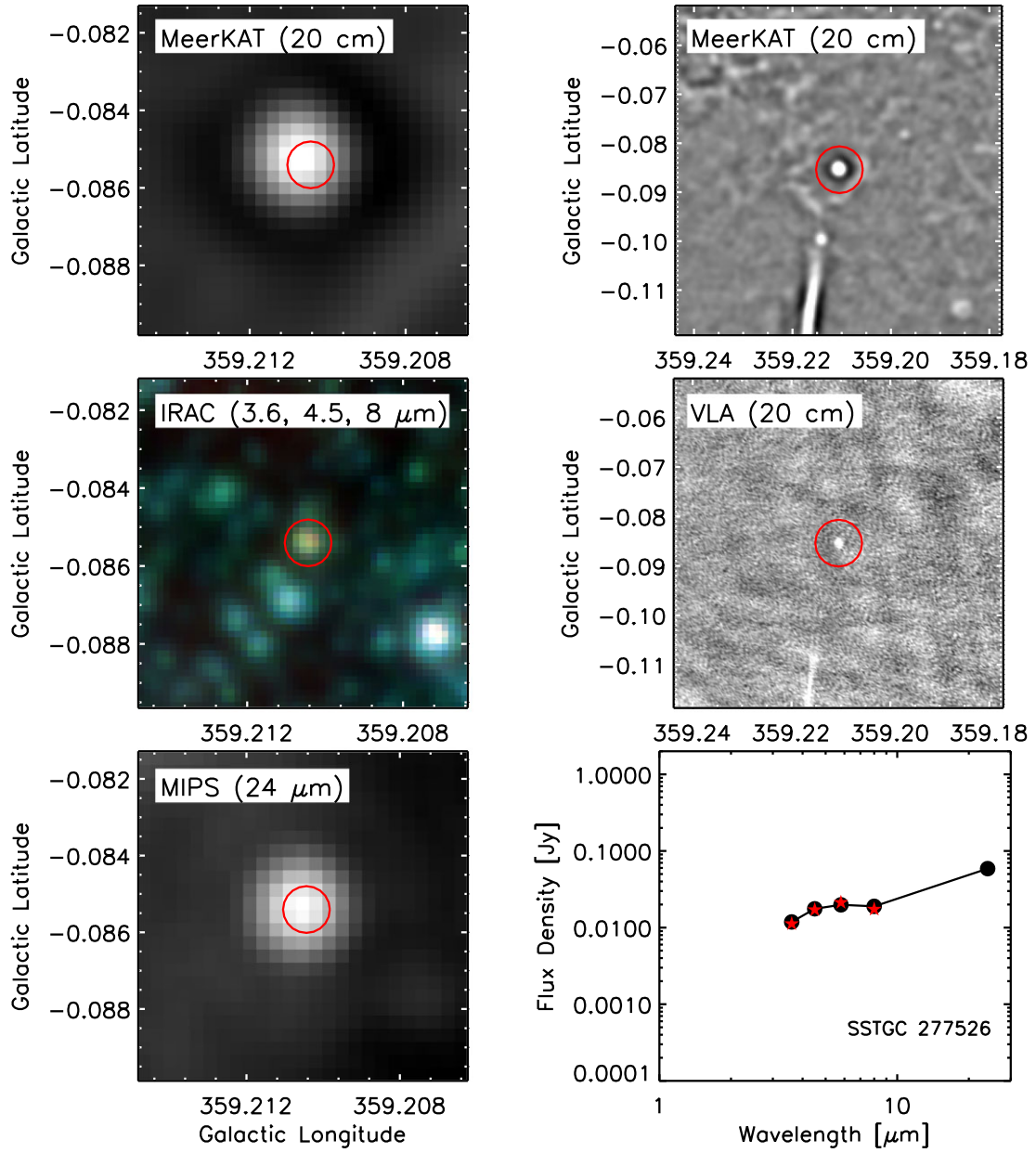


Figure 3. – (h) Same as Fig. 3(a) except for source 8 in Table 1.

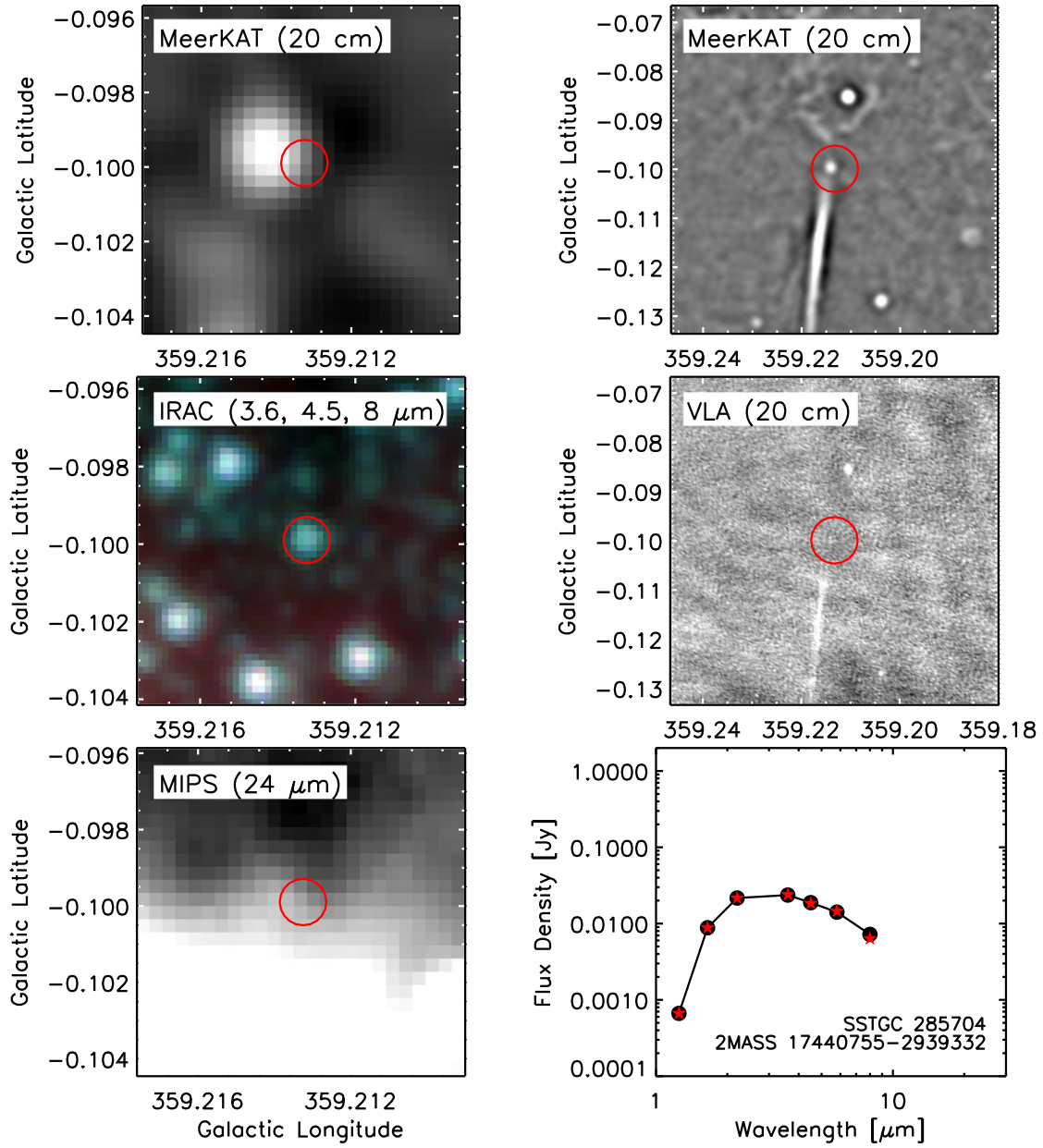


Figure 3. – (i) Same as Fig. 3(a) except for source 9 in Table 1.

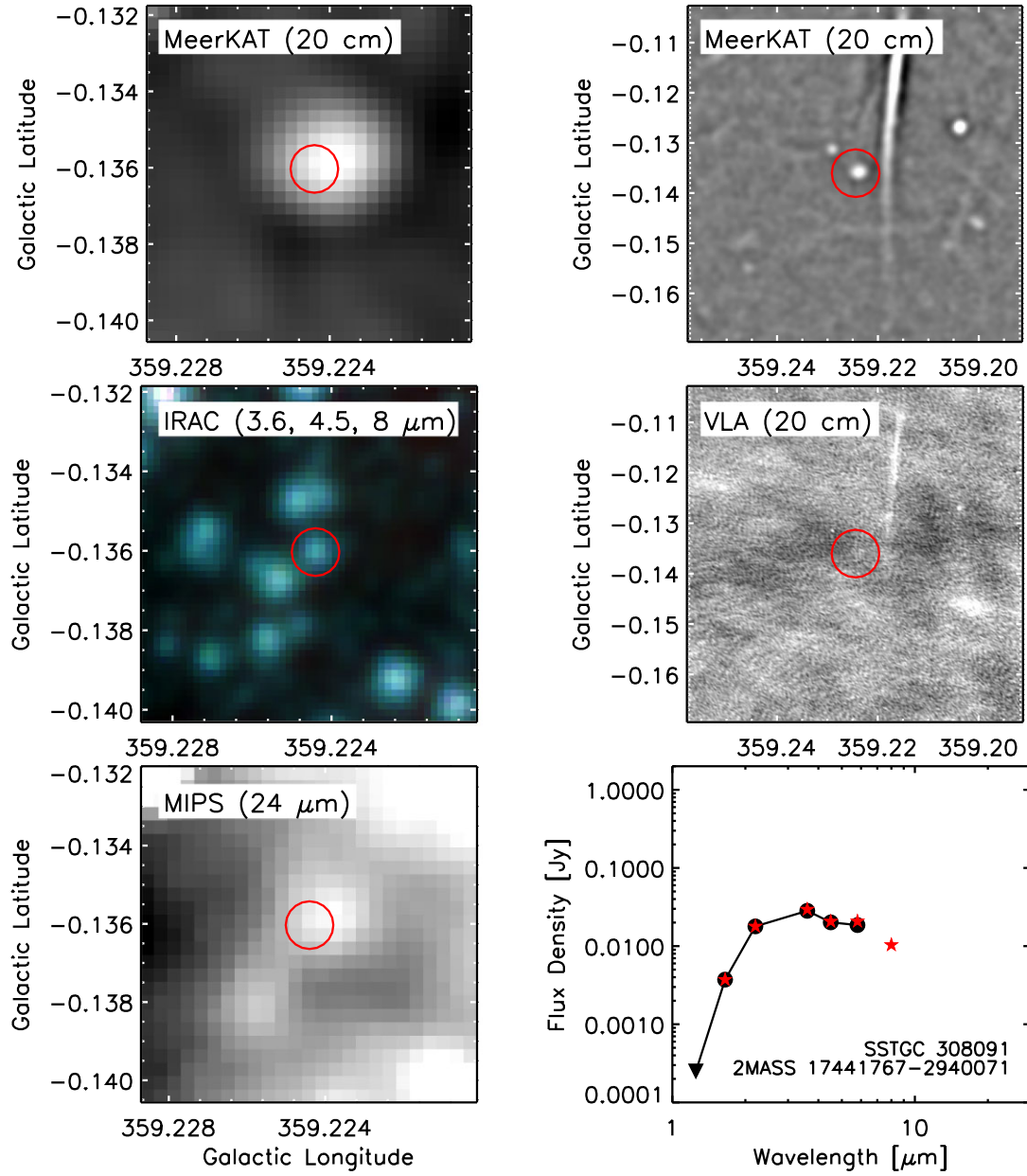


Figure 3. – (j) Same as Fig. 3(a) except for source 10 in Table 1.

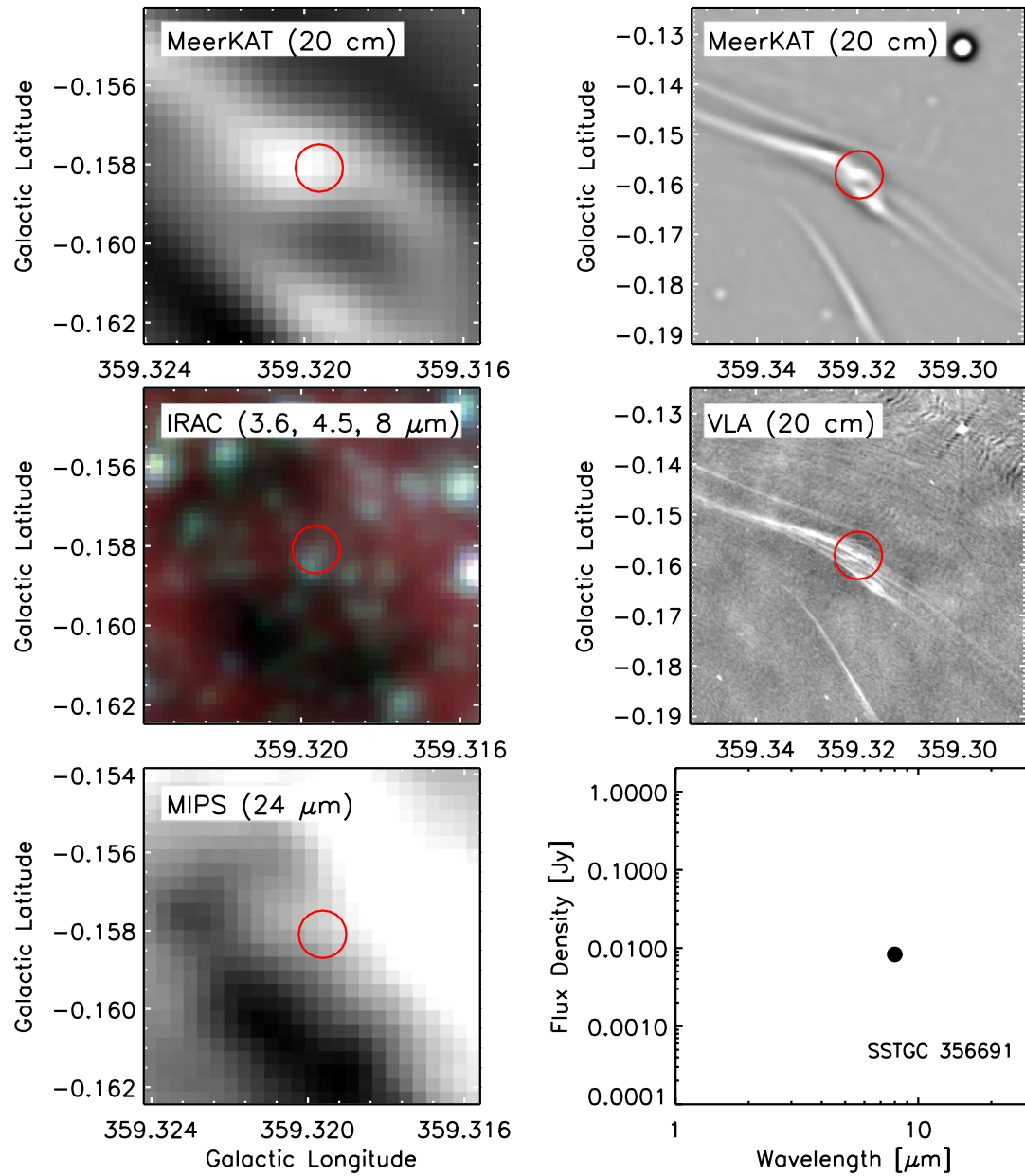


Figure 3. – (k) Same as Fig. 3(a) except source 11 in Table 1.

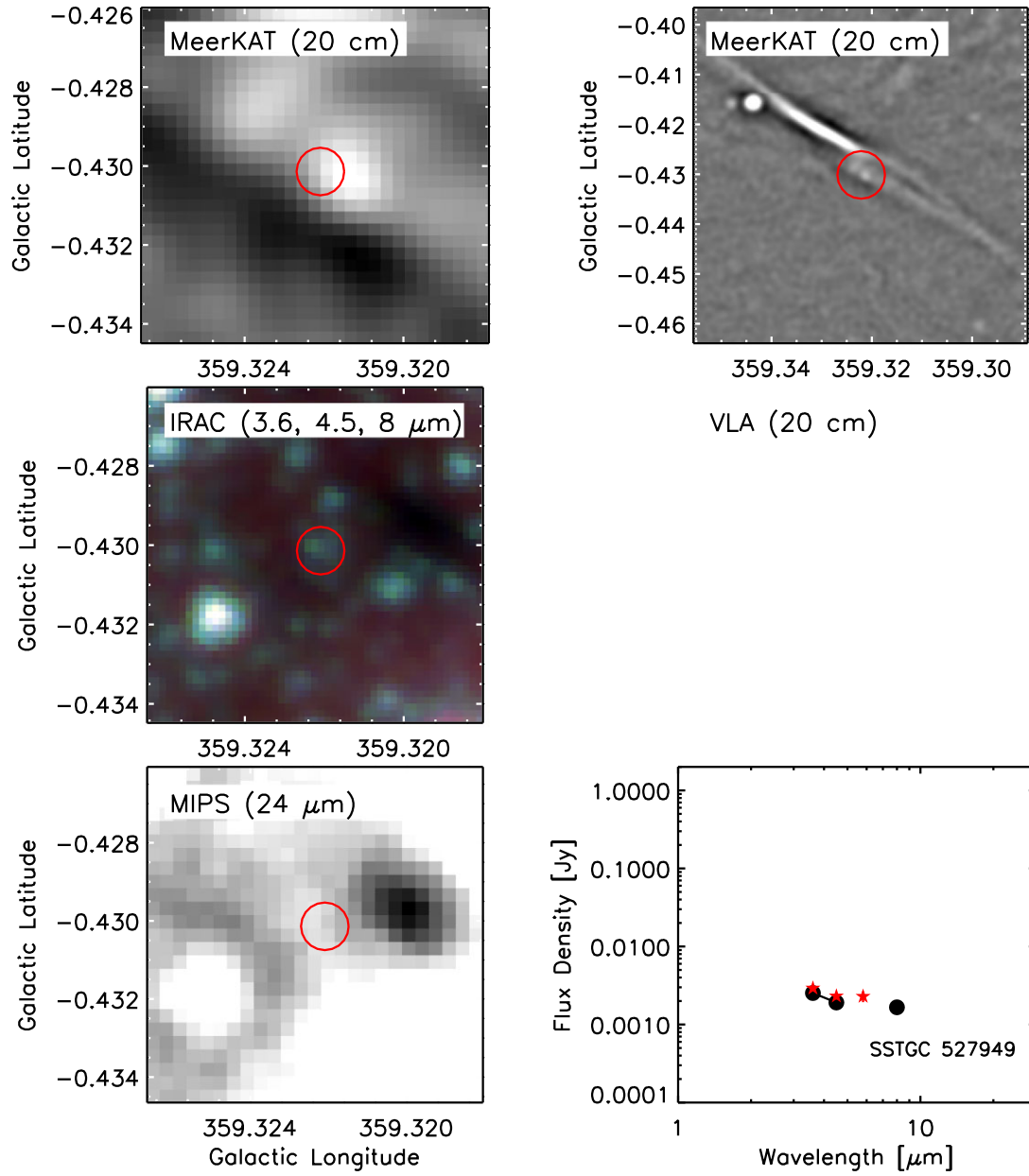


Figure 3. – (l) Same as Fig. 3(a) except source 12 in Table 1.

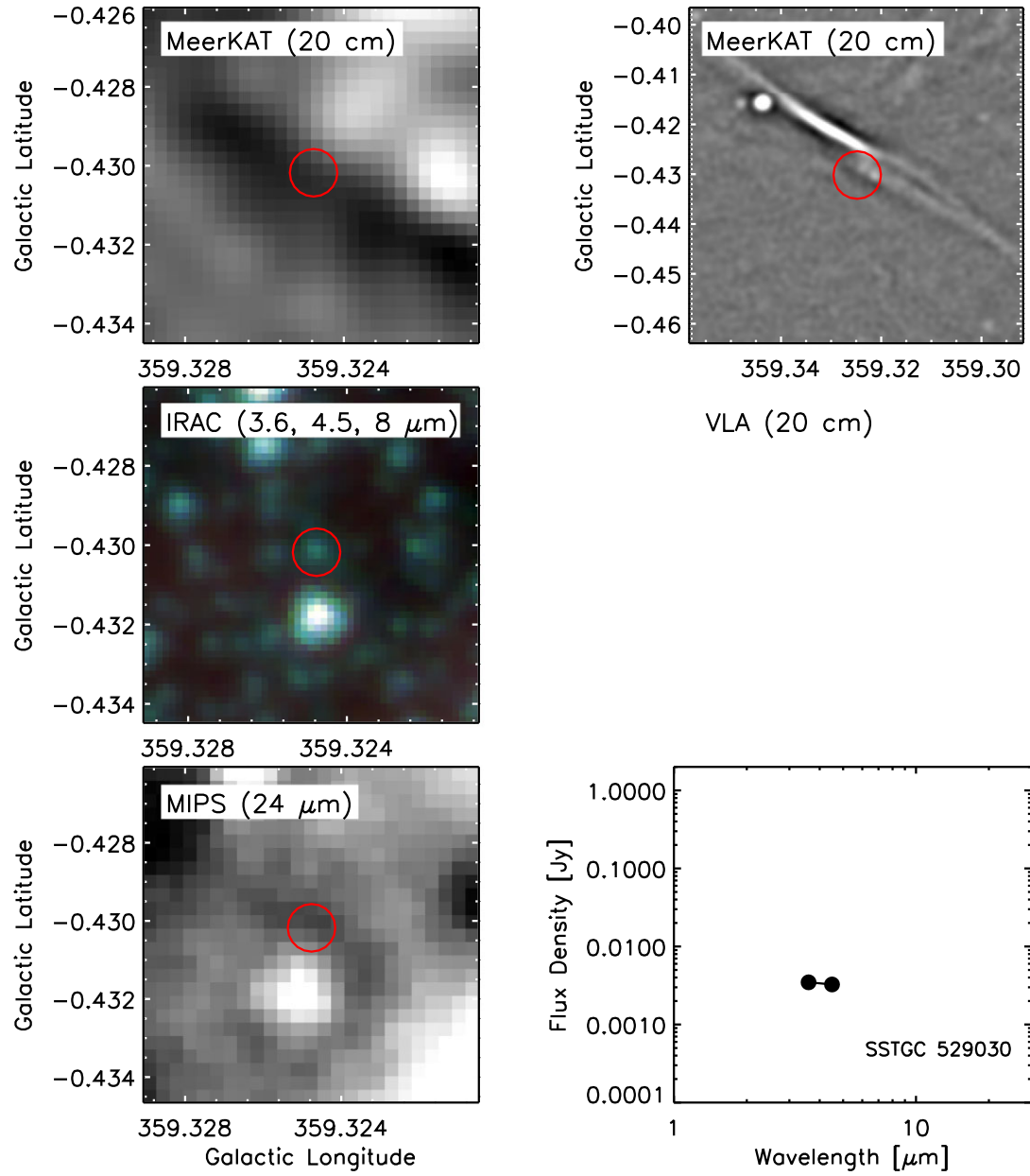


Figure 3. – (m) Same as Fig. 3(a) except source 13 in Table 1.

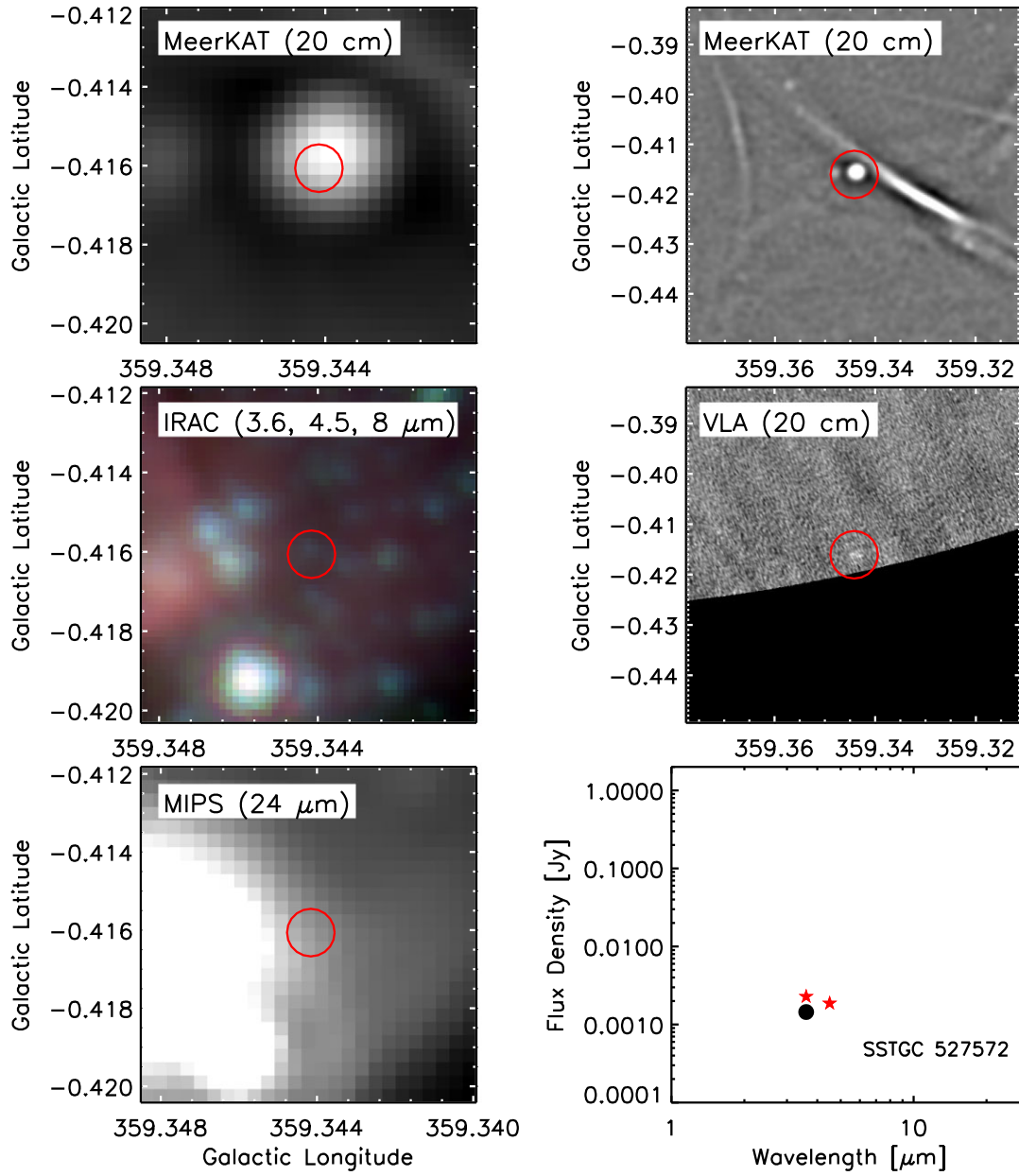


Figure 3. – (n) Same as Fig. 3(a) except source 14 in Table 1.

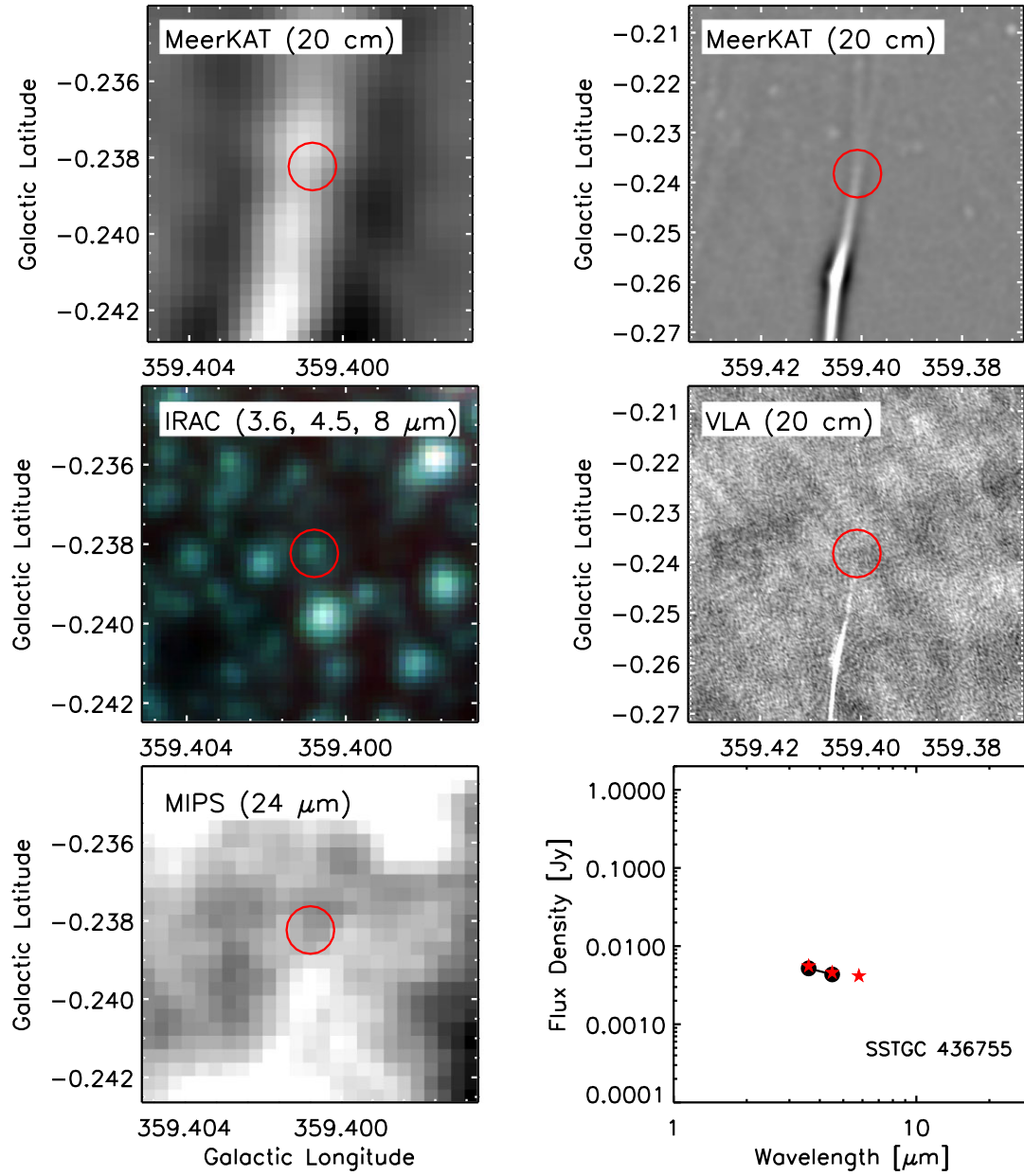


Figure 3. – (o) Same as Fig. 3(a) except source 15 in Table 1.

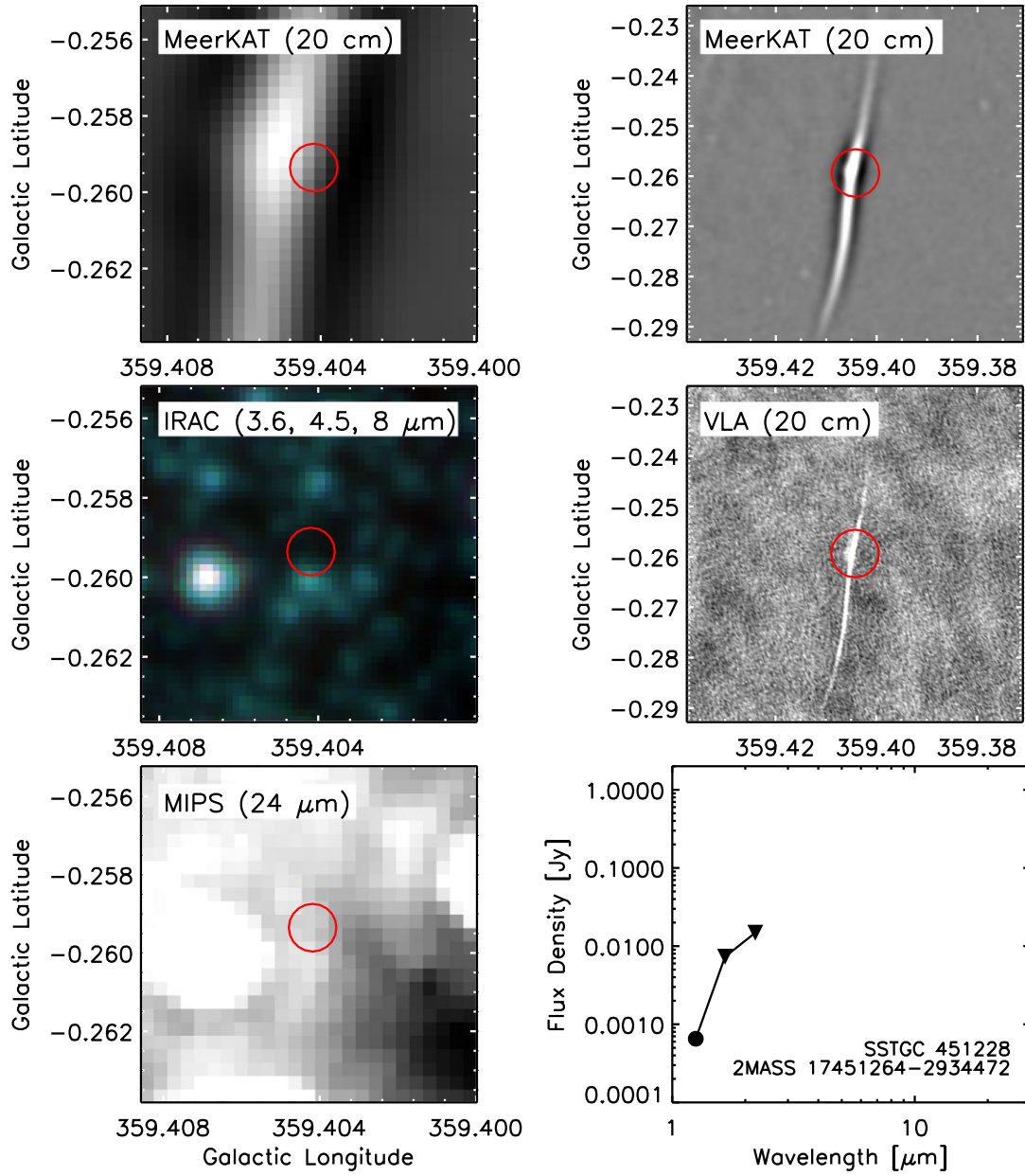


Figure 3. – (p) Same as Fig. 3(a) except source 16 in Table 1.

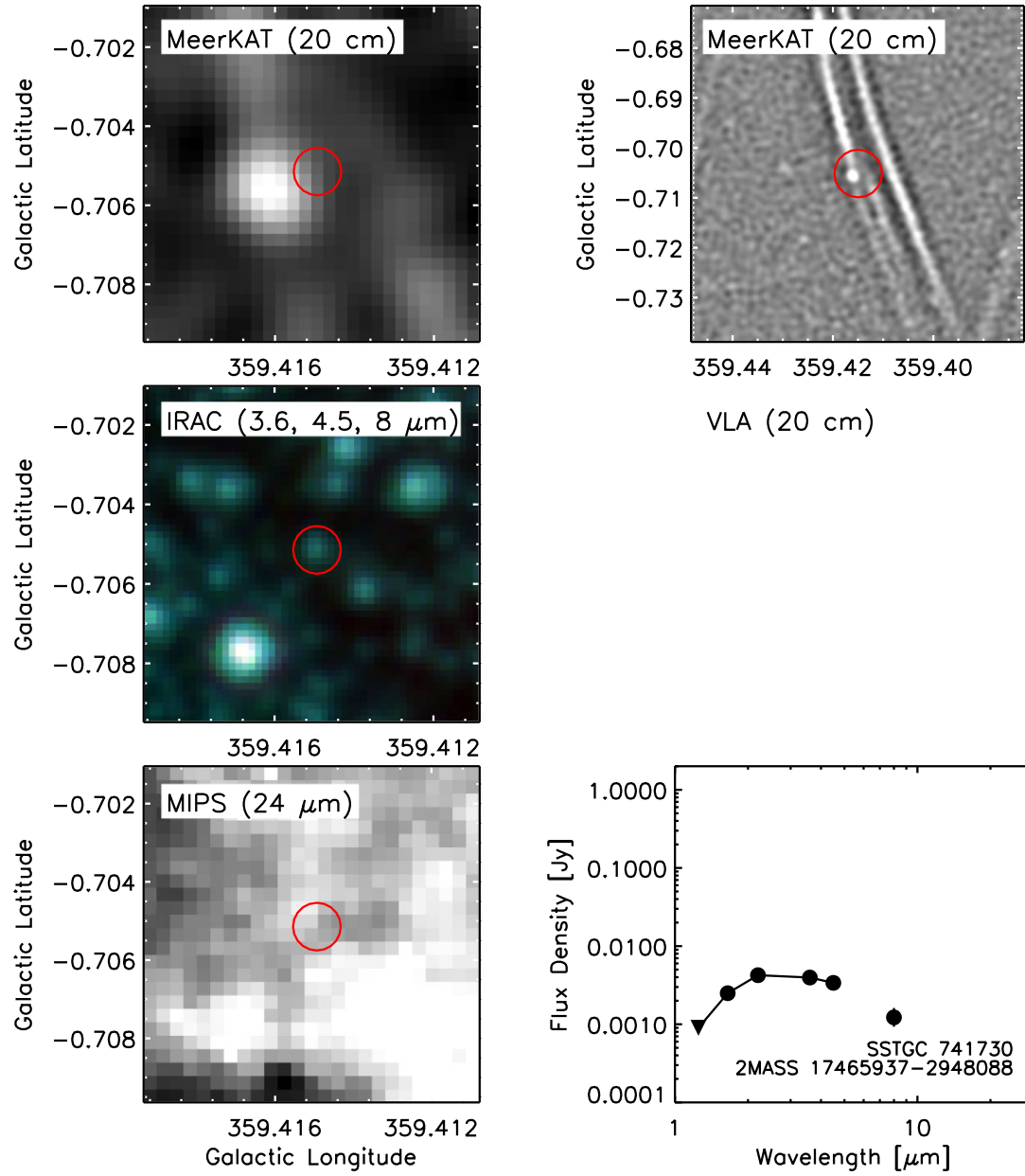


Figure 3. – (q) Same as Fig. 3(a) except source 17 in Table 1.

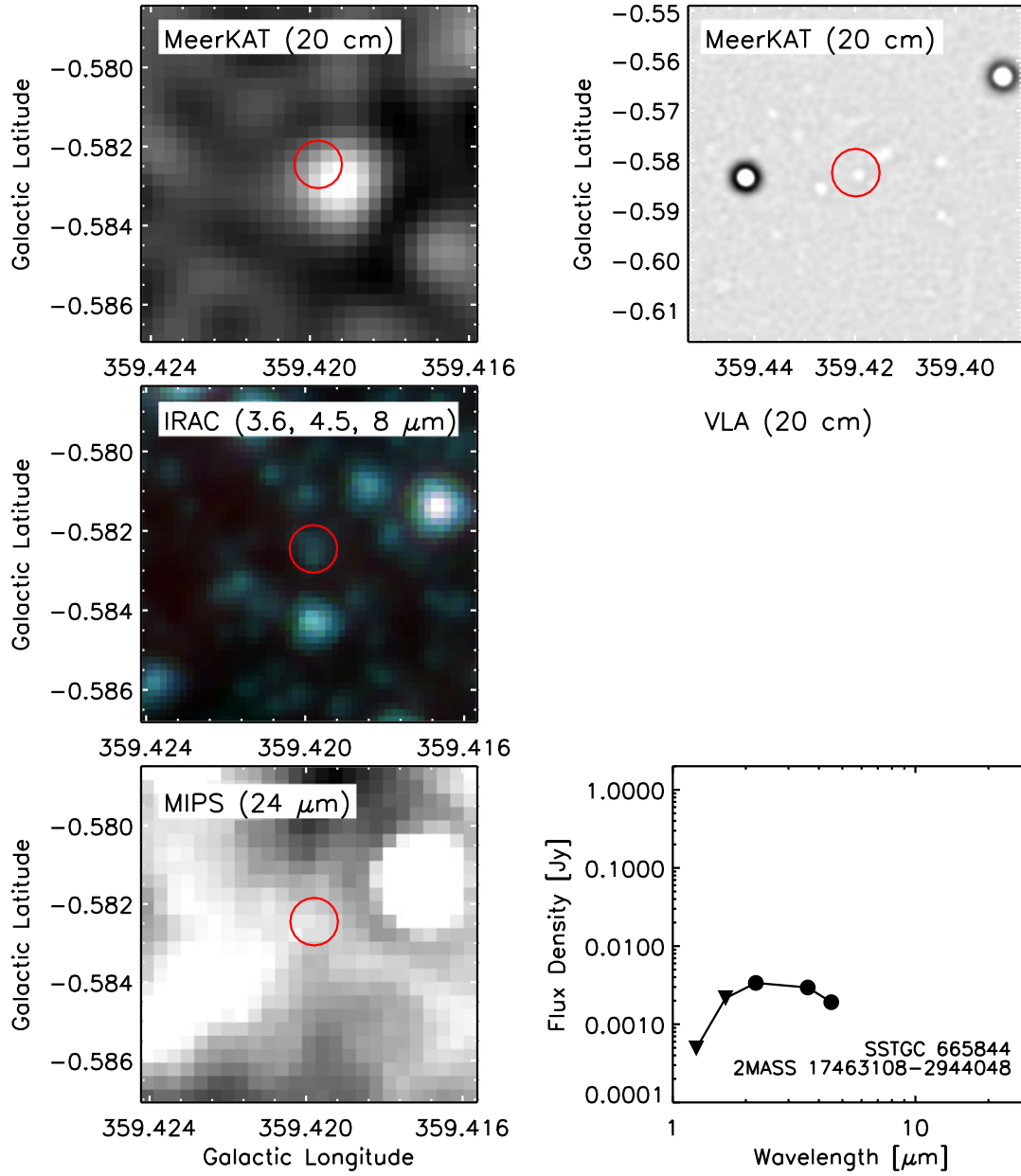


Figure 3. – (r) Same as Fig. 3(a) except source 18 in Table 1.

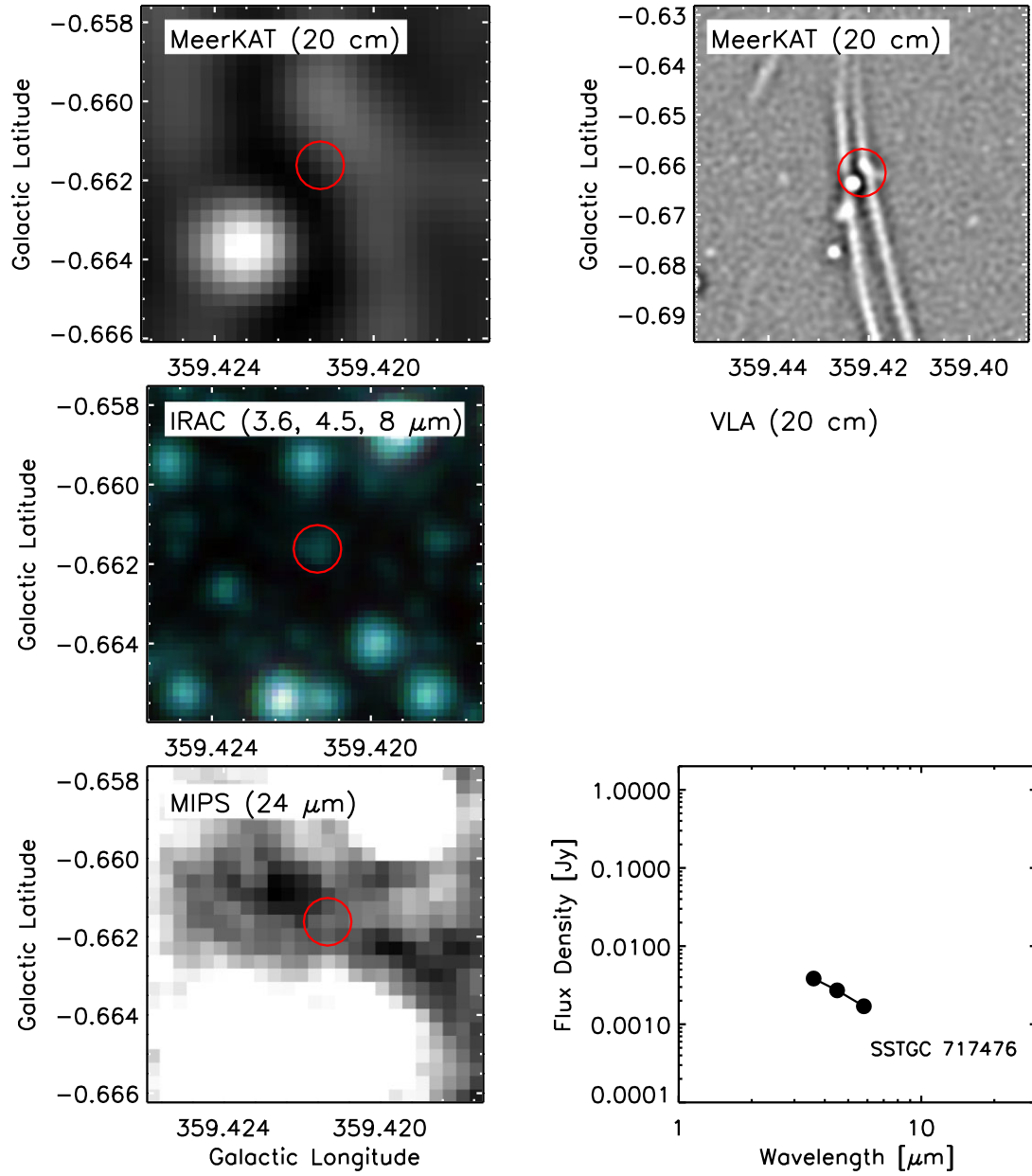


Figure 3. – (s) Same as Fig. 3(a) except source 19 in Table 1.

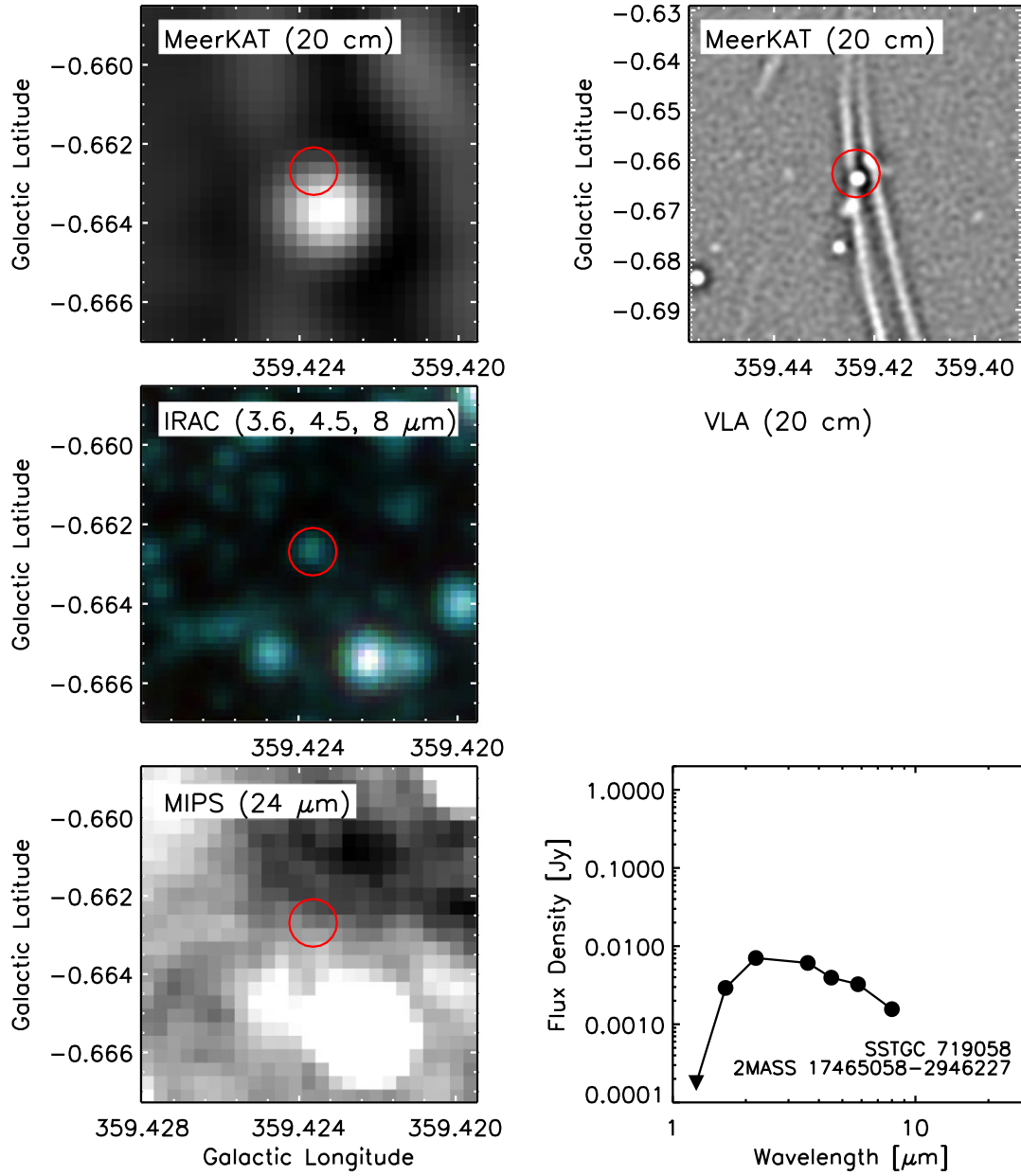


Figure 3. – (t) Same as Fig. 3(a) except source 20 in Table 1.

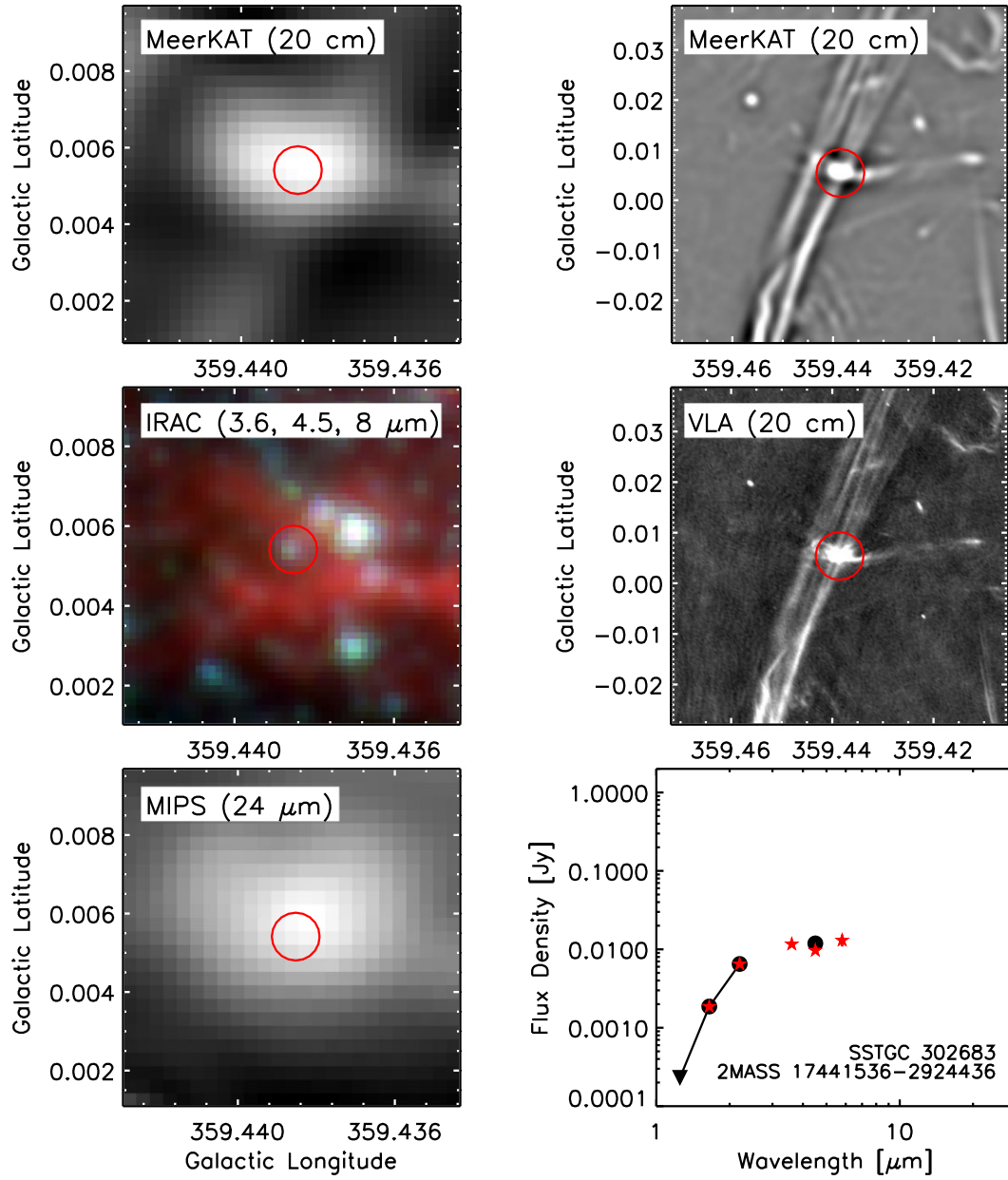


Figure 3. – (u) Same as Fig. 3(a) except source 21 in Table 1.

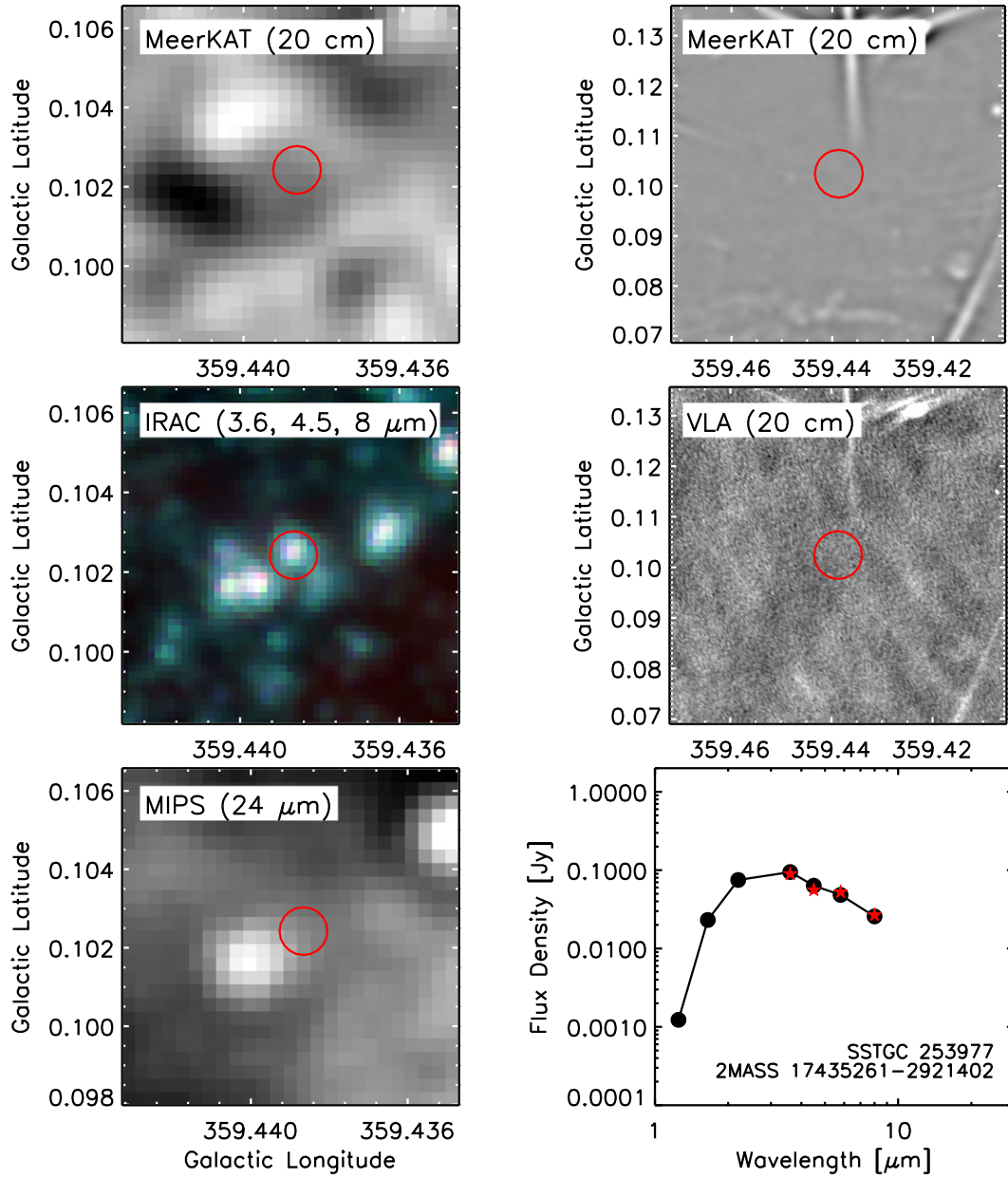


Figure 3. – (v) Same as Fig. 3(a) except source 22 listed in Table 1.

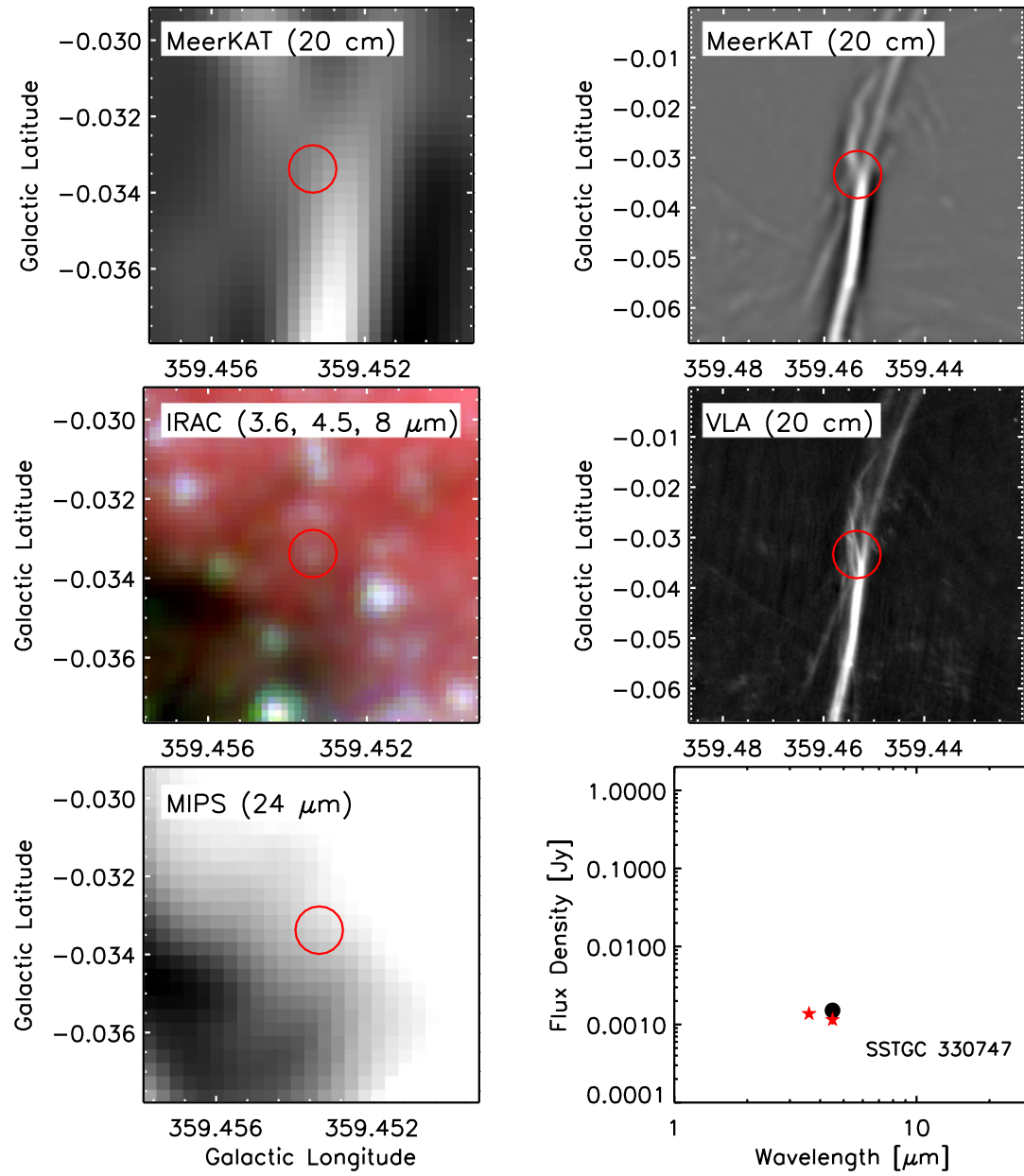


Figure 3. – (w) Same as Fig. 3(a) except source 23 in Table 1.

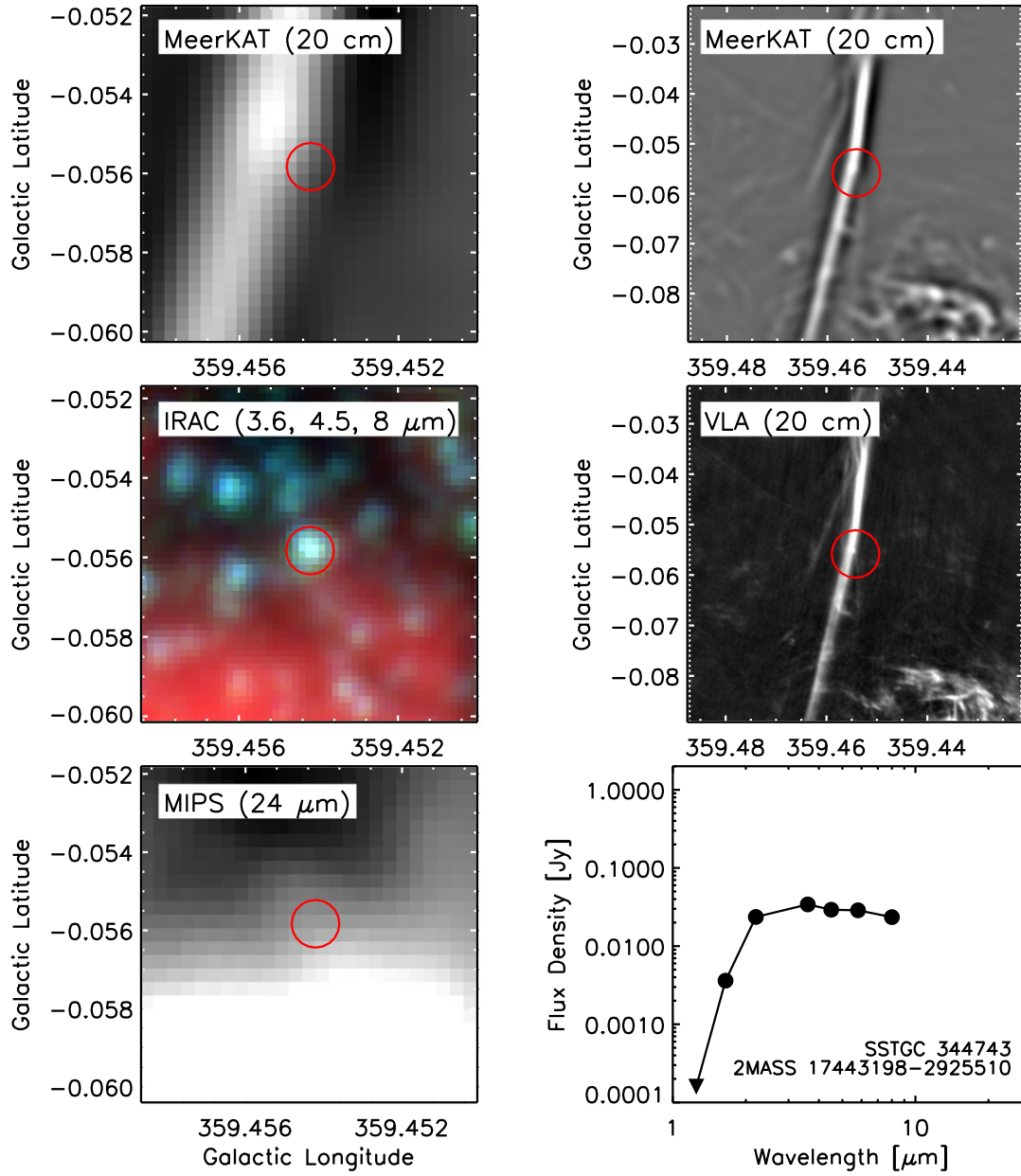


Figure 3. – (x) Same as Fig. 3(a) except source 24 in Table 1.

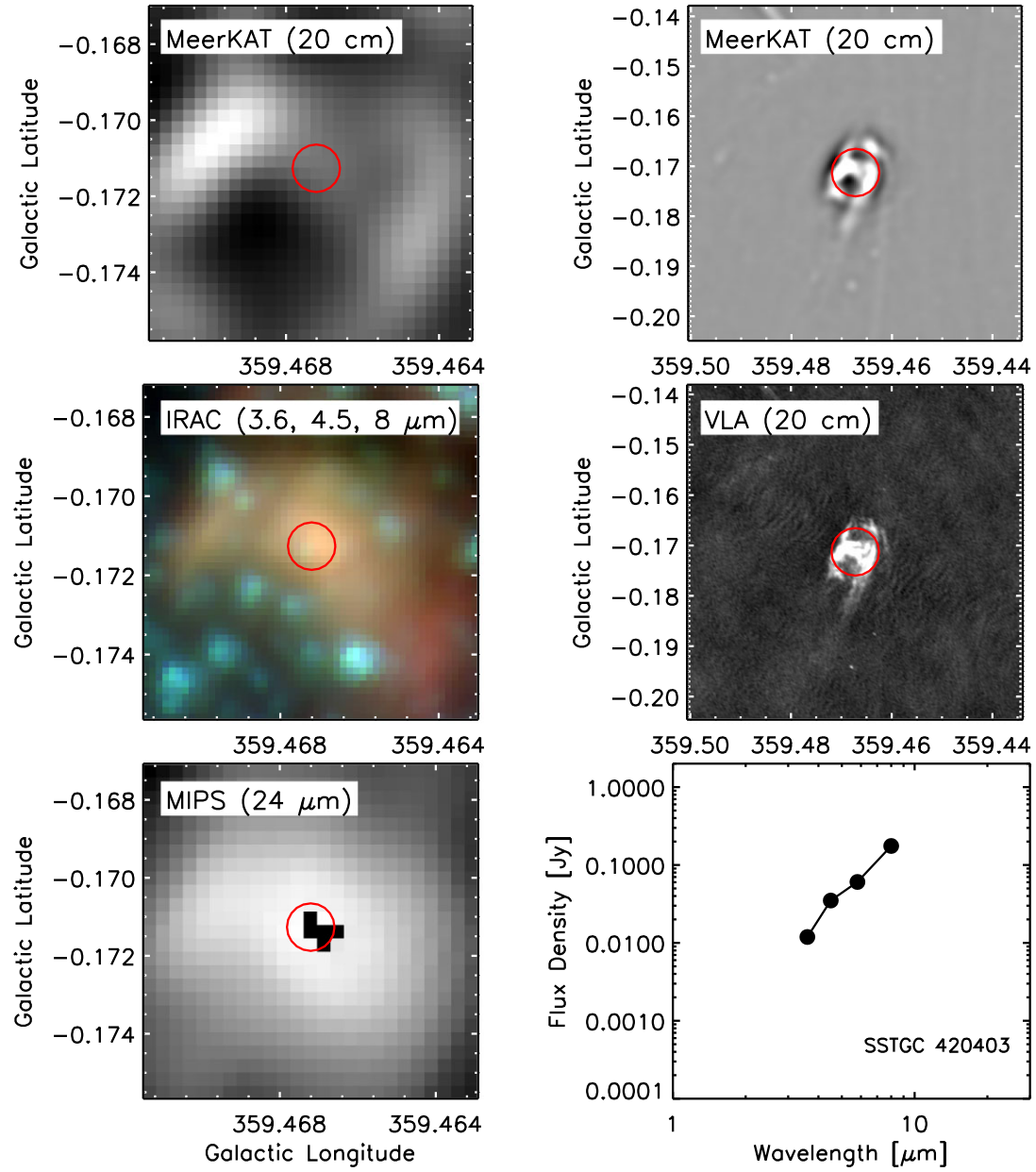


Figure 3. – (y) Same as Fig. 3(a) except source 25 in Table 1.

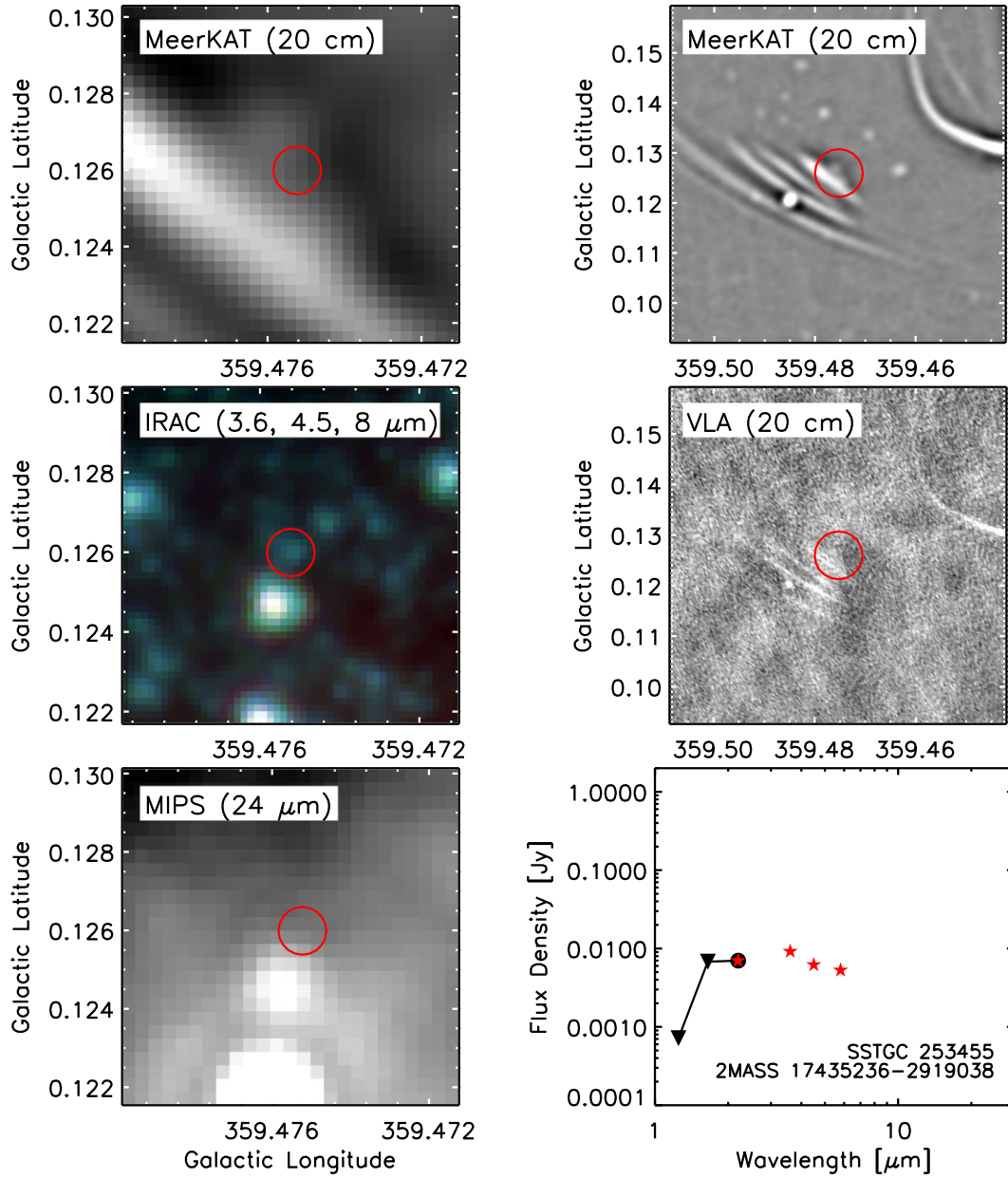


Figure 3. – (z) Same as Fig. 3(a) except source 26 in Table 1.

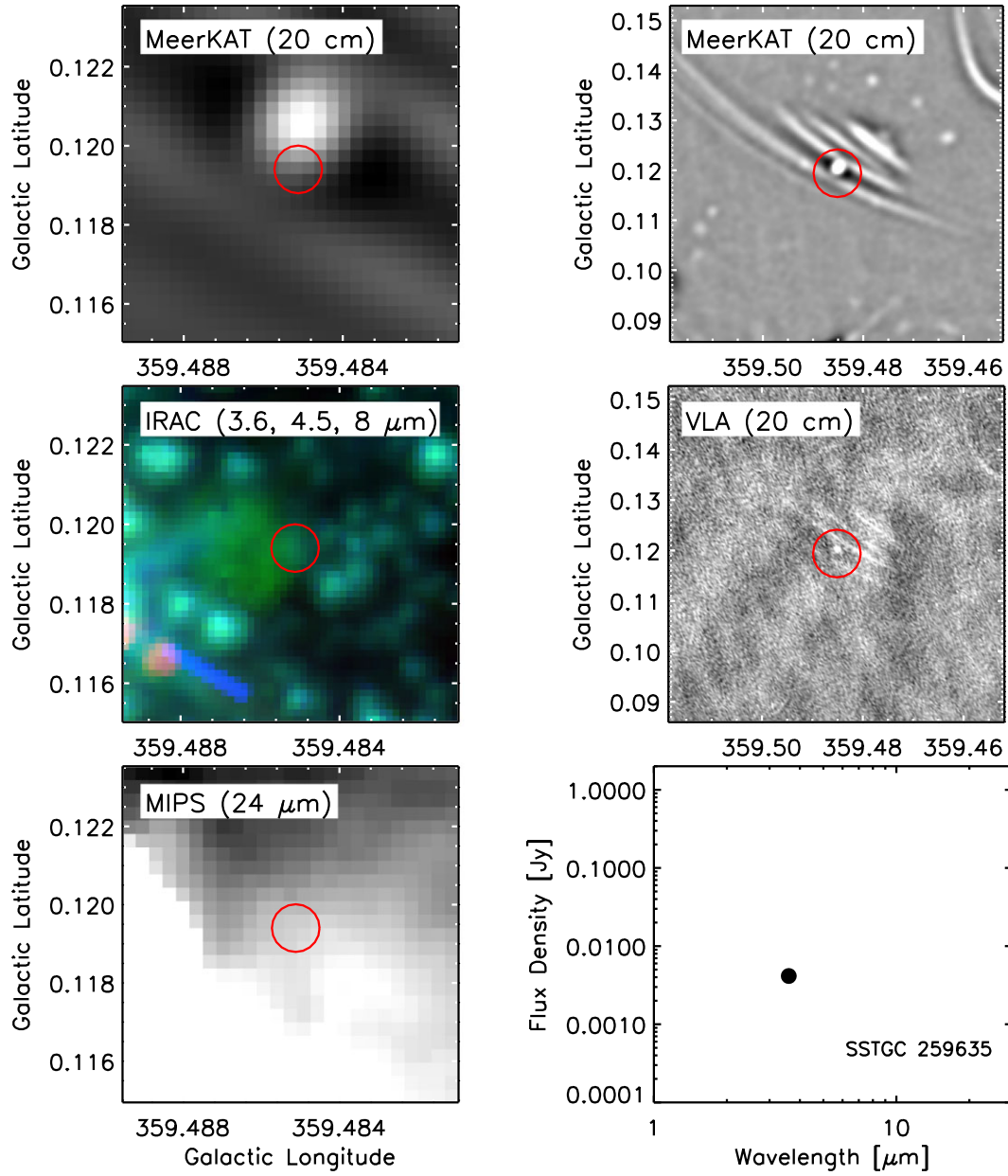


Figure 3. – (aa) Same as Fig. 3(a) except source 27 in Table 1.

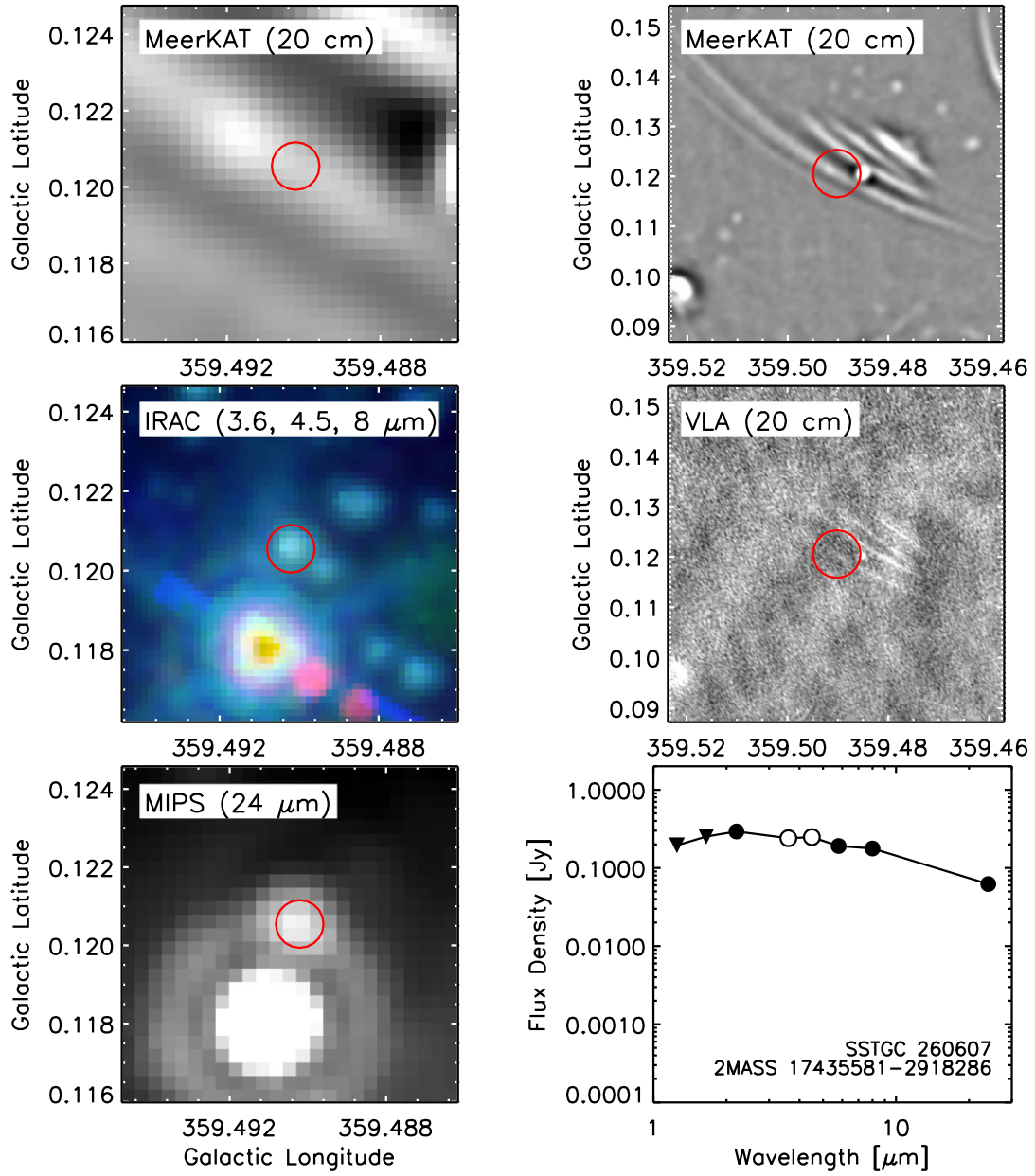


Figure 3. – (bb) Same as Fig. 3(a) except source 28 in Table 1. Open circles indicate potentially saturated IRAC measurements.

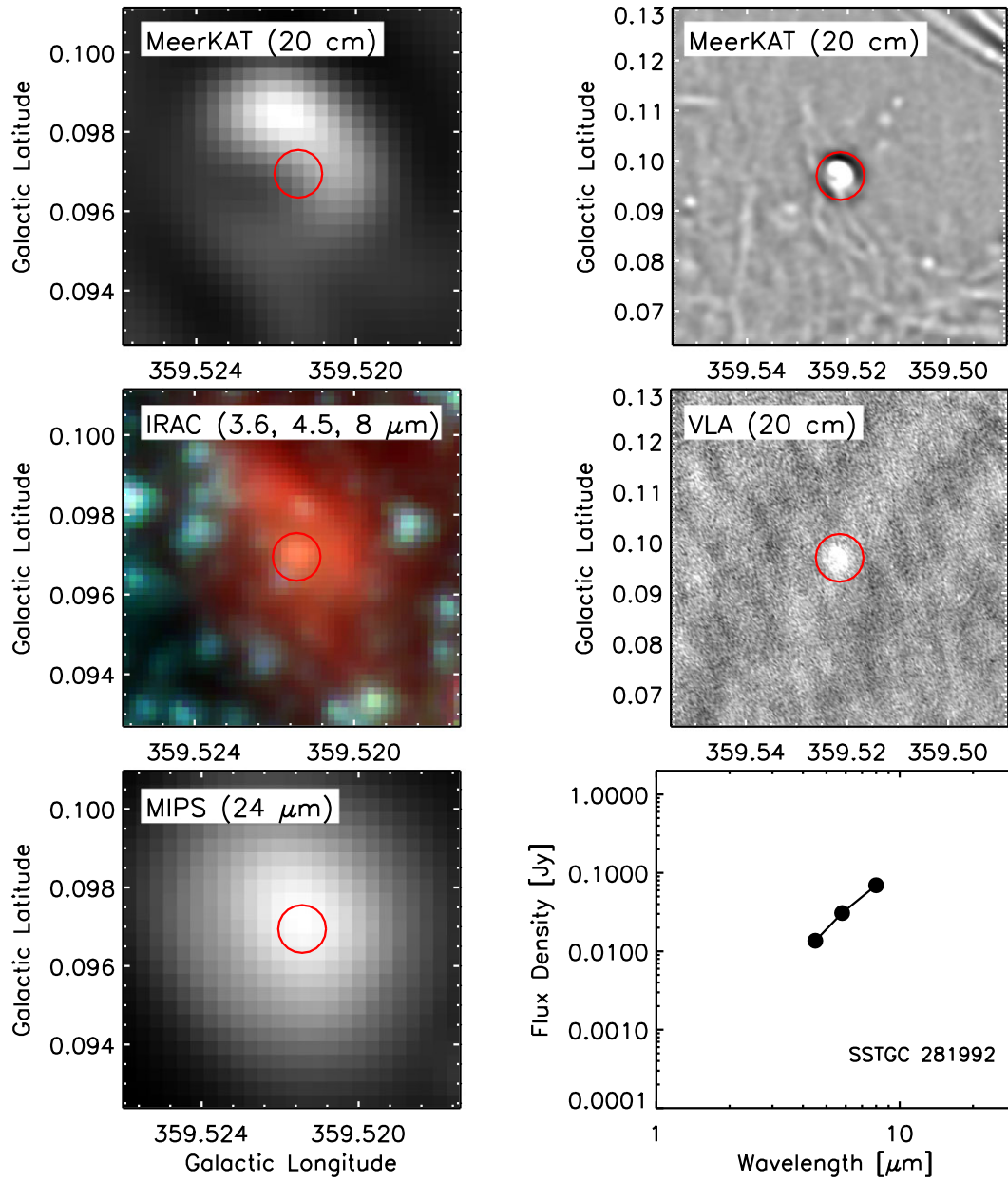


Figure 3. – (cc) Same as Fig. 3(a) except source 29 in Table 1.

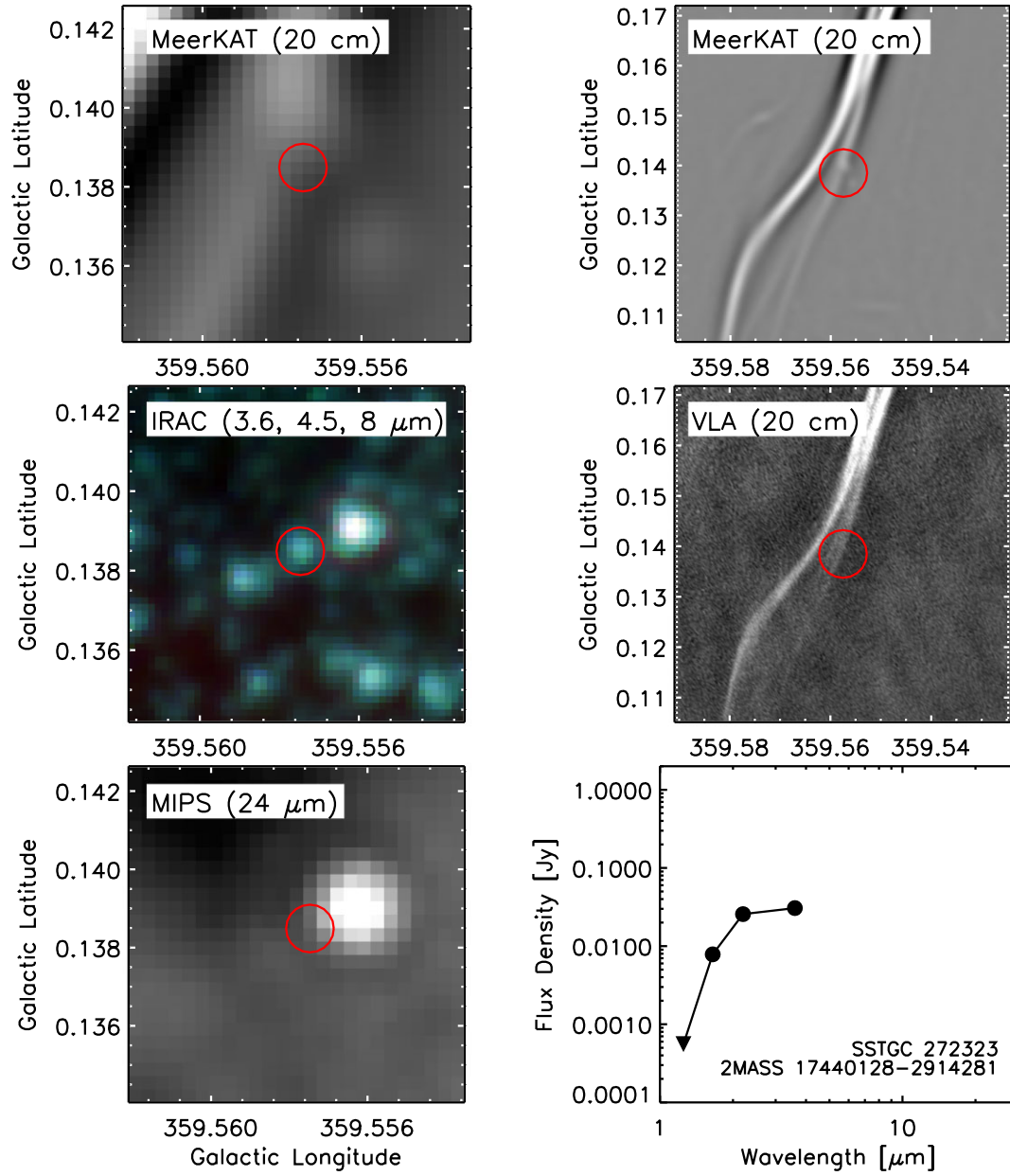


Figure 3. – (dd) Same as Fig. 3(a) except source 30 in Table 1.

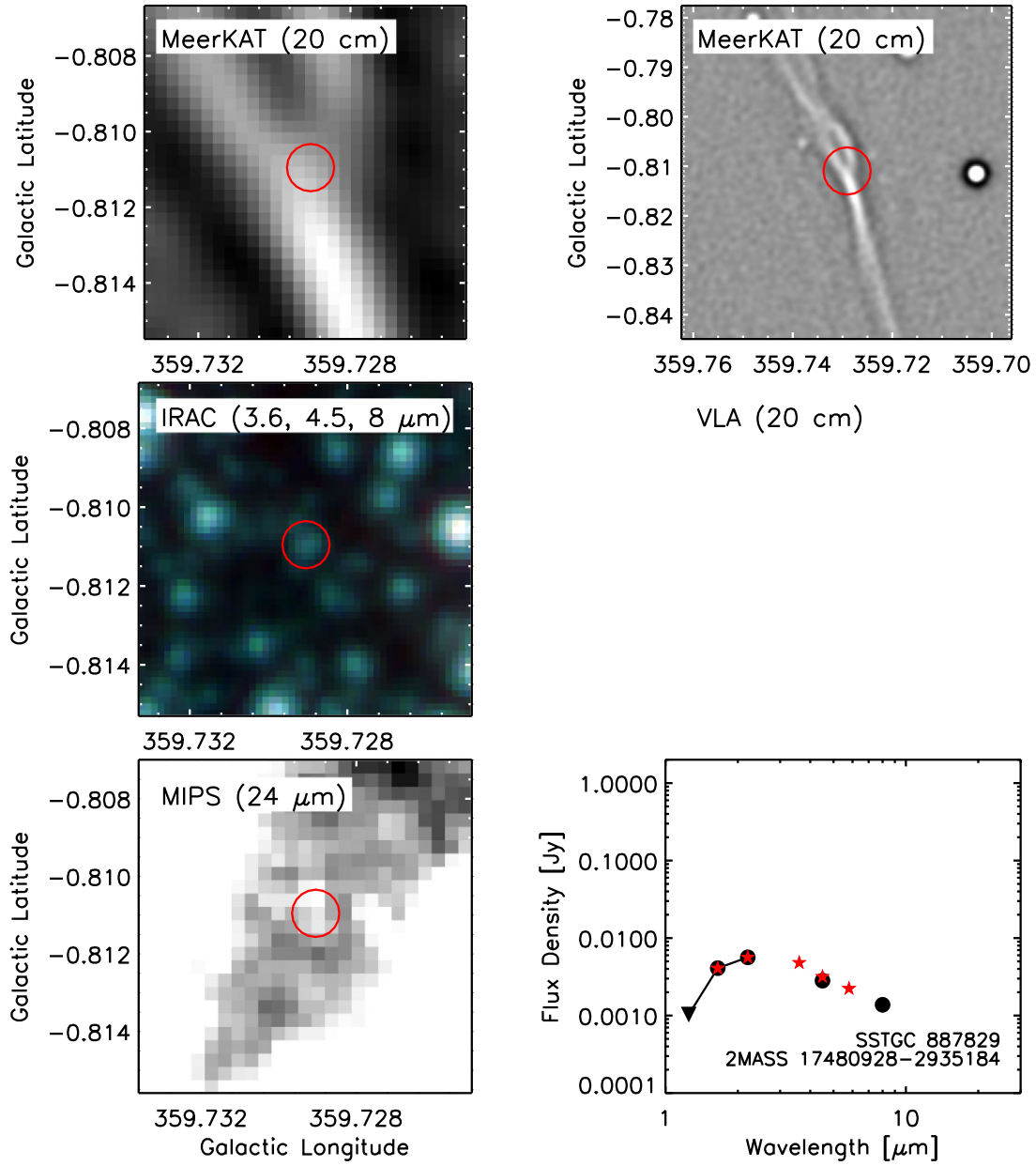


Figure 3. – (ee) Same as Fig. 3(a) except source 31 in Table 1.

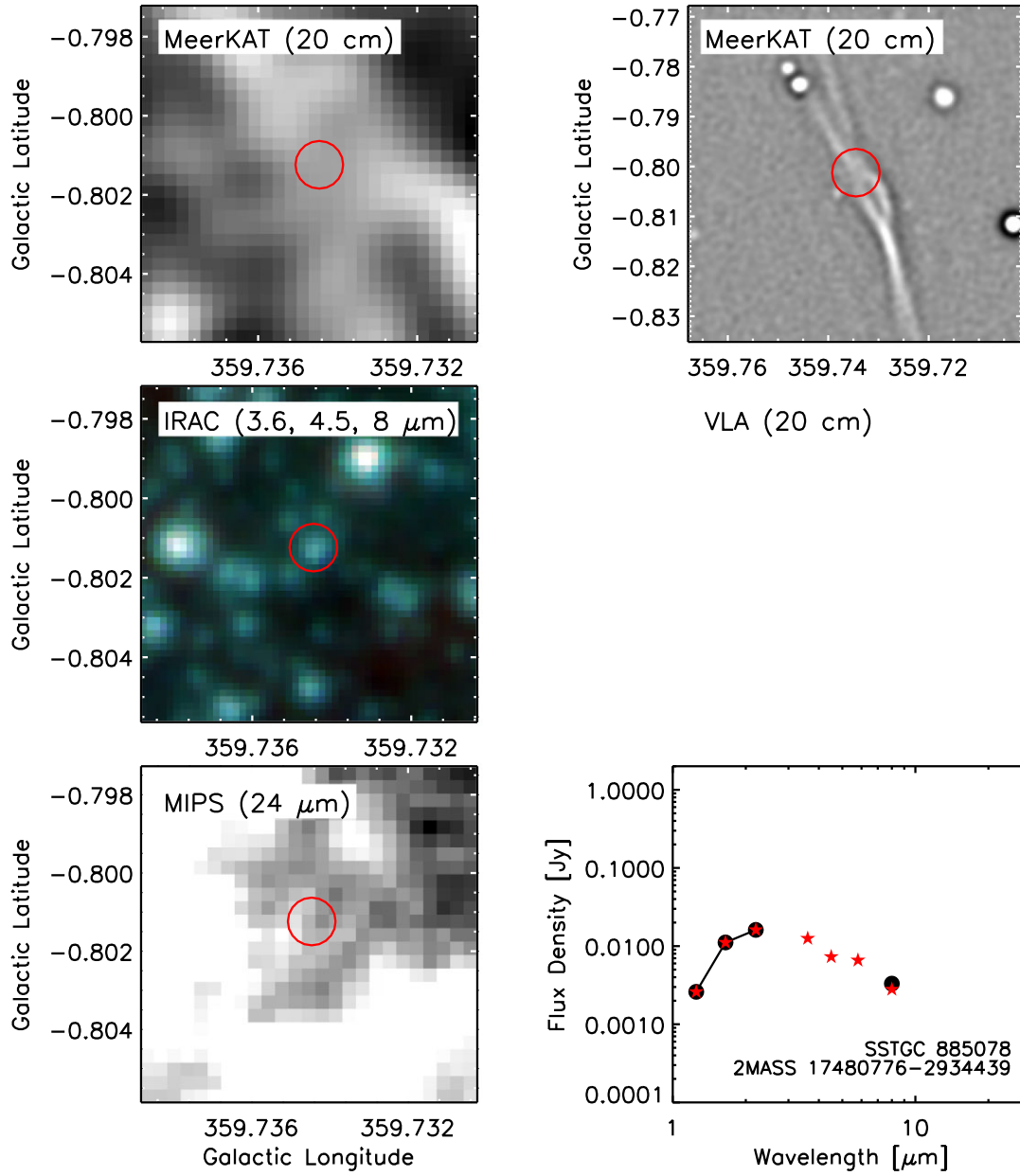


Figure 3. – (ff) Same as Fig. 3(a) except source 32 in Table 1.

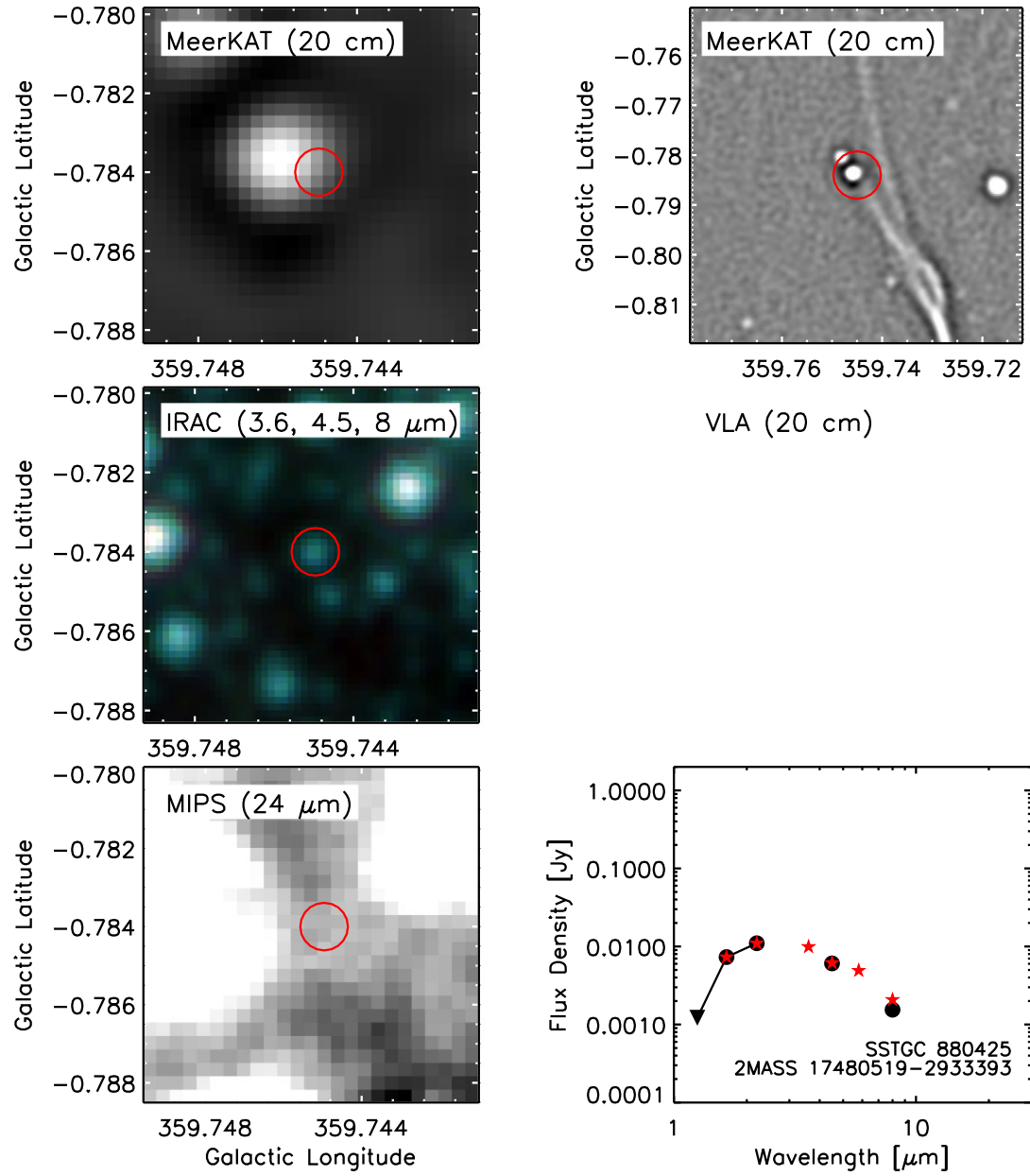


Figure 3. – (gg) Same as Fig. 3(a) except source 33 in Table 1.

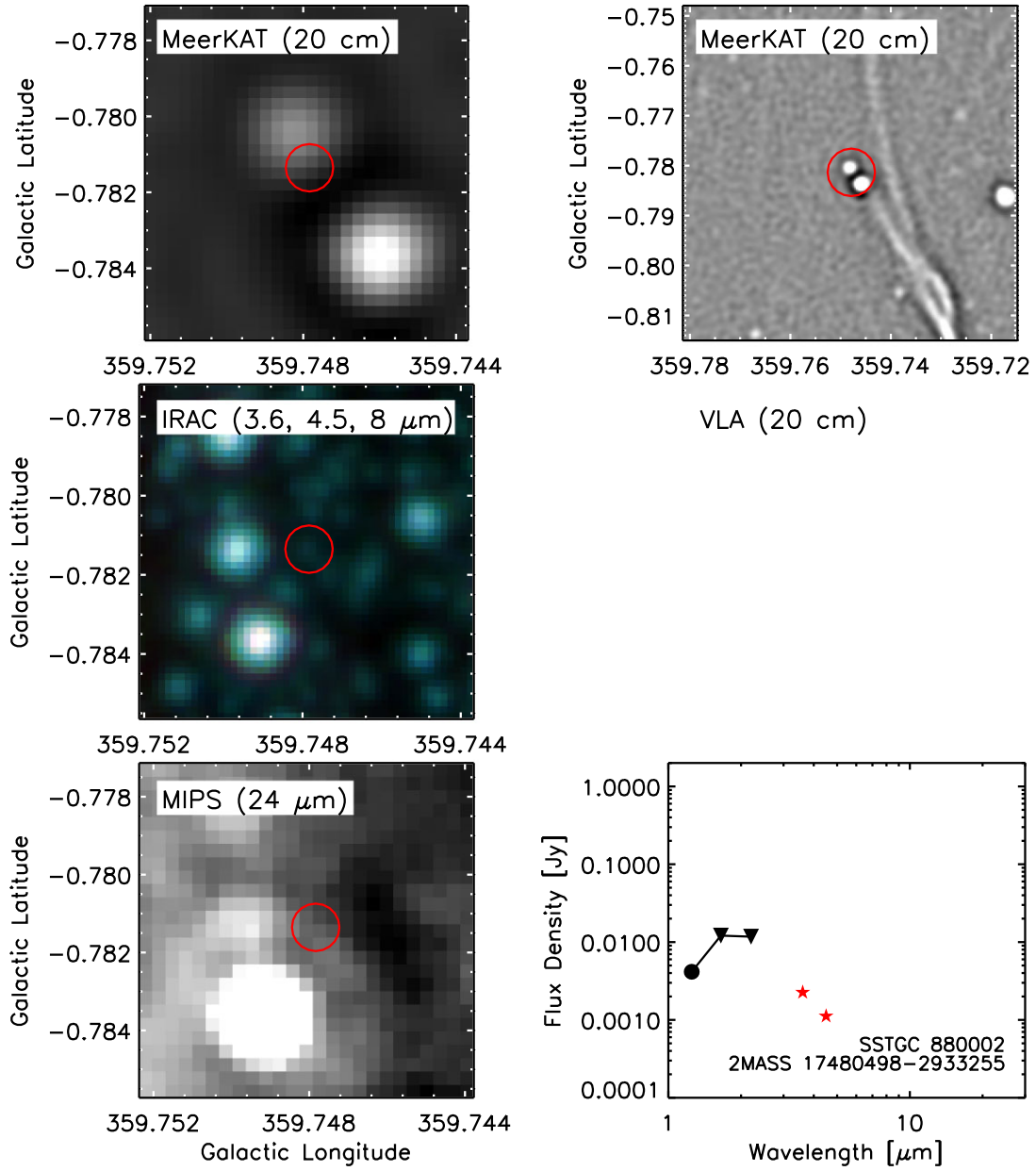


Figure 3. – (hh) Same as Fig. 3(a) except source 34 in Table 1.

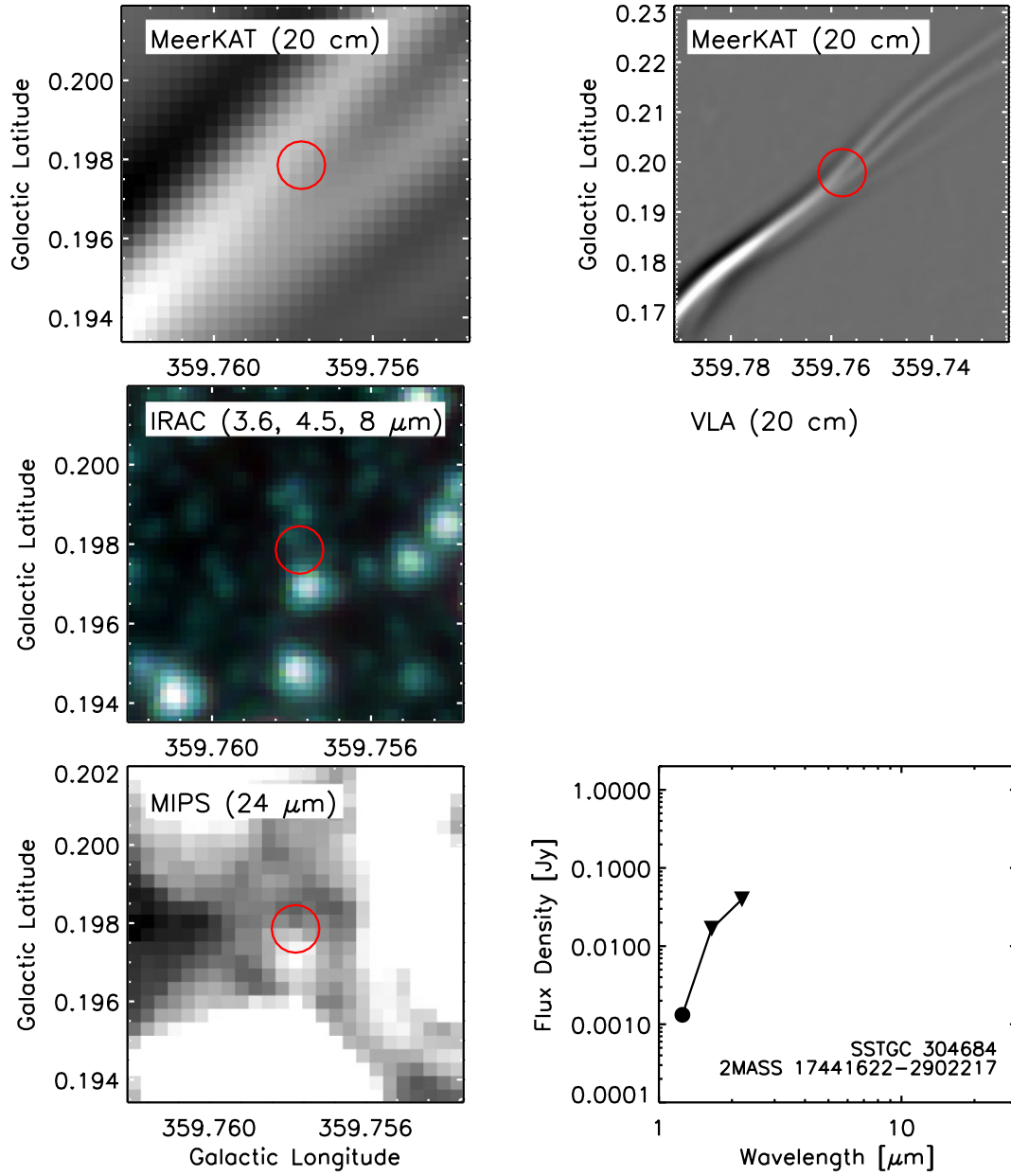


Figure 3. – (ii) Same as Fig. 3(a) except source 35 in Table 1.

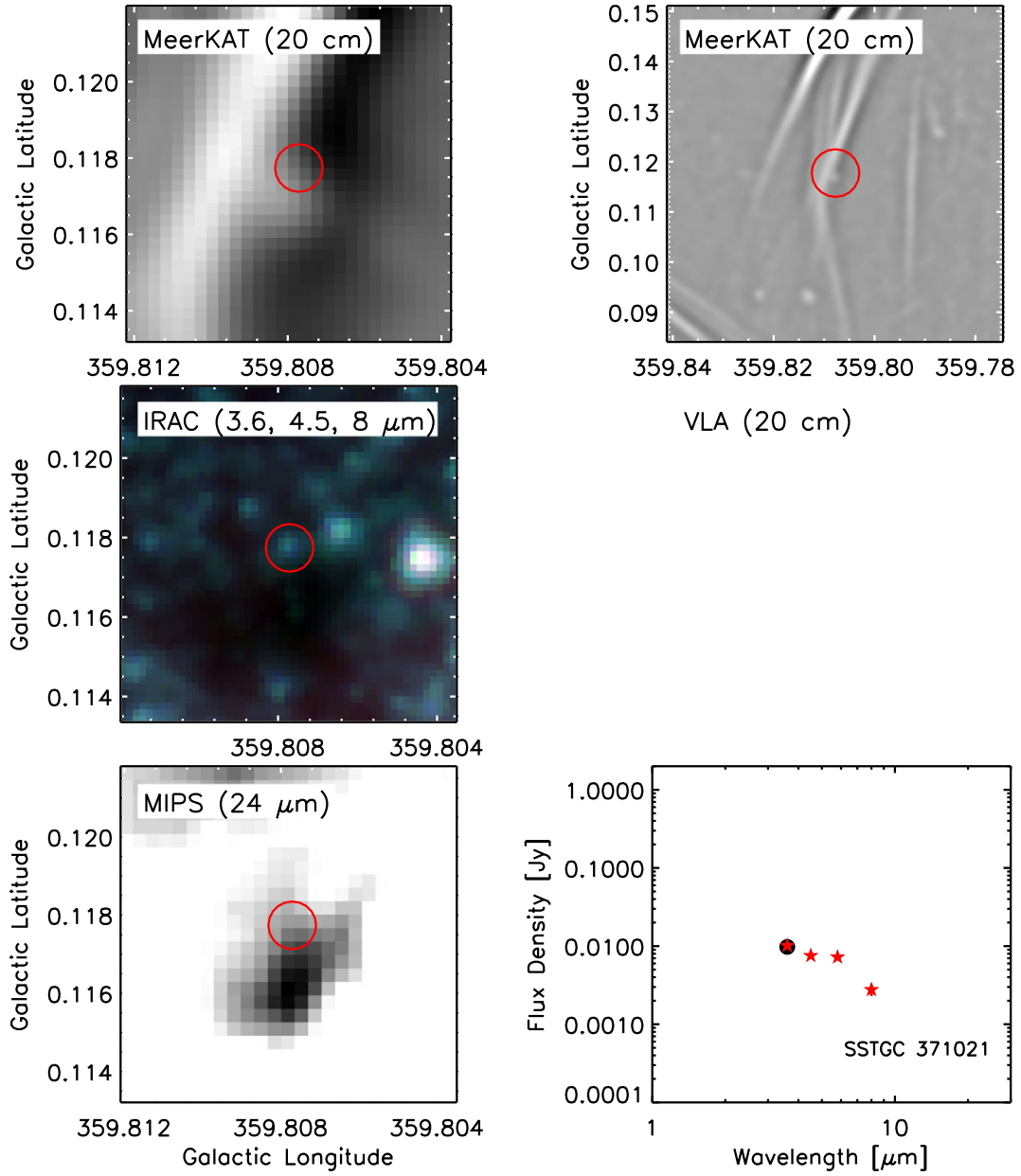


Figure 3. – (jj) Same as Fig. 3(a) except source 36 in Table 1.

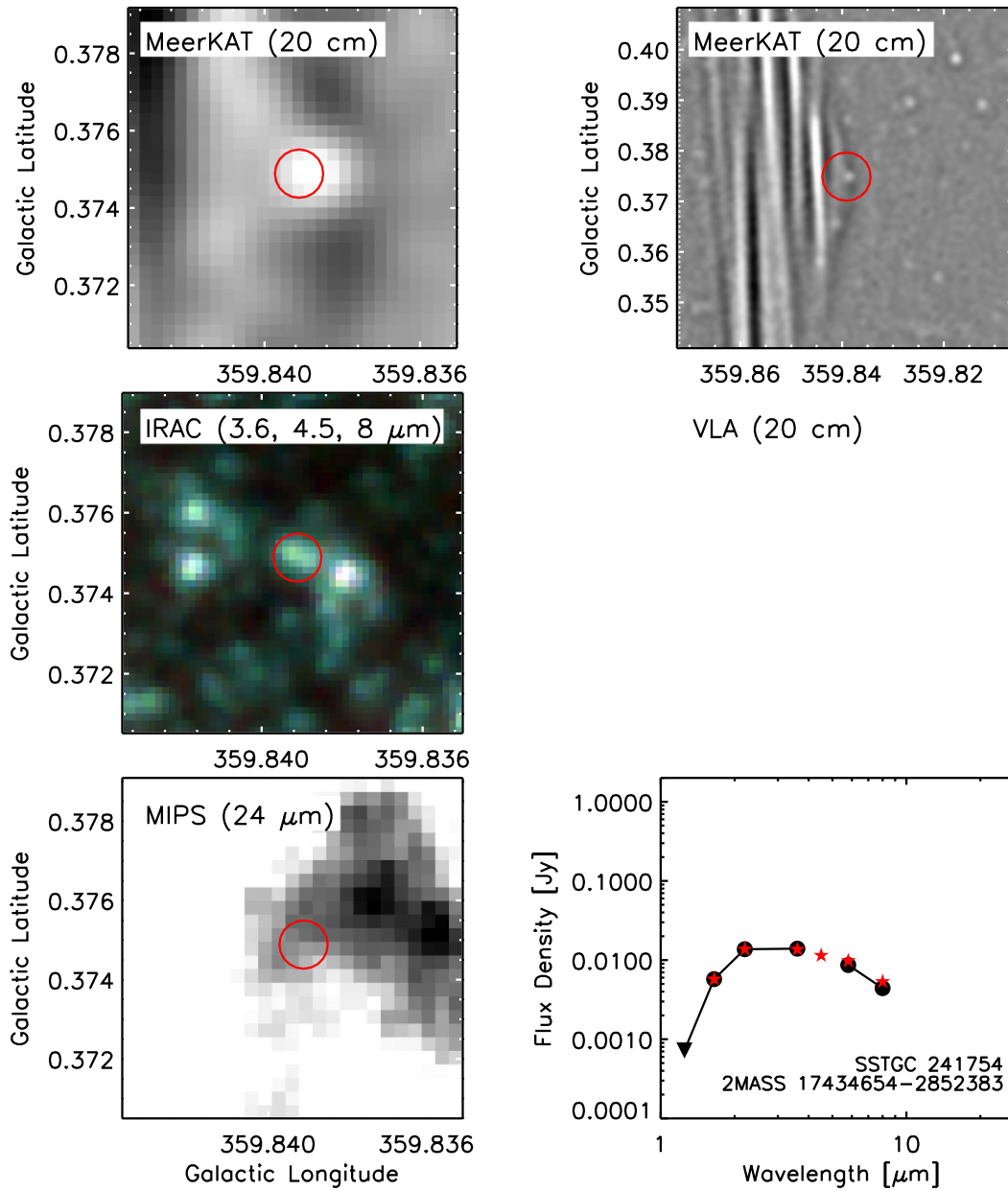


Figure 3. – (kk) Same as Fig. 3(a) except source 37 in Table 1.

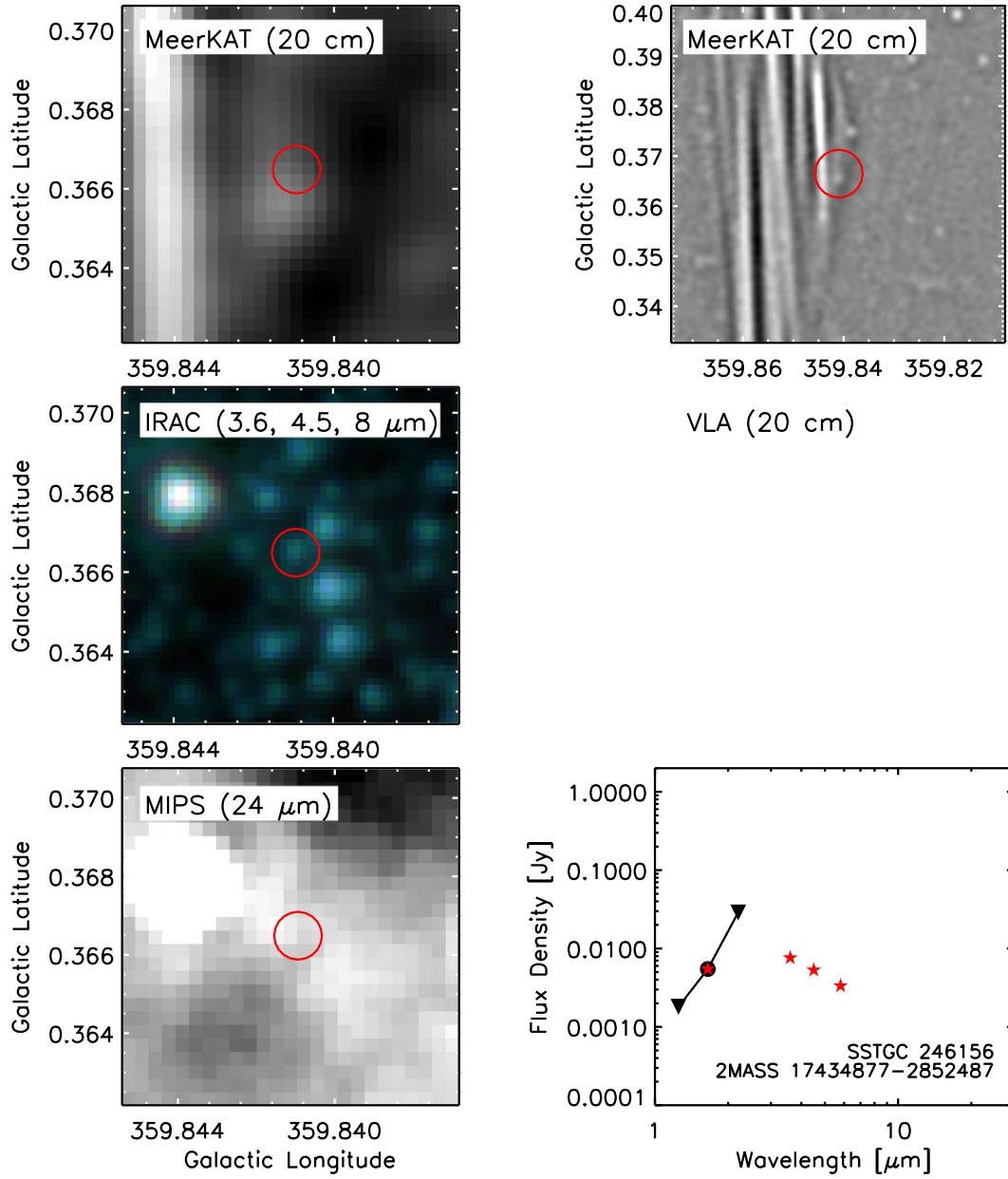


Figure 3. – (II) Same as Fig. 3(a) except source 38 in Table 1.

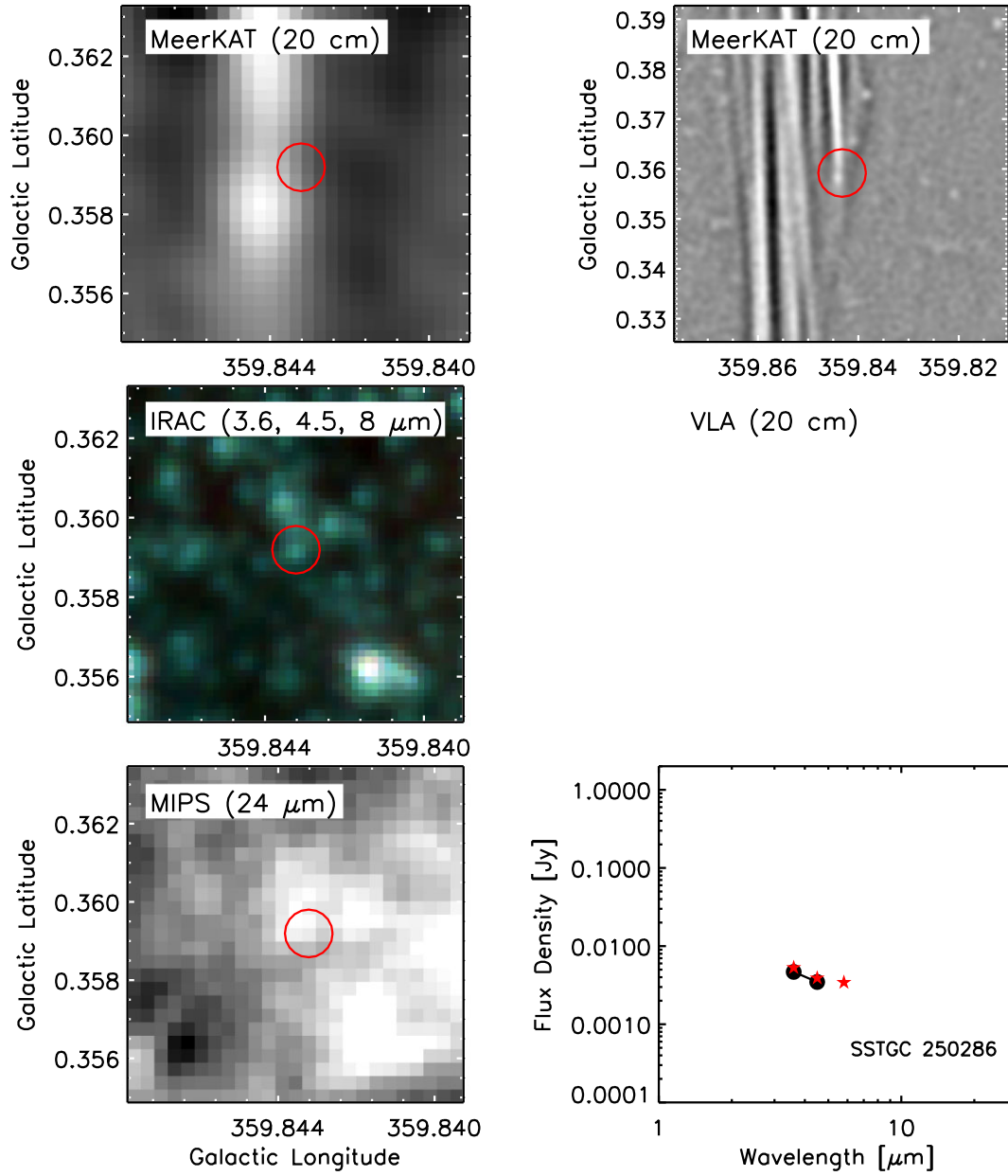


Figure 3. – (mm) Same as Fig. 3(a) except source 39 in Table 1.

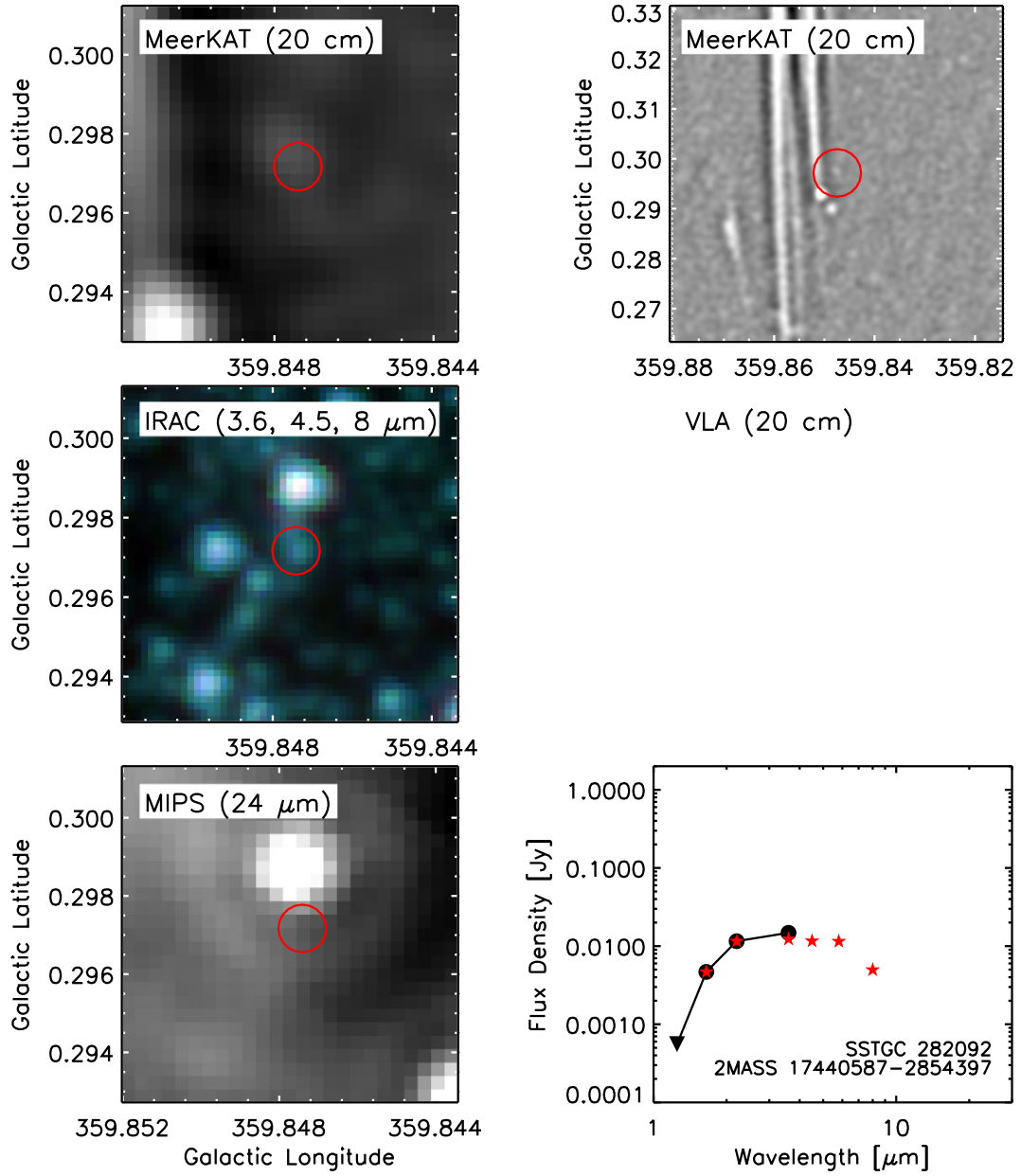


Figure 3. – (nn) Same as Fig. 3(a) except source 40 in Table 1.

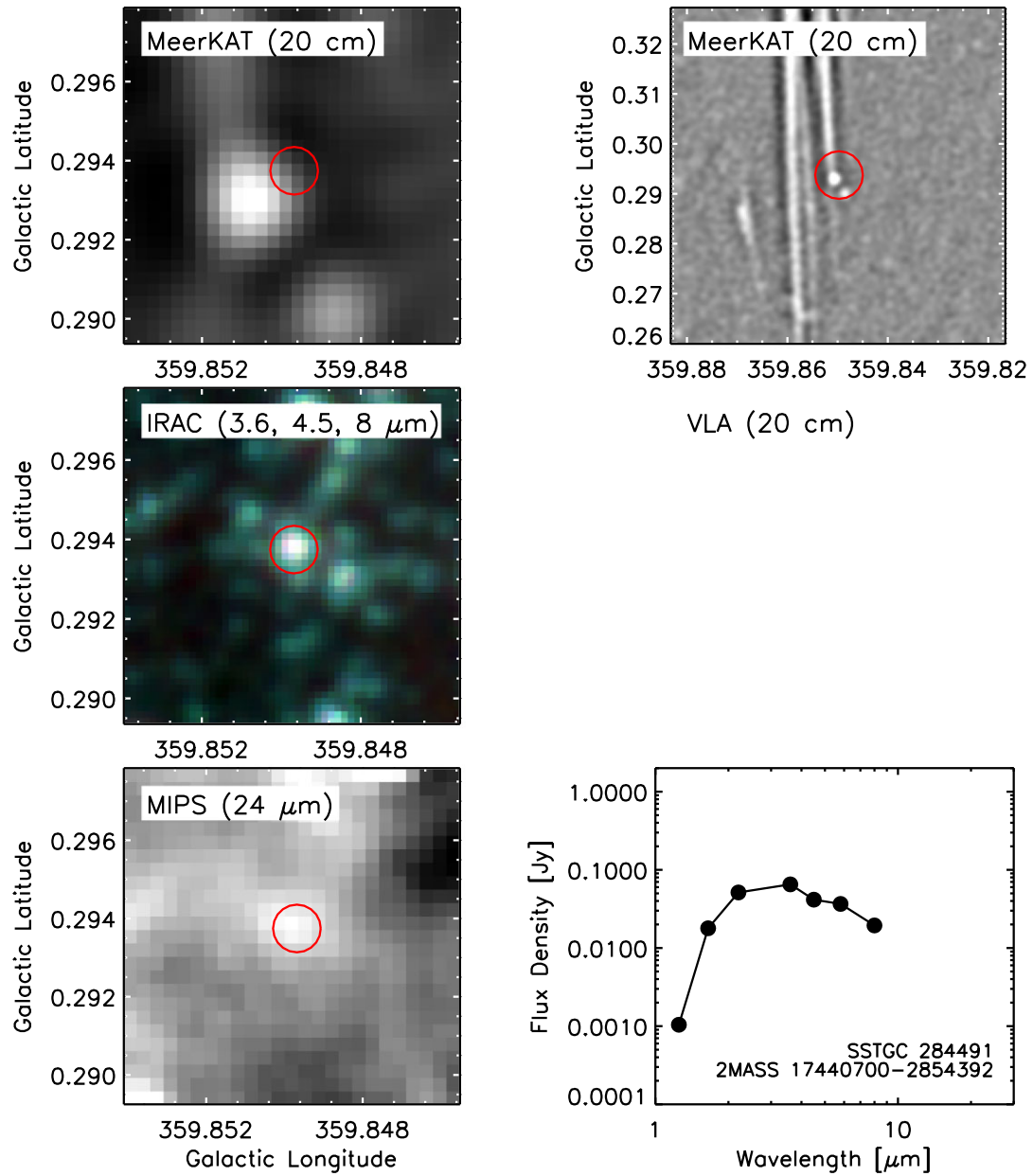


Figure 3. – (oo) Same as Fig. 3(a) except source 41 in Table 1.

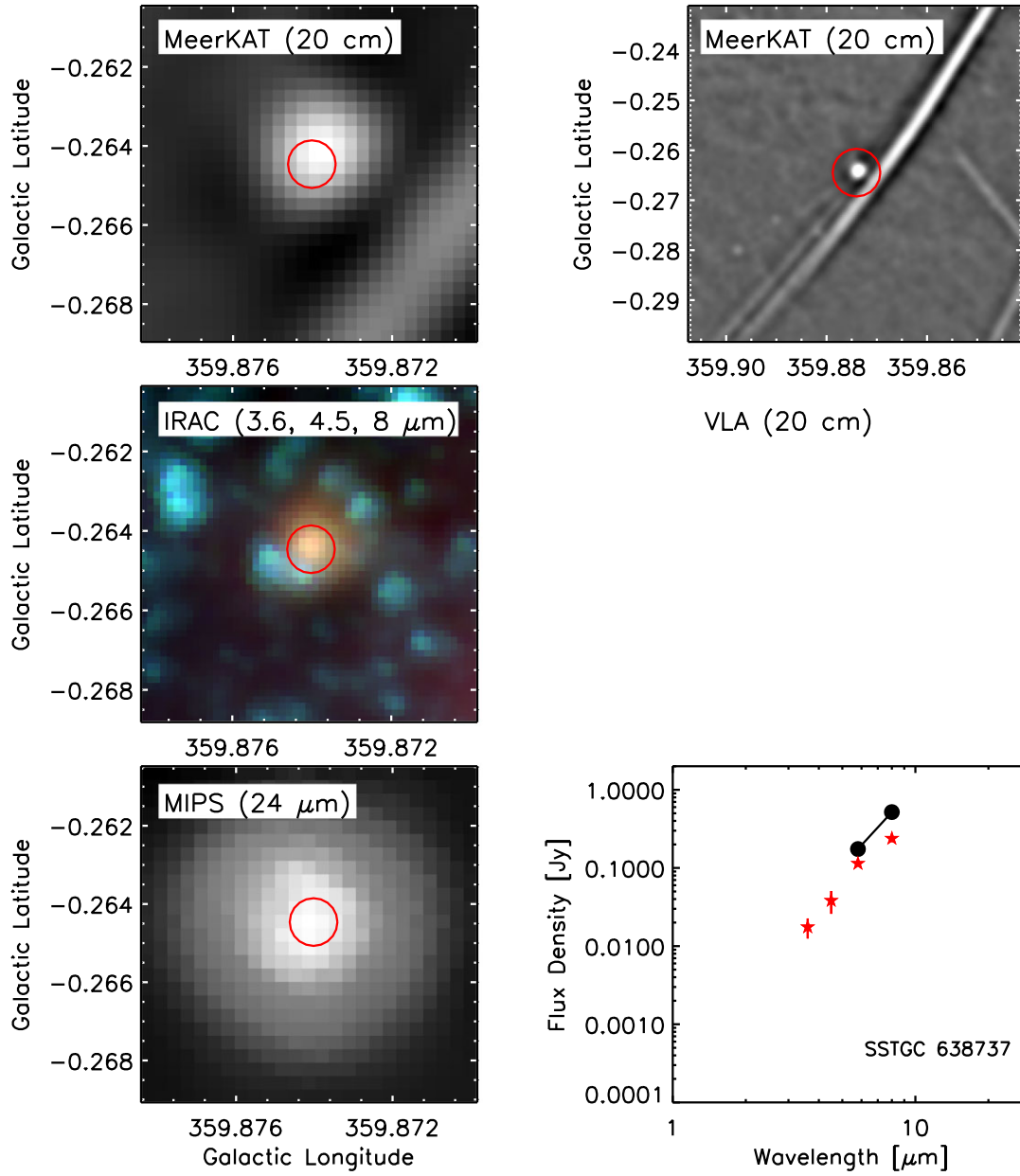


Figure 3. – (pp) Same as Fig. 3(a) except source 42 in Table 1.

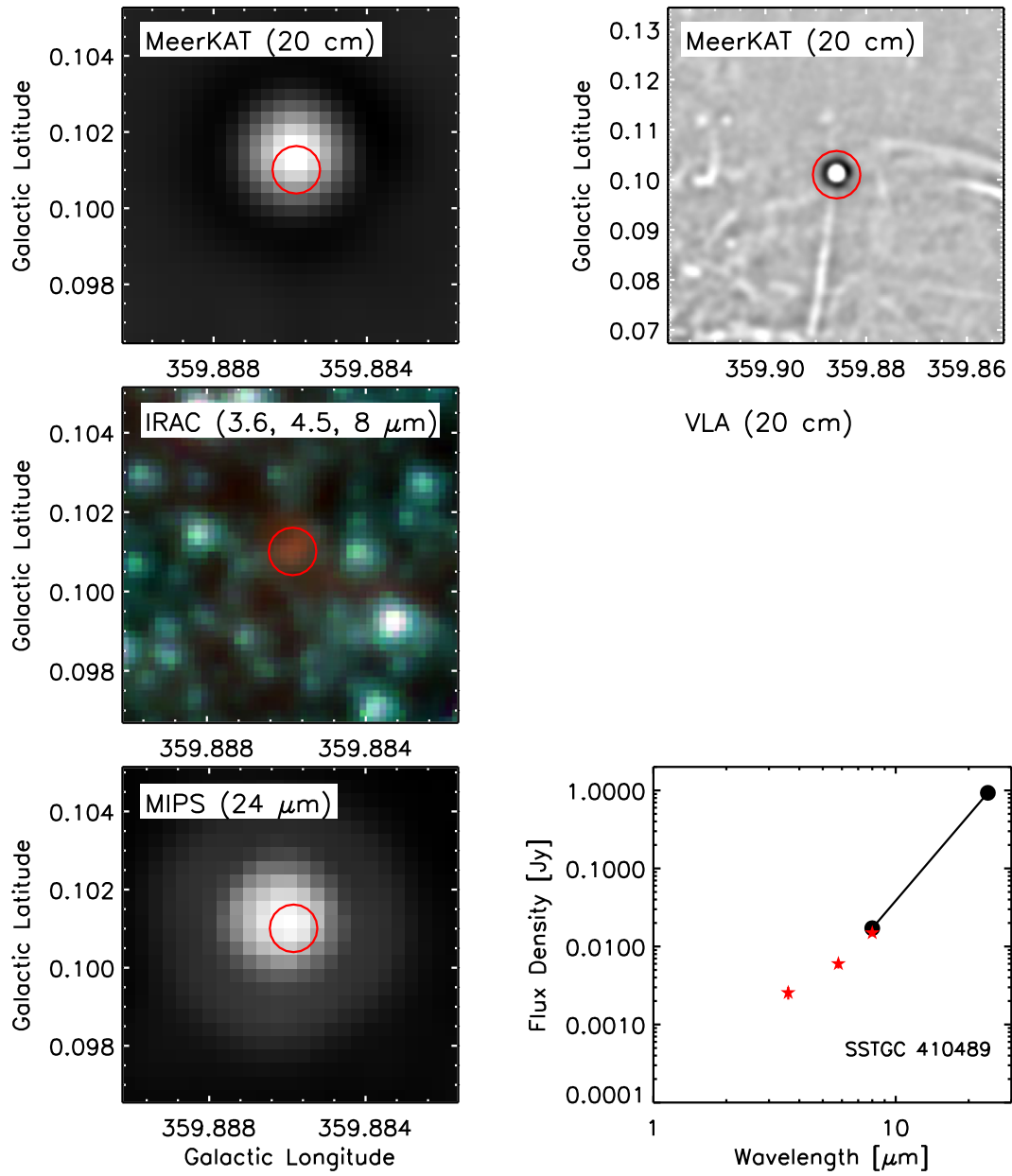


Figure 3. – (qq) Same as Fig. 3(a) except source 43 in Table 1.

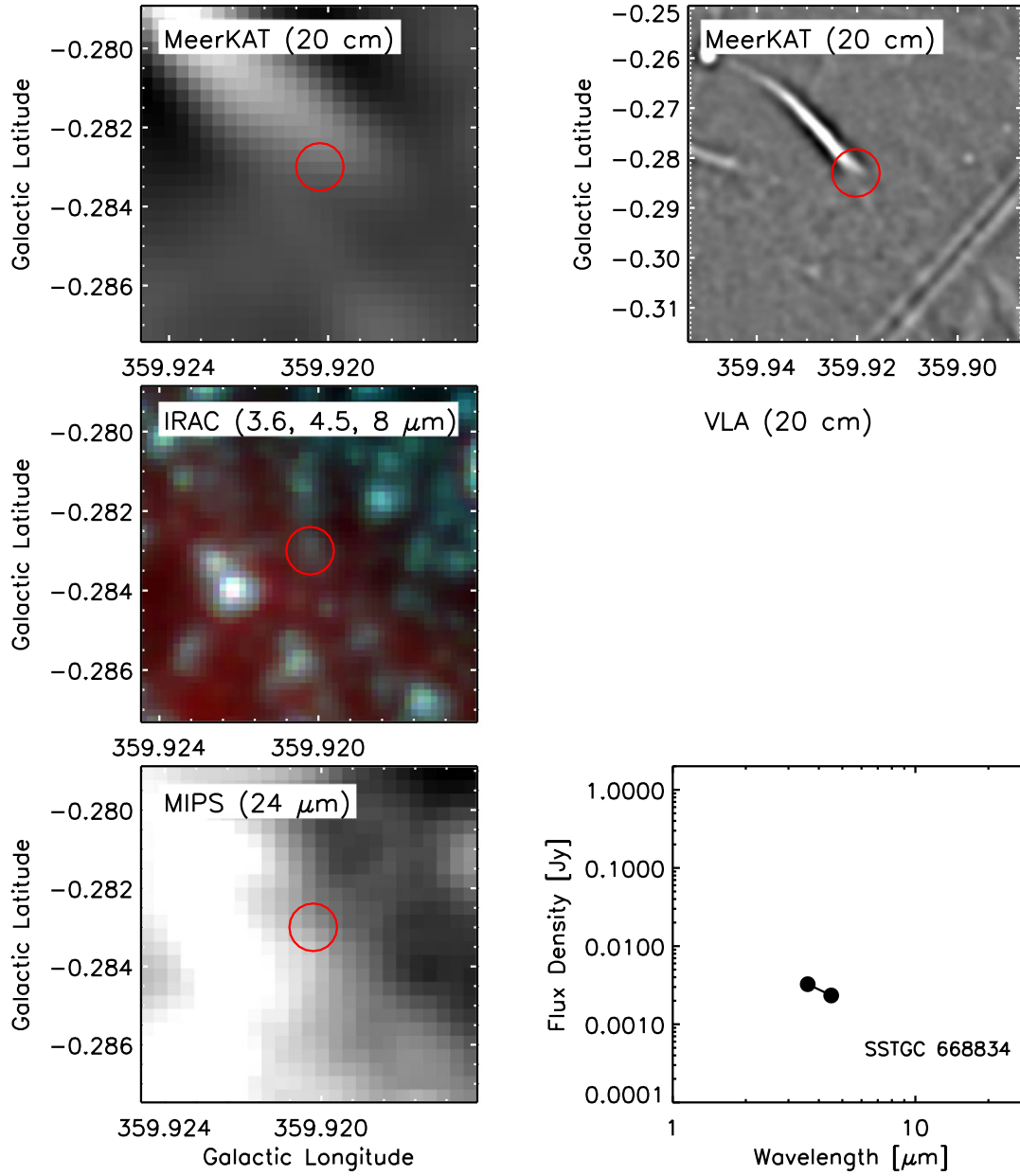


Figure 3. – (rr) Same as Fig. 3(a) except source 44 in Table 1.

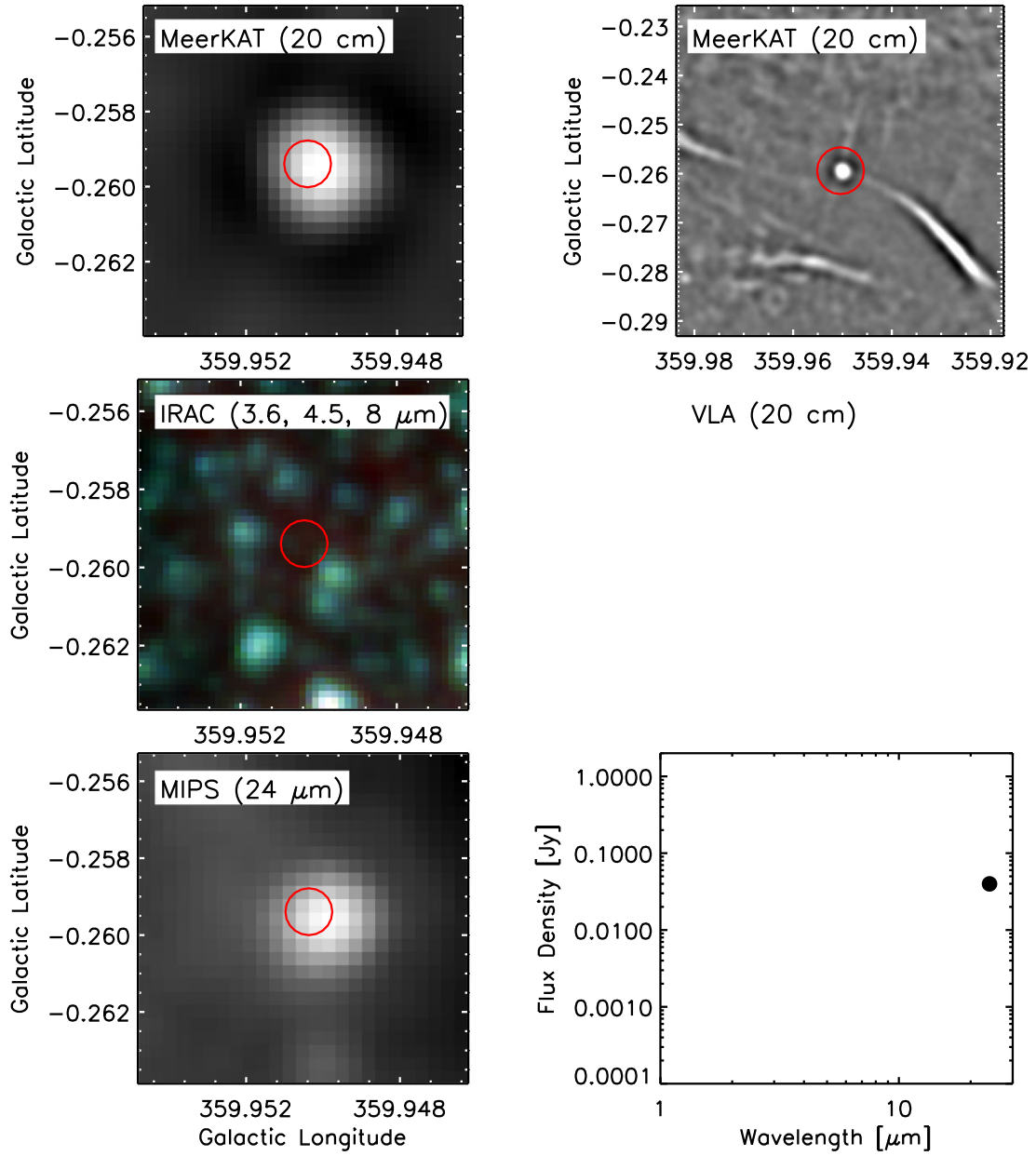


Figure 3. – (ss) Same as Fig. 3(a) except source 45 in Table 1.

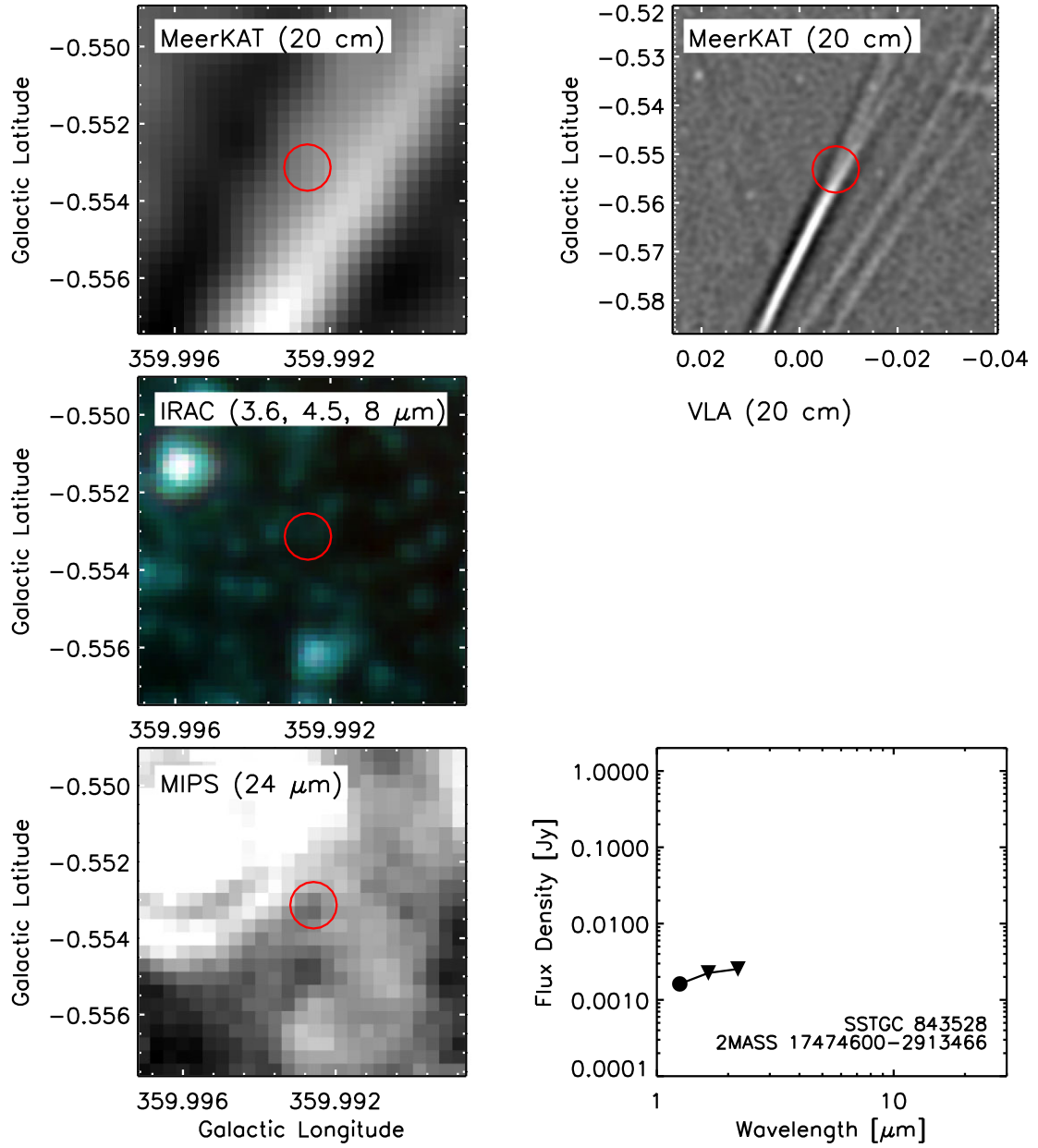


Figure 3. – (tt) Same as Fig. 3(a) except source 46 in Table 1.

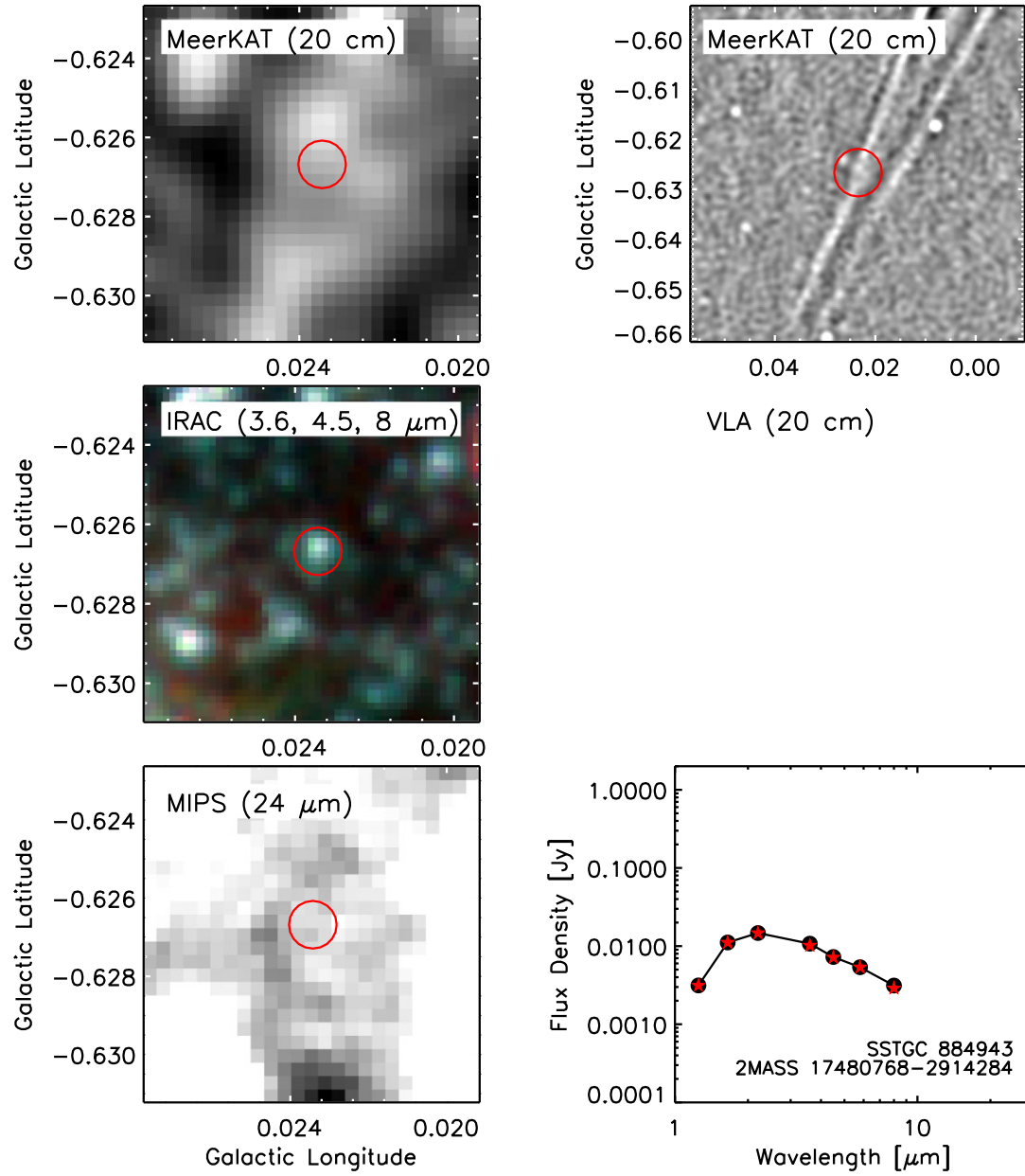


Figure 3. – (uu) Same as Fig. 3(a) except source 47 in Table 1.

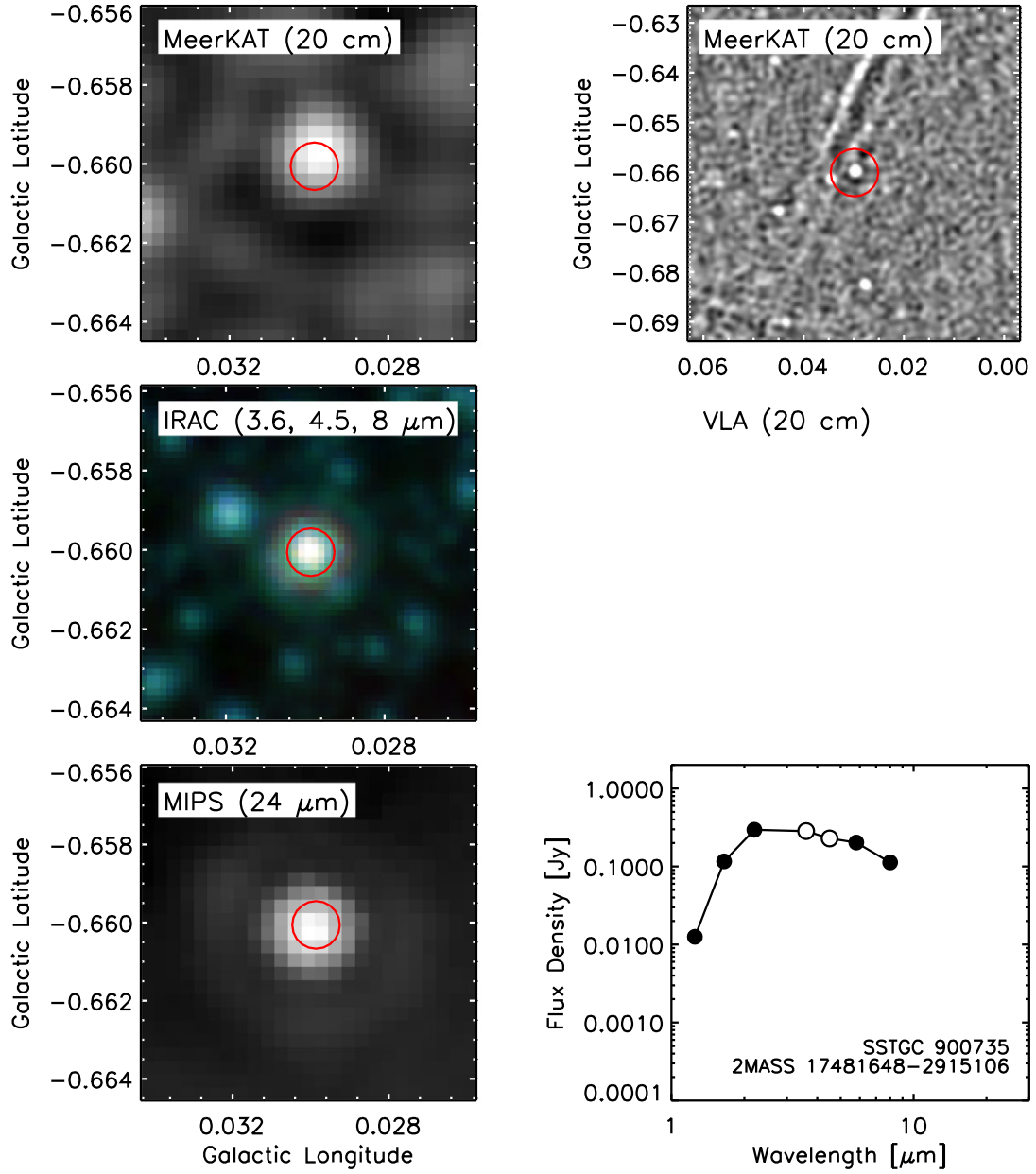


Figure 3. – (vv) Same as Fig. 3(a) except source 48 in Table 1. Open circles indicate potentially saturated IRAC measurements.

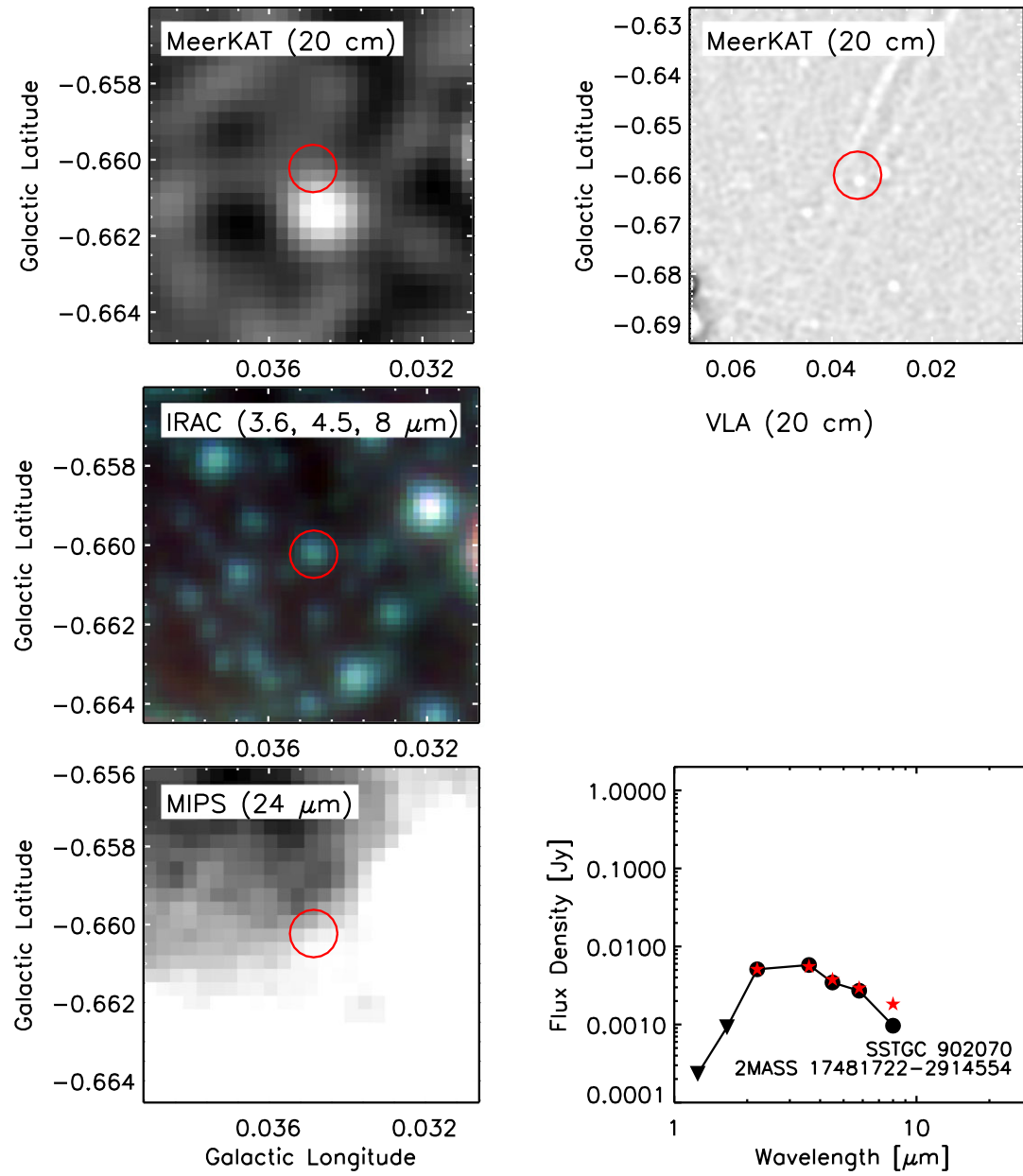


Figure 3. – (ww) Same as Fig. 3(a) except source 49 in Table 1.

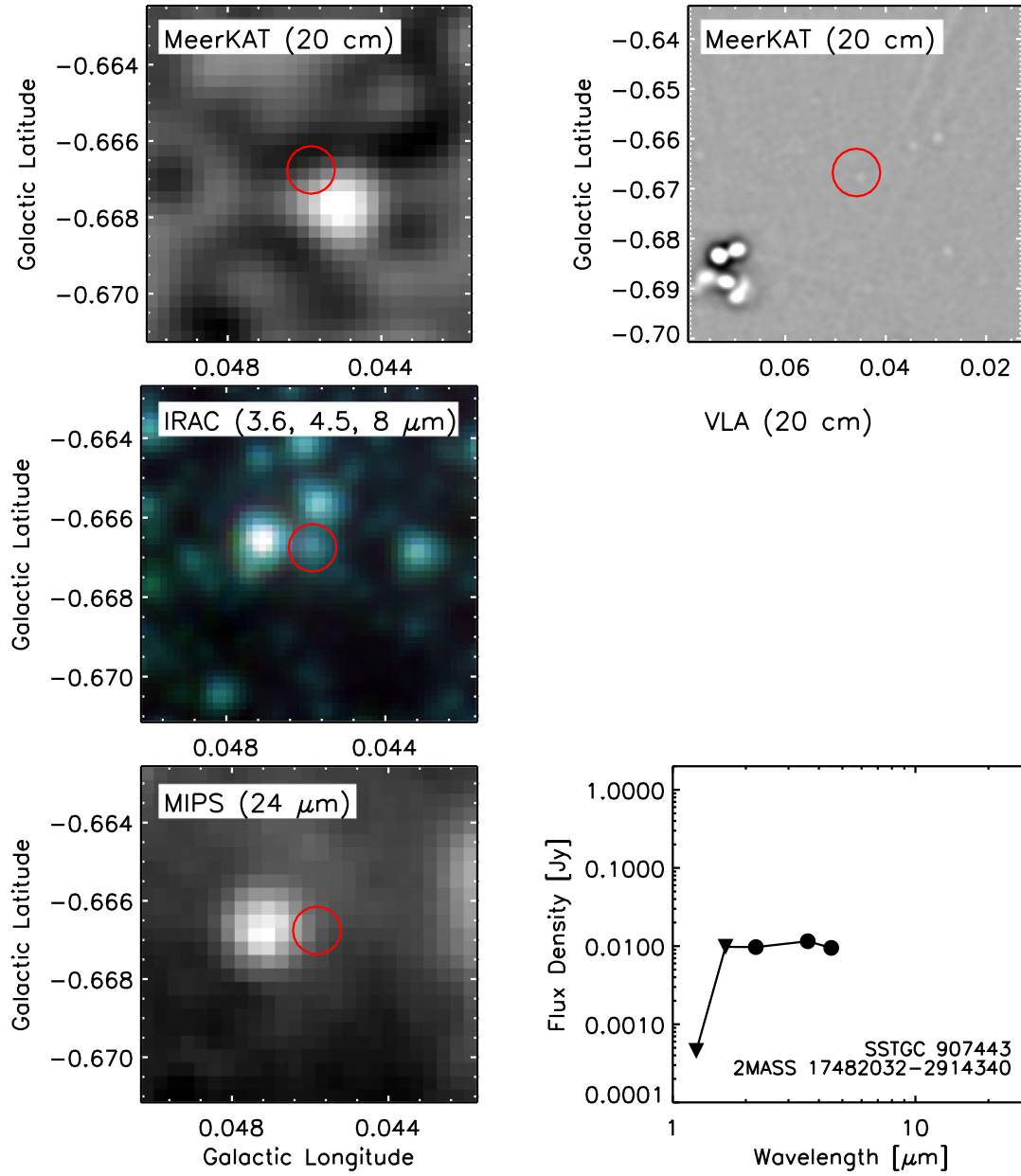


Figure 3. – (xx) Same as Fig. 3(a) except source 50 in Table 1.

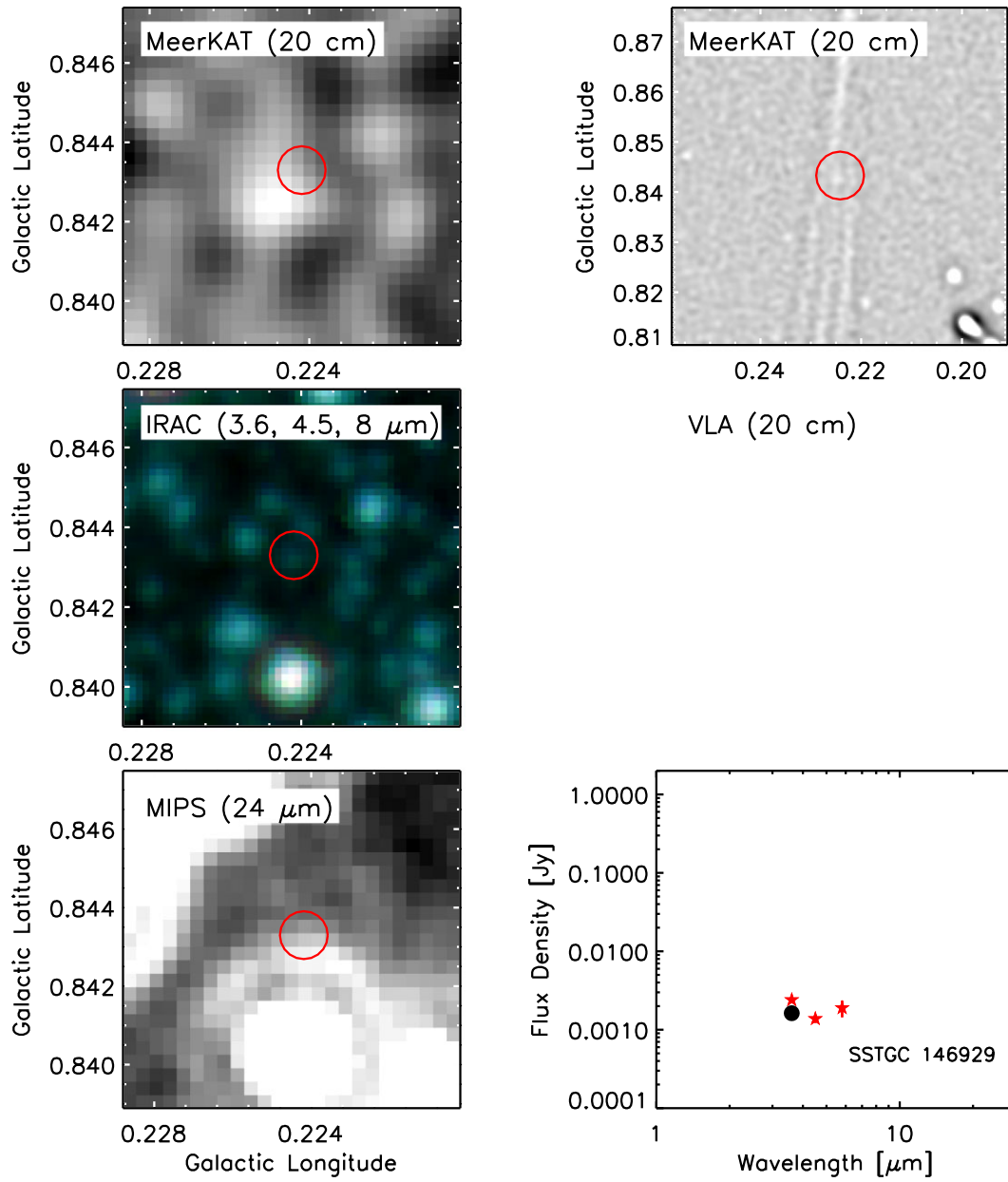


Figure 3. – (yy) Same as Fig. 3(a) except source 51 in Table 1.

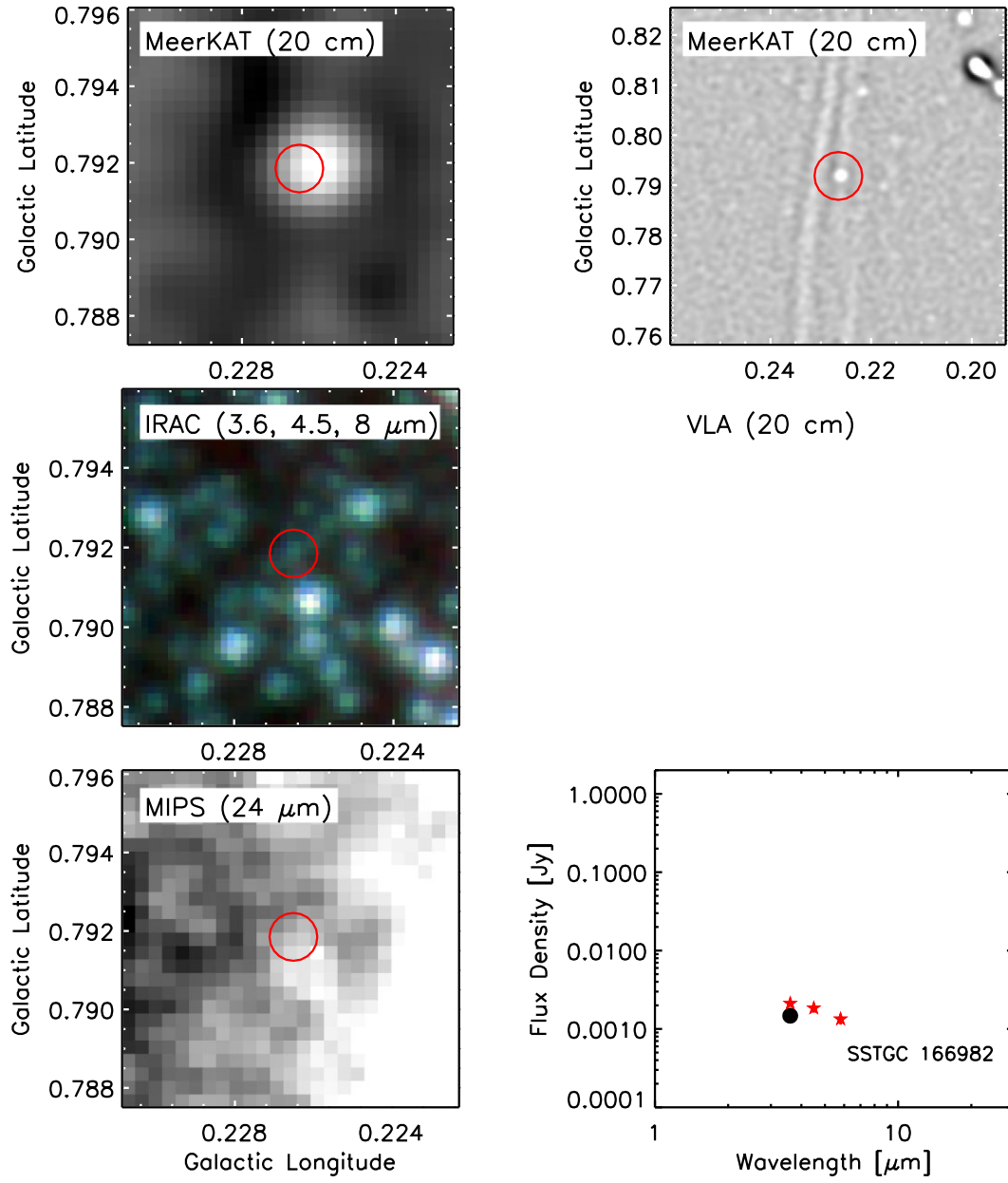


Figure 3. – (zz) Same as Fig. 3(a) except source 52 in Table 1.

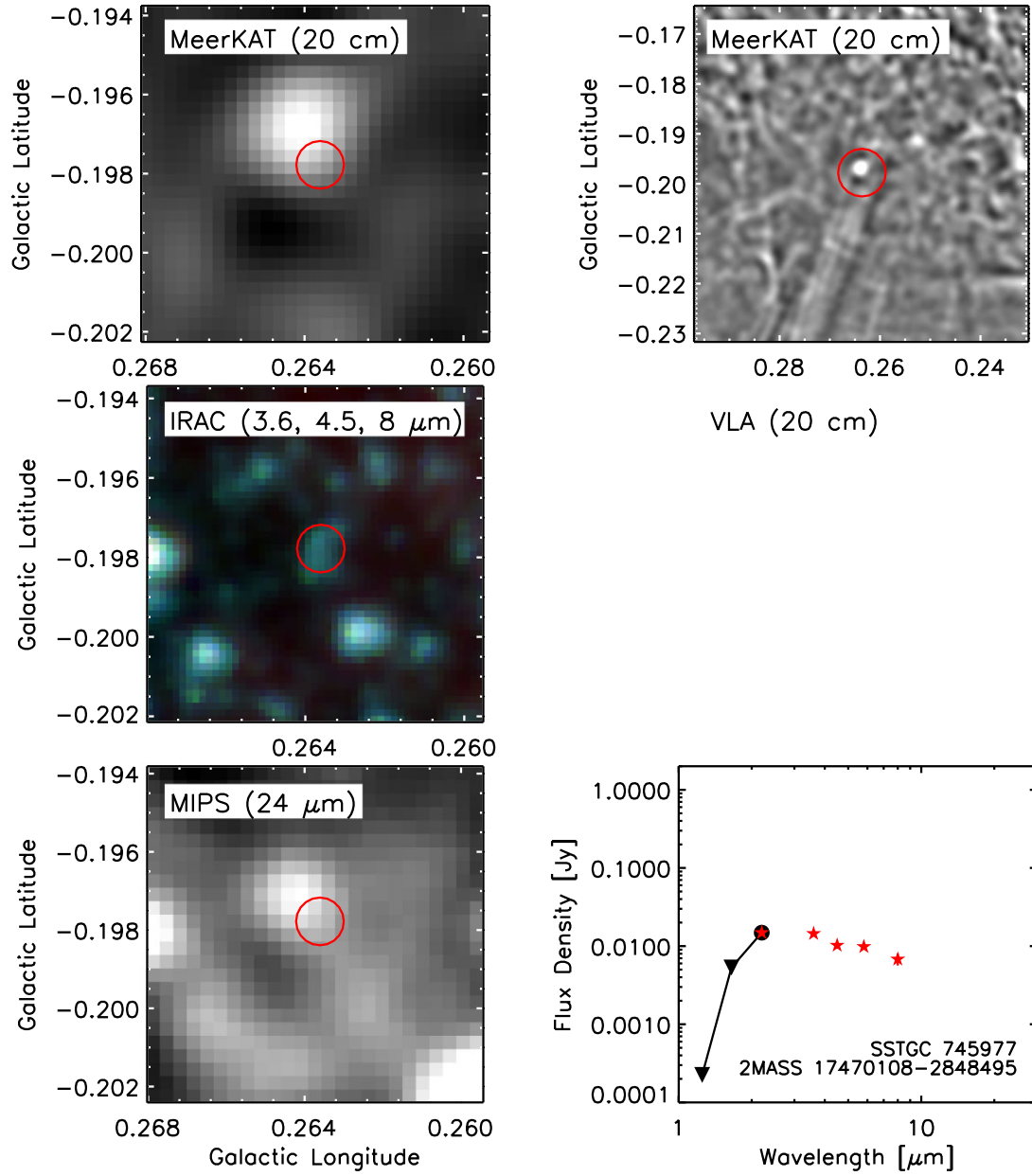


Figure 3. – (aaa) Same as Fig. 3(a) except source 53 in Table 1.

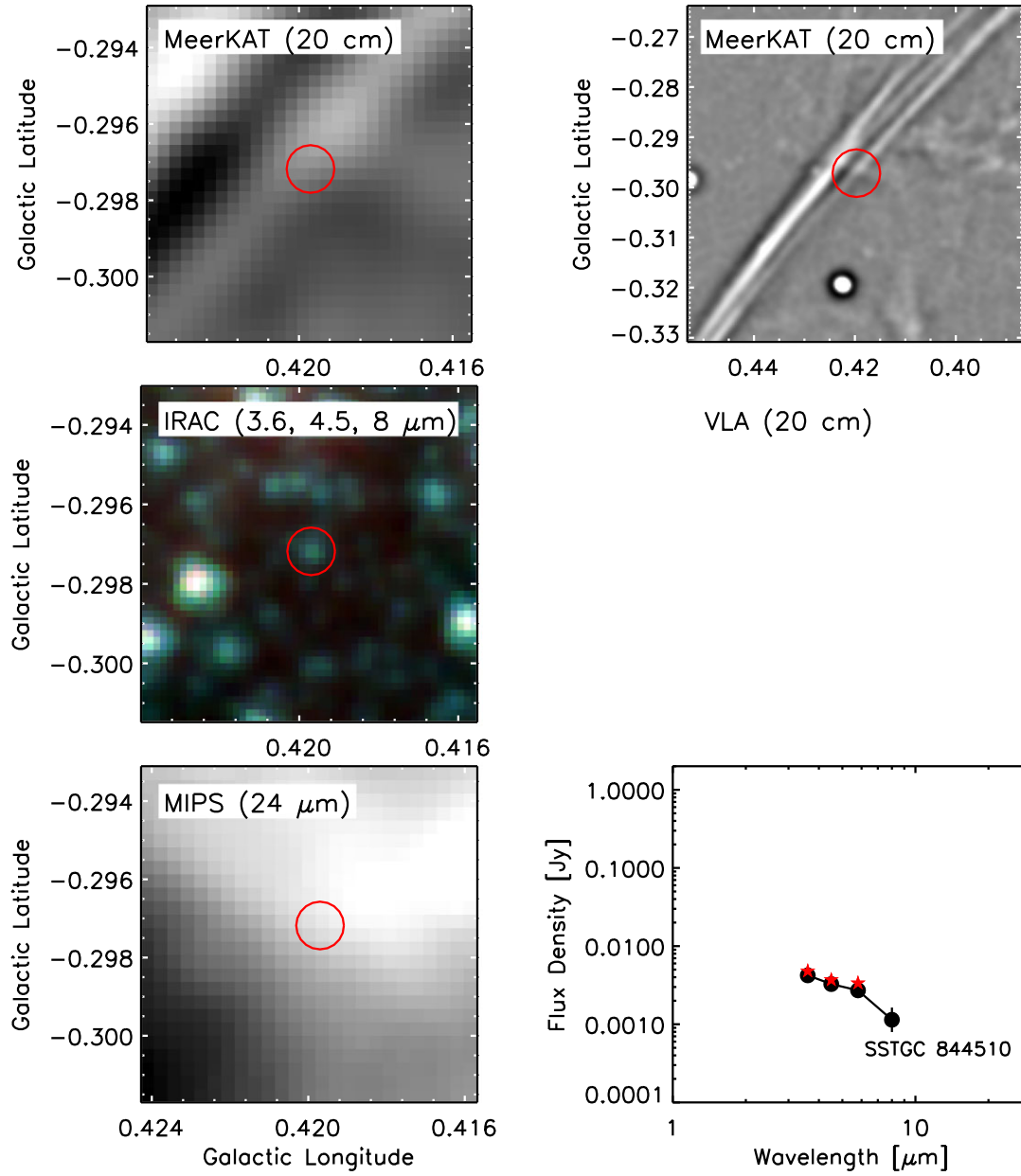


Figure 3. – (bbb) Same as Fig. 3(a) except source 54 in Table 1.

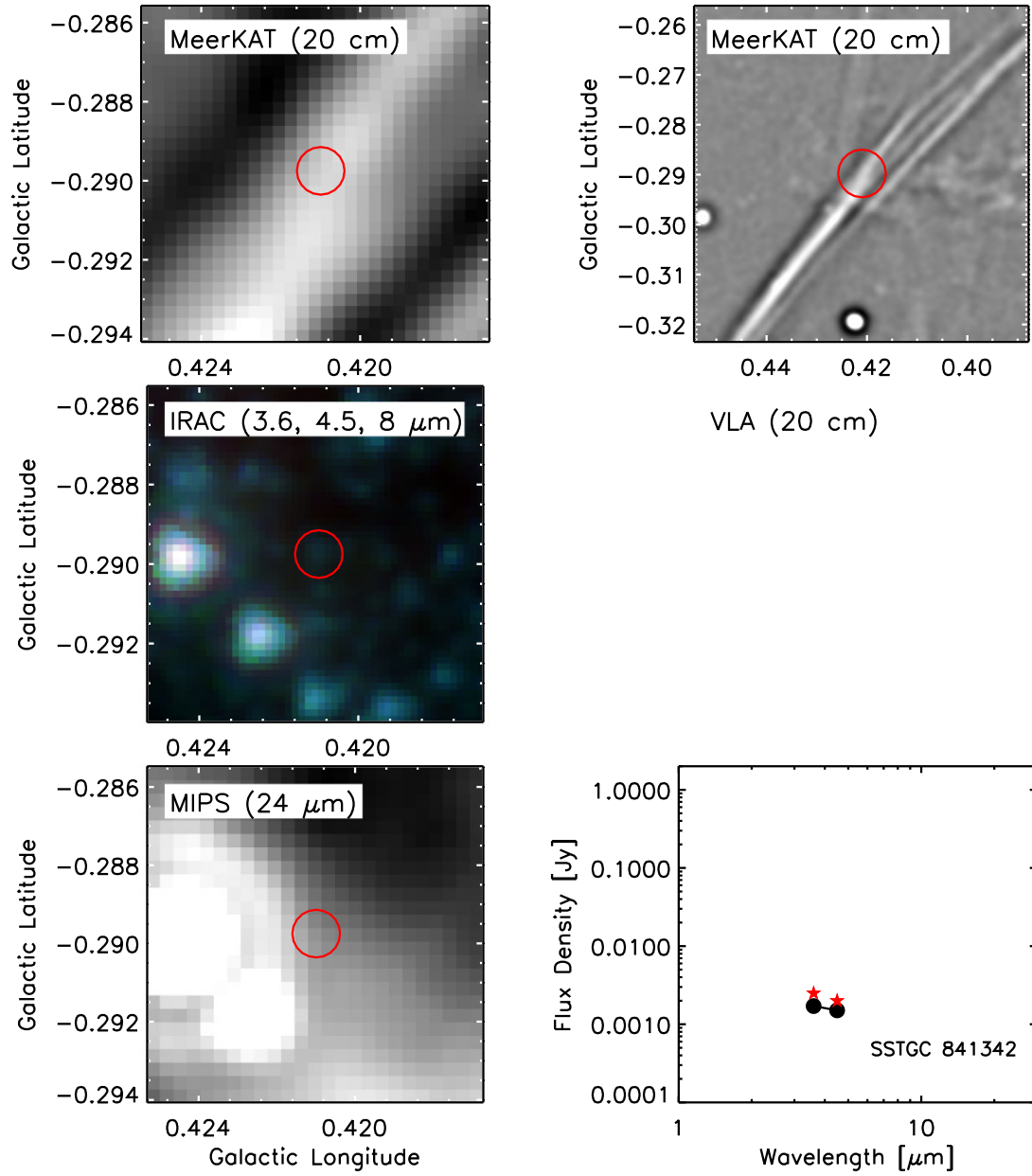


Figure 3. – (ccc) Same as Fig. 3(a) except source 55 in Table 1.

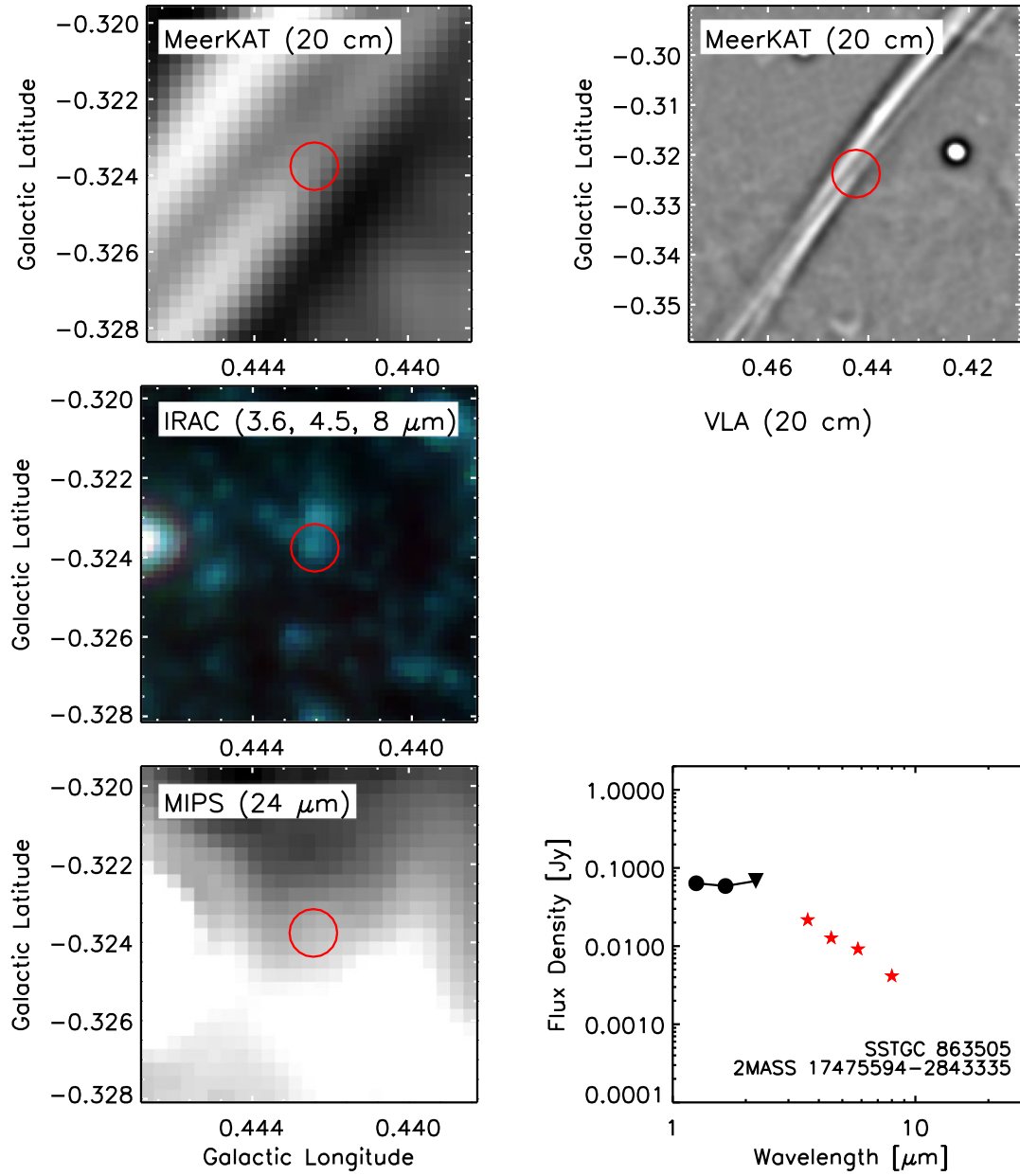


Figure 3. – (ddd) Same as Fig. 3(a) except source 56 in Table 1.

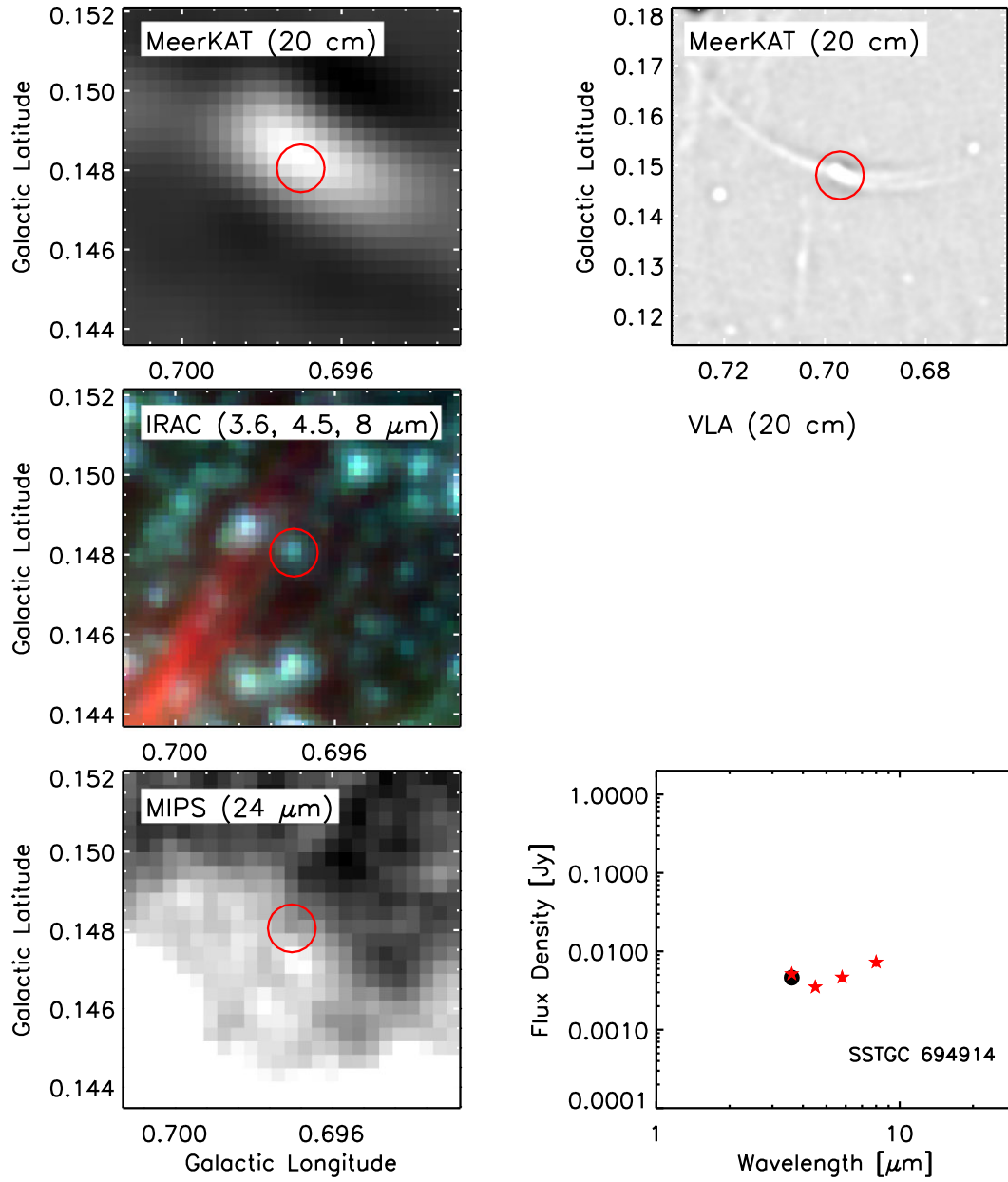


Figure 3. – (eee) Same as Fig. 3(a) except source 57 in Table 1.

ACKNOWLEDGEMENTS

Work by RGA was supported by NASA under award number 80GSFC21M0002. FYZ is partially supported by the grant AST-0807400 from the National Science Foundation. The MeerKAT telescope is operated by the South African Radio Astronomy Observatory, which is a facility of the National Research Foundation, an agency of the Department of Science and Innovation. The National Radio Astronomy Observatory is a facility of the National Science Foundation operated under cooperative agreement by Associated Universities, Inc.

DATA AVAILABILITY

All the data including VLA and MeerKAT that we used here are available online and are not proprietary. We have reduced and calibrated these data and they are available if requested.

REFERENCES

- Benjamin R. A. et al., 2003, *Publ. Astron. Soc. Aust.*, 115, 953
 Bicknell G. V., Li J., 2001, *ApJ*, 548, L69
 Crocker R. M., Aharonian F., 2011, *Phys. Rev. Lett.*, 106, 101102
 Engelke C. W., Price S. D., Kraemer K. E., 2006, *AJ*, 132, 1445
 Everett J. E., Zweibel E. G., Benjamin R. A., McCammon D., Rocks L., Gallagher J. S., 2008, *ApJ*, 674, 258
 Everett J. E., Schiller Q. G., Zweibel E. G., 2010, *ApJ*, 711, 13
 Geballe T. R., McCall B. J., Hinkle K. H., Oka T., 1999, *ApJ*, 510, 251
 Goto M., Geballe T. R., Indriolo N., Yusef-Zadeh F., Usuda T., Henning T., Oka T., 2014, *ApJ*, 786, 96
 Heywood I. et al., 2019, *Nature*, 573, 235
 Heywood I. et al., 2022, *ApJ*, 925, 165
 Hinz J. L., Rieke G. H., Yusef-Zadeh F., Hewitt J., Balog Z., Block M., 2009, *ApJS*, 181, 227
 Indriolo N., McCall B. J., 2012, *ApJ*, 745, 91
 Le Petit F. et al., 2016, *A&A*, 585, A105
 Oka T., Geballe T. R., Goto M., Usuda T., McCall B. J., 2005, *ApJ*, 632, 882
 Oka T., Geballe T. R., Goto M., Usuda T., McCall B. J., 2019, *ApJ*, 883, 54
 Ramirez S. V., Arendt R. G., Sellgren K., Stolovy S. R., Cotera A., Smith H. A., Yusef-Zadeh F., 2008, *ApJS*, 175, 147
 Reiter M. et al., 2015, *MNRAS*, 447, 3909
 Ruszkowski M., Yang H.-Y. K., Zweibel E., 2017, *ApJ*, 834, 208
 Shore S. N., LaRosa T. N., 1999, *ApJ*, 521, 587
 Su M., Slatyer T. R., Finkbeiner D. P., 2010, *ApJ*, 724, 1044
 Thomas T., Pfrommer C., Enßlin T., 2020, *ApJ*, 890, L18
 Yang H.-Y. K., Ruszkowski M., Zweibel E., 2013, *MNRAS*, 436, 2734
 Yusef-Zadeh F., Wardle M., 2019, *MNRAS*, 490, L1
 Yusef-Zadeh F., Arendt R. G., Wardle M., Heywood I., Cotton W., Camilo F., 2022, *ApJ*, 925, L18
 Yusef-Zadeh F., Arendt R. G., Wardle M., Boldyrev S., Heywood I., Cotton W., Camilo F., 2022, *MNRAS*, 515, 3059
 Zweibel E. G., 2017, *Phys. Plasmas*, 24, 55402

This paper has been typeset from a \LaTeX file prepared by the author.